FEDERAL UNIVERSITY OF SÃO CARLOS
CENTER FOR EXACT SCIENCES AND TECHNOLOGY
POSTGRADUATE PROGRAM IN MATERIALS SCIENCE AND ENGINEERING

FRICTION RIVETING OF ALUMINIUM ALLOY 6056-T6 WITH SHORT-GLASS-FIBER-REINFORCED POLYAMIDE 6 COMPOSITE

Bruno Cordeiro de Proença

São Carlos-SP
2017

FEDERAL UNIVERSITY OF SÃO CARLOS
CENTER FOR EXACT SCIENCES AND TECHNOLOGY
POSTGRADUATE PROGRAM IN MATERIALS
SCIENCE AND ENGINEERING

FRICTION RIVETING OF ALUMINIUM ALLOY 6056-T6 WITH SHORT-GLASS-FIBER-REINFORCED POLYAMIDE 6 COMPOSITE

Bruno Cordeiro de Proença

Thesis presented to Postgraduate Program in Materials Science and Engineering to achieve the MASTER DEGREE IN MATERIALS SCIENCE AND ENGINEERING.

Advisor: Dr. Leonardo Bresciani Canto (UFSCar/DEMa)
Co-Advisor: Dr.-Ing. Sergio T. Amancio Filho (HZG/Germany)
Financial Support: CNPq

São Carlos-SP
2017

VITAE OF THE CANDIDATE

Bachelor's in Materials Science and Engineering at the Federal University of São Carlos (UFSCar, 2014) with emphasis on polymeric materials.

UNIVERSIDADE FEDERAL DE SÃO CARLOS

Centro de Ciências Exatas e de Tecnologia
Programa de Pós-Graduação em Ciência e Engenharia de Materiais

Folha de Aprovação

Assinaturas dos membros da comissão examinadora que avaliou e aprovou a Defesa de Dissertação de Mestrado do candidato Bruno Cordeiro de Proença, realizada em 11/08/2017:

Prof. Dr. Leonardo Bresciani Canto
UFSCar

Profa. Dra. Alessandra de Almeida Lucas
UFSCar

Prof. Dr. Arnaldo Ruben Gonzalez
UFRGS

Certifico que a sessão de Defesa realizou-se com a participação à distância do membro Arnaldo Ruben Gonzalez e, depois das arguições e deliberações realizadas, o participante à distância está de acordo com o conteúdo do Parecer da Comissão Julgadora redigido neste Relatório de Defesa.

Prof. Dr. Leonardo Bresciani Canto – Presidente de Comissão Julgadora

ACKNOWLEDGEMENTS

The development of this MSc thesis counted with valuable contributions of many people whom I would like to thank:

- Prof. Dr. Leonardo Bresciani Canto for the opportunities, guidance, critiques and trust by giving me autonomy in my researches since my scientific initiation.
- Prof. Dr. Sergio T. Amancio-Filho for the opportunity, guidance, constructive critiques, friendship and trust by giving me autonomy in my research at HZG.
- Dr. Jorge F. dos Santos for the opportunity to perform my internship at WMP-HZG.
- Dr. Lucian Blaga for the support, encouragement, healthy discussions, friendship and for sharing his expertise in life and FricRiveting with me.
- Employees of the DEMa/UFSCar and PPG-CEM that are dedicating their lives for the intellectual and personal development of the students.
- All people from WMP-HZG. Special thanks to Menno Peters for helping me to perform some of my experiments.
- The Young Investigator Group. Special thanks to my colleagues André, Natalia, Natascha, Eduardo and Seyed for the support and friendship
- My dear friends from São Carlos and life, Carlos, Afonso, Guilherme, Fernando, Gustavos, Rafael, Vinicius, Ligia, Caio, Wesla, Lys, Yumi, Andressa for the personal support and for sharing experiences.
- Movimento Mapa Educação for the opportunity to make Brazil a better place to live.
- My family for the inspiration and unconditional love. Specially my parents and sister for the support, advices, values and opportunities. All my love is yours.
- Janaina, my best friend and love, for her support, love, comprehension and friendship.
- God for everything that happens for me.
- CNPq sponsoring me with MSc scholarship.

ABSTRACT

Friction Riveting (FricRiveting) is a relatively new joining technique for metal-polymer hybrid structures. This master thesis was carried out to investigate the FricRiveting process for polyamide 6 reinforced with 30 wt% short glass fiber (PA6-30GF) and aluminum alloy 6056-T6. These materials were selected because of their current joint use in automotive structures. AA6056-T6/PA6-30GF friction-riveted joints were successfully produced. Peak temperatures monitored for the process achieved between 323 °C and 399 °C leading the plastic deformation and thus anchoring of the rivet. The metallic rivet had its microstructure changed during the process, with dynamic recovery and recrystallization being observed in the anchoring zone. Microhardness in the metallic rivet decreased by 40 % of the base material hardness in the anchoring zone, due to a possible dissolution of the precipitates in the aluminum matrix and dynamic recovery and recrystallization. Polyamide 6 degradation was investigated by viscosity measurements and ATR/FT-IR, the joint with the highest level of degradation showed a reduction of 19 % on viscosity average molecular weight and an increase of 2.4 % of the carbonyl index in relation to the base material. Despite this reduction of properties, the friction-riveted joints had a good mechanical performance under tensile loading. Two joining conditions fractured through the metallic rivet outside the composite plate, achieving 92 % of the ultimate tensile strength of the metallic rivet. The influence of the process parameters on the process temperature, viscosity average molecular weight and ultimate tensile force were studied through Box-Behnken Design of experiment, response surface methodology and analysis of variance. Regression equations for these responses were estimated and validated, and an optimized condition was selected. Post joining heat treatment was performed on the optimized joining condition, resulting in an increase of the joint ultimate tensile force up to 99 % of the metallic rivet ultimate tensile force. The durability of the optimized joint was evaluated through natural weathering. An expected negative effect of weathering on the joint ultimate tensile force was observed, strength decrease of 8.4 % after 6 months and 15.5 % after 12 months of exposure.

Keywords: Hybrid Joints; Friction Riveting; Polyamide 6; AA 6056-T6

REBITAGEM POR FRICÇÃO DE LIGA ALUMÍNIO 6056-T6 EM COMPÓSITO DE POLIAMIDA 6 REFORÇADA COM FIBRA DE VIDRO CURTA

RESUMO

A Rebitagem por Fricção é uma técnica relativamente nova para união de estruturas híbridas metal-polímero. Esta dissertação de mestrado foi desenvolvida para investigar a utilização da técnica com poliamida 6 reforçada com 30% fibra de vidro curta em peso (PA6-30FV) e liga de alumínio 6056-T6, materiais comumente utilizados na indústria automobilística. As juntas rebitadas por fricção foram produzidas com sucesso. As temperaturas processuais variaram entre 323 °C e 399 °C, isso possibilitou a deformação plástica do rebite e consequentemente sua alteração microestrutural. A microdureza na zona de ancoragem do rebite metálico diminuiu 40 % em relação ao material base, devido a uma possível dissolução dos precipitados na matriz de alumínio e também devido à recuperação e recristalização dinâmica. A degradação da PA6 foi investigada por viscosimetria e ATR/FT-IR mostrando uma redução máxima de 19 % no peso molecular viscosimétrico médio e um aumento de 2,4 % do índice de carbonila em relação ao material de base. Mesmo com a redução nas propriedades, as juntas tiveram um bom desempenho mecânico, atingindo 92% da força máxima de ruptura do rebite metálico e tendo a falha no rebite metálico exterior a placa de material compósito. A influência dos parâmetros do processo sobre a temperatura do processo, o peso molecular viscosimétrico e força máxima de tração foram estudadas através do planejamento de experimento Box-Behnken (BBD), superfície de resposta e análise de variância. Equações de regressão para essas respostas foram estimadas e validadas, uma condição otimizada foi selecionada. Com essa junta foi realizado um tratamento térmico após a união, isso aumentou a resistência da união para 99 % da força máxima de ruptura do rebite metálico. A durabilidade das juntas foi avaliada por ensaio de intemperismo natural. Os efeitos sobre a força máxima de tração foram negativos, decréscimos de 8,4 % após 6 meses e 15,5 % após 12 meses.

Palavras-chave: Juntas híbridas, Rebitagem por fricção; Poliamida 6; AA6056-T6

PUBLICATIONS

PROENCA, B.C., BLAGA, L.A., DOS SANTOS, J.F., CANTO, L.B., AMACIO-FILHO, S.T. Influência da Topografia da Superfície de Atrito do Rebite na Formação de Juntas de Alumínio 6056 T6 e Compósito PA6-30FV Rebitadas por Fricção.In: 22º CBECiMat –22° Congresso Brasileiro de Engenharia e Ciência dos Materiais, Natal, Brazil, 06-10 November, 2016.

PROENCA, B.C., BLAGA, L.A., DOS SANTOS, J.F., CANTO, L.B., AMANCIO-FILHO, S.T. Rebitagem por Fricção (“FricRiveting”) de Liga de Alumínio 6056 T6 e Poliamida 6: Influência da Velocidade de Rotação na Formação da Zona de Ancoragem e no Desempenho Mecânico. Soldagem & Inspeção, 2015; 20(4): 489-500.

PROENCA, B.C., BLAGA, L.A., DOS SANTOS, J.F., CANTO, L.B., AMANCIO-FILHO, S.T. Friction Riveting (‘FricRiveting’) of 6056-T6 Aluminum Alloy and Polyamide 6: Influence of Rotational Speed on the Formation of the Anchoring Zone and on Mechanical Performance. Welding International, 2017; 31(7): 509-518.

PROENCA, B.C., BLAGA, L.A., DOS SANTOS, J.F., CANTO, L.B., AMACIO-FILHO, S.T. Rebitagem por Fricção (“FricRiveting”) de Liga de Alumínio 6056 T6 e Poliamida 6: Influência da Velocidade de Rotação na Formação da Zona de Ancoragem e no Desempenho Mecânico. In: XLI CONSOLDA- Congresso Nacional de Soldagem, Salvador, Brazil, 12-15 October, 2015.

PROENCA, B.C., BLAGA, L.A., DOS SANTOS, J.F., CANTO, L.B., AMACIO-FILHO, S.T. Force Controlled Friction Riveting of Glass Fiber Reinforced Polyamide 6 and Aluminum Alloy 6056 Hybrid Joints. In: Society of Plastics Engineers - ANTEC 2015, Orlando, USA: 23-25 Mar, 2015.

x

SUMMARY

LIST OF FIGURES

LIST OF TABLES

LIST OF SYMBOLS AND ABBREVIATIONS

A	Thermo-Mechanically Affected Area
ATR	Attenuated Total Refraction
AZ	Anchoring Zone
B	Height of the Anchoring Zone
BBD	Box-Behnken Design
BM	Base Material
BO	Burn-off
BOR	Burn-off Rate
CDRX	Continuous Dynamic Recrystallization
CF-PEEK	Carbon Fiber Reinforced Poly(ether-ether-ketone)
CHAZ	Composite Heat Affected Zone
CTMAZ	Composite Thermo-Mechanically Affected Zone
D	Rivet Diameter
DaF	Displacement at Friction
DSC	Differential Scanning Calorimetry
EBSD	Electron Backscatter Diffraction
EDS	Energy Dispersive Spectroscopy
FF	Friction Force
FoF	Forging Force
FoP	Forging Pressure
FoT	Forging Time
FP	Friction Pressure
FricRiveting	Friction Riveting
FSW	Friction Stir Welding
FT	Friction Time
FT-IR	Fourier Transformed Infrared Spectroscopy
GF	Glass Fiber
GF-P	Glass Fiber Reinforced Thermoset Polyester
GF-PEI	Glass Fiber Reinforced Poly(ether imide)
H	Rivet Penetration Depth
HT	Heating Time

HV	Vickers Microhardness
HZG	Helmholtz Zentrum Geesthacht
JF	Joining Force
JP	Joining Pressure
JT	Joining Time
LAB	Low Angle Boundary
LOM	Light Optical Microscopy
MHAZ	Metal Heat Affected Zone
MTMAZ	Metal Thermo-Mechanically Affected Zone
PC	Polycarbonate
PEI	Poly(ether imide)
PHAZ	Polymer Heat Affected Zone
PJHT	Post Joining Heat Treatment
PTMAZ	Polymer Thermo-Mechanically Affected Zone
RS	Rotational Speed
RSM	Response Surface Methodology
R●	Free Radical
SEM	Scanning Electron Microscopy
TEM	Transmission Electron Microscopy
Tg	Glass Transition Temperature
Tm	Melting Temperature
UTF	Ultimate Tensile Force
VR	Volumetric Ratio
W	Rivet-Tip Width

1 INTRODUCTION

1.1 General Considerations

The development of engineering polymers and polymer composites for the use in the transportation industry seeks to maximize efficiency in terms of weight and mechanical performance [1]. In recent years, polymers and polymer composites have replaced several automotive metal parts. Nowadays, approximately 16% of the weight in a vehicle is polymer, with a growing trend to reach possibly 25% in the next five years [2]. The use of metal-polymer hybrid structures is essential to the application of polymers and polymer composites in the automotive industry [3, 4].

Currently, the joining processes used in the industry for dissimilar materials, such as metals and polymers, can be divided in two main categories: those in which the joining is achieved by mechanical connection and those relying on a physical-chemical bond between the parts. Mechanical fastened connections involve external fasteners, such as screws, rivets, bolts, among others. The physical-chemical bonding involves an adhesive that connects the joining parts after curing. Mechanical fastened joints are obtained faster and with a lower cost when compared to adhesive bonded ones, for instance, because less surface pre-treatments are required. On the other hand, adhesive bonded joints present less stress concentration (due to absence of through-holes) and weight reduction when compared to traditional mechanical fastening [1,5-7]. Facing these disadvantages, Friction Riveting (FricRiveting) was designed to be an alternative joining technology for metal-polymer hybrid structures.

FricRiveting was developed and patented by Amancio *et al*. [8] at Helmholtz-Zentrum Geesthacht (HZG) in Germany in 2007. As suggested by its name, the technique combines principles from mechanical fastening and friction welding. The feasibility of Friction Riveting has been demonstrated for various combinations of materials, such as polyetherimide (PEI) and AA2024-T3 [9], polycarbonate (PC) and AA2024-T3 [10], laminates of polyetherimide reinforced with glass fiber (GF-PEI) and titanium grade 2 [11], polyether-ether-ketone

reinforced with short carbon (CF-PEEK) fiber and titanium grade 3 [12] and thermoset polyester composite (GF-P) and Ti6Al4V alloy [13, 14].

Preliminary investigations by the author and collaborators carried out at the HZG, from February 2014 to February 2015, showed the technical feasibility of joining AA6056-T6 aluminum alloy with a composite of polyamide 6 reinforced with 30% of short glass fibers (PA6-30GF) [15]. Polyamide 6 is an engineering thermoplastic, well established in the textile, automotive and consumer electronics industry for more than 50 years [16]. In the automotive industry it is mostly used as fiber-reinforced polymer with short glass fiber in air intake manifolds, engine covers, oil tanks and other parts [17]. Aluminum is a lightweight metal with good mechanical and corrosion resistance. 6056 aluminum alloy fits in the needs of weight reduction for the automotive industry being suitable for aluminum fastener applications [18]. Figure 1.1 shows examples where the combination of AA6056-T6 and PA6-GF could be used vehicles; 1- Under the hood: air coolers, turbo air ducts, air intake manifolds, oil pans, transmission parts and others; 2- Front End/Structural: fender stiffener; 3- Rear: fuel tank and 4 - Trunk: spare wheel recess. In these examples, FricRiveting has good potential applications for automotive components [19].

Figure 1.1 Examples of applications of AA6056-T6 and PA6-GF in the automotive [19].

This master thesis aims to investigate a new process variant of the FricRiveting technique for polyamide 6 reinforced with short glass fiber and aluminum alloy 6056-T6. The new process-variant was divided into two phases controlled by force, with the frictional phase limited by the displacement of the spindle, and the forging phase limited by time. For this purpose, Box-Behnken design of experiment was used to study the correlations between the FricRiveting process parameters, process temperature, process-related changes in the joined materials and quasi-static mechanical behavior of the joints. The techniques used to determine the correlation between process, microstructure and mechanical properties of the joints were: optical microscopy and Scanning Electron Microscopy - Electron Backscatter Diffraction (SEM-EBSD) for the microstructure; microhardness for the local mechanical properties; Differential Scanning Calorimetry (DSC), dilute solution viscometry and Attenuated Total Refraction – Fourier Transformed Infrared Spectroscopy (ATR-FTIR) for the physical-chemical characterization; and T-pull tensile testing for the global mechanical performance; and T-pull tensile testing for the global mechanical performance. Finally, the influence of post-weld heat treatment and natural weathering on the ultimate tensile force was analyzed for an optimized joint.

1.2 Motivation and Objectives

The use of polymer composites in the automotive industry leads to the challenge of developing techniques to join lightweight dissimilar structures. The main motivation for this thesis is to investigate and optimize a new process variant of Friction Riveting to join materials commonly used in the automotive sector.

Recently, Proenca *et al.* [15] have demonstrated the technical feasibility of joining aluminum alloy 6056-T6 rivets with short glass fiber reinforced polyamide 6 (PA6-30GF) by FricRiveting. However, the microstructural changes in the joined materials were not deeply investigated. The author did not focus in the correlation of these changes with the joining parameters and how it affects the global properties of the joint. The joints were not optimized in terms of quasi-static mechanical performance as well.

Considering these knowledge gaps, this work has the following objectives:

Scientific:

- Understand the relationships between process parameters, microstructure and mechanical properties of AA6056-T6/PA6-30GF friction-riveted metallic-insert joints.

Engineering:

- Evaluate the use of a new Friction Riveting process variant (process controlled by force and limited by spindle displacement) and, through determining the influence of parameters, optimize AA6056-T6/PA6-30GF joints in terms of the ultimate tensile force.

2 LITERATURE REVIEW

2.1 Materials

2.1.1 Aluminum Alloy 6056-T6 (AA 6056-T6)

Aluminium alloy 6056 is part of the Al-Si-Mg alloys (AA6XXX) family. The main elements combine to form the stoichiometric compound magnesium silicide (Mg_2Si), where the Mg/Si ratio is 1.73 [20]. The use of magnesium and silicon makes the AA6XXX alloys heat treatable and increases their strength. AA6XXX alloys have also good formability, weldability, machinability and corrosion resistance [21,22]. The nominal chemical composition of aluminum alloy 6056 is shown in Table 2.1.

Table 2.1 Chemical composition of aluminum alloy 6056 [23].

Elements [% weight]								Impurities		
Si	**Fe**	**Cu**	**Mn**	**Mg**	**Cr**	**Zn**	**Zr+Ti**	**Each**	**Total**	**Al**
0.7-1.3	**0.5**	**0.5-1.1**	**0.4-1.0**	**0.6-1.2**	**0.25**	**0.1-0.7**	**0.20**	**0.05**	**0.15**	**Bal**

The strength of this alloy is related to the precipitation hardening mechanisms that occurs during the aging treatment [24,25]. Starting from a solid solution, the sequence of precipitation in the cooling phase of the AA6XXX follows the steps described below [26]:

$$SSS \rightarrow \text{atomic clusters} \rightarrow GP \rightarrow \beta'' \left(Mg_5Si_6 \right) \rightarrow \beta' \left(Mg_{1.7}Si \right) \rightarrow \beta \left(Mg_2Si \right)$$

SSS denotes supersaturated solid solution. Atomic level clusters of Mg and Si and some small particles as Guinier-Preston (GP) zones are formed. This zones are precursors to the formation of coherent β'' and β' metastable precipitates. β stable precipitate is formed from β'' and β'. The presence of different types of precipitates is related to the composition, heat treatment and aging conditions. The use of heat treatments is a common practice for AA6XXX alloys. Examples are the T4 (solution heat treated and naturally aged to a

substantially stable condition), T5 (cooled from an elevated-temperature shaping process and artificially aged) and T6 (solution heat treated and artificially aged) conditions [25]. The hardness in some AA6XXX alloys is related mainly to the formation of β'' [24]. The formation of β'', β' and β phases are the main strengthening mechanisms of AA6XXX alloys [20,22,24,25] due the creation of distortions in the crystal lattice and the presence of coherent internal stresses, whose factors hinder the movement of the dislocations.Table 2.2 shows examples of relevant properties of AA6056 alloy for this study.

Table 2.2 Relevant properties of AA6056-T6 [18,22,27].

Properties	AA6056-T6
Density [g/cm^3]	2.70
Tensile strength at 23 °C [MPa]	380-420
0.2% yield strength [MPa]	350-375
Elongation [%]	6-12
Inferior Melting point [°C]	610*
Coef. of Linear Thermal Expansion, [µm/mm°C]	23.4

* General property for AA6XXX

2.1.2 Polyamide 6 Reinforced with 30 % of Short Glass Fiber (PA6-30GF)

Polyamide 6 is synthesized by ring opening polymerization of ε-caprolactam initiated by water [28,29]. The polyamide 6 repeating unit is illustrated in Figure 2.1.

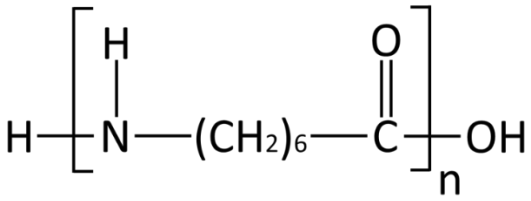

Figure 2.1 Repeating unit of polyamide 6.

PA6 is a semi-crystalline polymer with melting point of 220 ºC. The crystallinity is a result mainly of the amide groups (Figure 2.1) that allow hydrogen bonds between chains. This structure gives good balance of material properties such as stiffness, hardness, strength, toughness, chemical resistance, wear resistance and thermal stability [28].

PA6 is hygroscopic owing to hydrogen bonds between water and polyamide amide groups; it can absorb up to 9.5 % of its weight in moisture. Water absorption is higher in the amorphous region due the larger free volume and thus chain mobility. Moisture affects strongly polyamides properties. For instance, absorbed water acts as a plasticizer, which reduces the glass transition temperature (T_g) and, hence, decreases the modulus and strength, and increases the elongation at break and impact strength at room temperature [28,30,31].

The rheological properties of polyamides are sensitive to factors such as moisture, molecular weight, shear rate, temperature and addition of fillers [28, 30-32]. The moisture in the molten polyamide decreases the melt viscosity due the depolymerisation by hydrolysis, which decreases the molecular weight [30, 32]. The dependence of melt viscosity on molecular weight of polyamide 6 is similar to other thermoplastics. The viscosity increases linearly with the molecular weight to the power 1, until the critical molecular weight for entanglements. After this point, the viscosity is proportional to the molecular weight to the power 3.4 [32]. The viscosity of the molten polyamides is very sensitive to changes in temperature; an increase in 20 °C could decrease the melt viscosity from 10000 Pa.s in 230 °C to approximately 6000 Pa.s in 250 °C and to 2000 Pa.s in 270 °C [28,32]. Mainly the melt viscosity of polyamide increases significantly by glass fiber addition at low shear rates; however in high shear rates this effect is not evident [28]. Polyamide 6 is an engineering thermoplastic established in the textile, automotive and consumer electronics industry for more than 50 years [16]. In applications where high stability at high temperatures is required, the polyamides are used filled with fibers. Polyamides are usually filled with short glass fibers to improve the mechanical performance of the components in automotive industry; one good example of this is the air intake manifold. The use of glass fibers as reinforcement in polyamides improve some properties such as

hardness, resistance to creep and fatigue, and reduces the coefficient of thermal expansion [30,33].

Table 2.3 compares some relevant properties of polyamide 6 and the corresponding composite filled with 33 wt% of short glass fiber (SGF).

Table 2.3 Properties of polyamide 6 and polyamide 6 based composite filled with 33 wt% of short glass fiber [34,35].

	Polyamide 6	Polyamide 6 + 33 wt% SGF
Density [g/cm^3]	1.13	1.39
Moisture [%]		
24 hour*	1.6	1.1
50% RH**	2.7	1.8
Saturation***	9.5	6.4
Tensile strength at 23 °C [MPa]	85	230
Notched izod impact strength, 23 °C [J/m]	65	110
T_g; T_c; T_m [°C]	~40; 185; 220	~40; 185; 220
Heat deflection, 1.8 MPa [°C]	65	208
Coef. of Linear Thermal Expansion, [µm m/mm°C]	83	38

* Specimens are immersed in distilled water at 23°C for 24 hours

** Specimens are exposed to a 50% relative humidity environment at 23°C for 24 hours.

*** Specimens are immersed in distilled water at 23°C until the water absorption ceases

Polyamides undergo several kinds of chain degradations at different conditions [28,30,36-43]. For the purpose of the work, thermal degradation [36-39] and thermo-oxidative degradation [40-43] were considered. In the case of polyamide 6, the main products of the thermal degradation are amine and carboxyl end-functionalized scission chains, oligomers and monomer. Thermal decomposition of PA6 can be divided into three categories: (1) those that occurs

at temperatures below 300 °C in the absence of a nucleophile (Lewis base); (2) those that occurs at temperatures much greater than 300 °C in the absence of a nucleophile, and (3) those that occurs in the presence of a nucleophile at temperatures below 300 °C [36]. These categories were proposed by Davis *et al*. [36], based on a review by Levchik [38] on thermal decomposition of aliphatic polyamides.

In the first category (below 300 ºC) and in the absence of a nucleophile the main product of PA6 thermal degradation is ε-caprolactam (monomer). In the second category of PA6 thermal degradation - which takes place at temperatures between 300 and 800 ºC in the absence of a nucleophile - the products are monomers, cyclic oligomers, various small gaseous molecules and amine end-functionalised small chains. In the third category (thermal degradation in the presence of a nucleophile such as hydroxide ions (OH^-) from adsorbed moisture) the major products are amine and carboxyl end-functionalized small chains through hydrolysis of amide linkages, as shown in Figure 2.2. This thermal degradation results in a drastic decrease in the molecular weight [36,38].

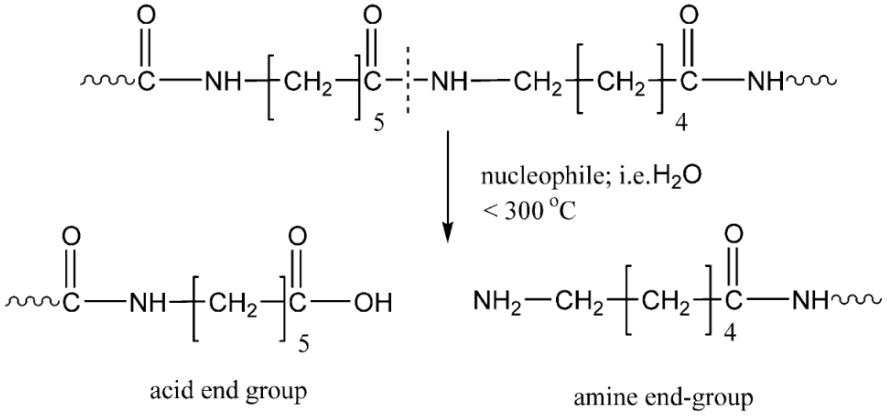

Figure 2.2 PA6 thermal degradation reaction initiated by the presence of a nucleophile, such as water. Adapted from [36].

The thermal degradation of polyamides is very different in the presence of oxygen. The thermo-oxidative degradation of polyamide initiates when labile hydrogen is extracted from the main chain. In polyamides, the methylene group adjacent to the nitrogen atom is attacked because it is the weakest bond. This

reaction occurs due to certain free energy in the system, like heat or light, and generates a reactive and unstable polymer 'free radical' (R●) as illustrated in Figure 2.3-a. The propagation occurs when the free radical (R●) reacts with an oxygen (O_2) molecule to form a peroxy radical (ROO●), Figure 2.3-b. This radical can be recombined generating carbonyl and hydroxyl groups. The peroxy radical is also able to extract a hydrogen atom from another polymer chain; this reaction leads to the formation of a hydroperoxide (ROOH), Figure 2.3-c. Then, the hydroperoxide is divided in two new free radicals, alkoxyl (RO●) and hydroxyl (●OH), Figure 2.3-d. The propagation will continue and other polymeric molecules will be attacked. Degradation is finished when free radicals are stabilized. For engineering purposes, stabilizers are added to scavenge free radicals [40,42,43].

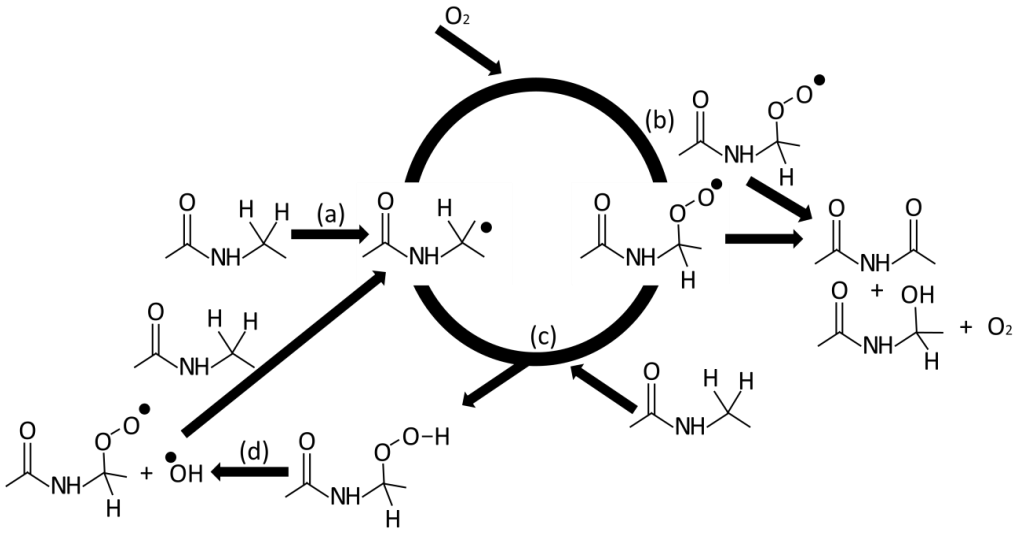

Figure 2.3 General oxidative mechanism for aliphatic polyamide. Adapted from [42].

The general oxidation mechanism, as shown in Figure 2.3, is considered satisfactory to describe the thermo-oxidative degradation mechanism of polyamides. Nevertheless, Lánská *et al*. [44,45] proposed some deviations, during the oxidation, hydroperoxides are formed and its decomposition can lead to alkoxy radicals (Figure 2.3). Primary amides and aldehydes can be formed by the decomposition of alcohols. The alcohols are formed by the reaction between alkoxy radicals and another polymer chain, as shown in Figure 2.4-a. The alkoxy radicals can also suffer β-scission, as shown in Figure 2.4-b. These thermo-

oxidative reactions decrease the polyamide mechanical properties due to the loss in molecular weight [42].

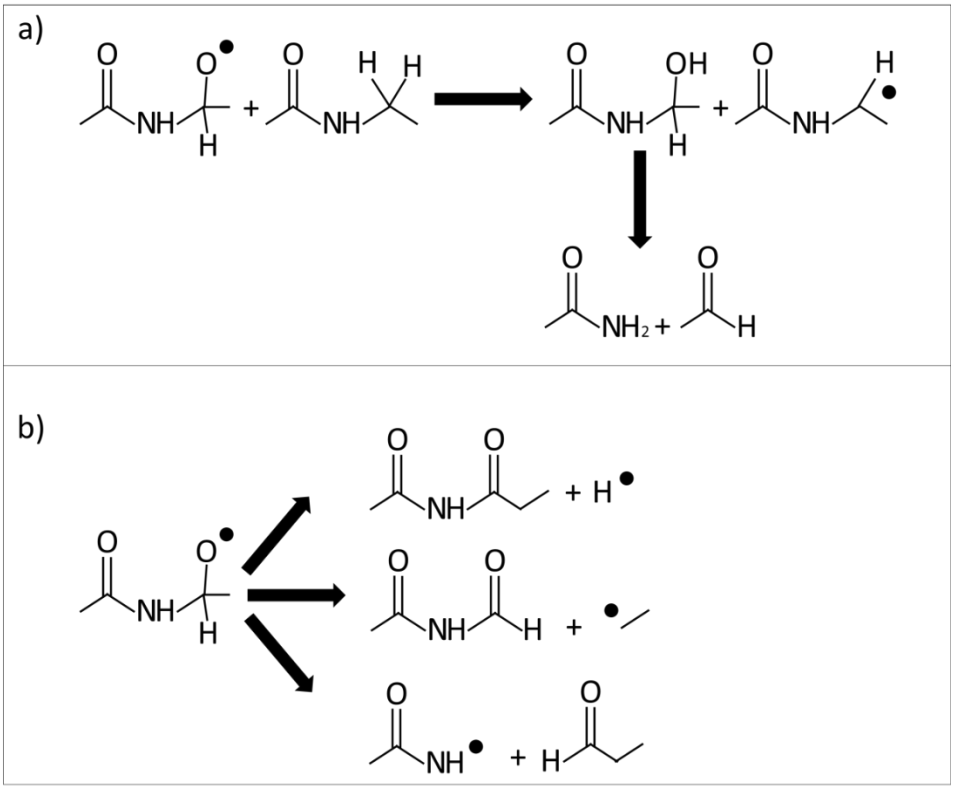

Figure 2.4 Alkoxy radicals possible reactions: Alcohols formed by the reaction between alkoxy radicals and polymer chain (a) and alkoxy radicals suffers β-scission (b). Adapted from [42].

The thermo-oxidative degradation of polyamide 6 has been studied and the correlation between temperature, molecular mass and mechanical properties evaluated [42,46]. Dong e Gijsman [42] investigated the influence of temperature on the thermo-oxidative degradation of polyamide 6 films. Non-stabilized 50 μm-thick polyamide 6 films were thermo-oxidative aged in a forced air venting oven at temperatures between 120 and 170 °C under atmospheric conditions and different times. The molecular weight of the films was estimated by relative viscosity measurements through dilute solution viscometry. The relative viscosity had a great decrease at temperatures above 140 °C in short times (50 h). It was found that the polymeric degradation decreased the elongation at break of aged specimens. In the same study a new peak in PA6 IR spectrum was observed

after the oxidation procedure. The new peak was associated to products of polyamide oxidation such as carbonyl compounds as ketones and aldehydes. The carbonyl index increases at high temperatures of the oven and in a fast rate also. Gonçalves [46] analyzed changes in the molecular weight of PA6 samples extracted from joints produced by Friction Spot Welding (FSpW) with different heat inputs, in order to estimate the level of degradation caused by this process. The molecular weight was determined from dilute solution viscometry analysis. The viscosity average molecular weight decreased almost linearly with the maximum temperature achieved during the process. The maximum decrease in the molecular weight (7% in comparison with the base material) did not compromise the quasi-static mechanical strength of the PA6 spot welds.

2.2 Joining Techniques for Polymer-Metal Structures

Currently, the joining of polymer-metal structures is achieved mostly by mechanical fastening, adhesive bonding, hybrid techniques derived from these two and injection over molding [1,5]. The limitations of the currently used joining techniques are the long joining cycles, the need for surface preparations and uncertainty in predicting the long-term durability for the adhesive joints [6]. Moreover, higher number of process steps, higher stress concentration (related to the through-hole in the joining partners) and an increase in the weight are also issues in the state-of-the-art mechanical fastened joints [47]. Finally , single-part structures are usually impractical or very expensive, due to the restrictive features such as complex mold design and large size, as it is the case for injection over molding [48].

New techniques for thermoplastic-metal hybrid joints have been developed during the last decades. Ultrasonic welding [49], induction welding [50], resistance welding [51], friction riveting [8], friction-based injection clinching joining [51,52] and friction spot joining [53,54] are examples of innovative techniques that have been tested and already shown good results.

The following sections are dedicated to present the fundamentals of adhesive bonding, mechanical fastening, injection over molding and Friction Riveting.

2.2.1 Adhesive Bonding

Adhesive bonding is used to join similar and dissimilar materials. It is based on chemical bonding, where the formation of intermolecular forces between adherent and adhesive occurs. The adhesive can be a thermoplastic, thermoset or even ceramic; this material suffers a chemical (curing) or physical reaction enabling the formation of the joint [6]. In the last decades, the use of adhesive bonding increased substantially due to the development of adhesives with high strength and the need to reduce weight in the transportation sector.

The strength of bonded joints is determined by the adhesion - intimate contact force between surfaces - and cohesion - the internal force that keeps the joint together [6]. The adhesion is therefore essentially an interfacial phenomenon in which chemical and physical forces are involved. Several theories to explain the phenomena of adhesion have been established, such as adsorption (gas or liquid particles physically bound to the solid or liquid surface), diffusion, mechanical anchoring and electrostatic adhesion, among others. Figure 2.5 schematically illustrates the adhesion theories. The increasing in the roughness and wettability of the adherent parts are related to the mechanical anchoring and adsorption theories, respectively [56].

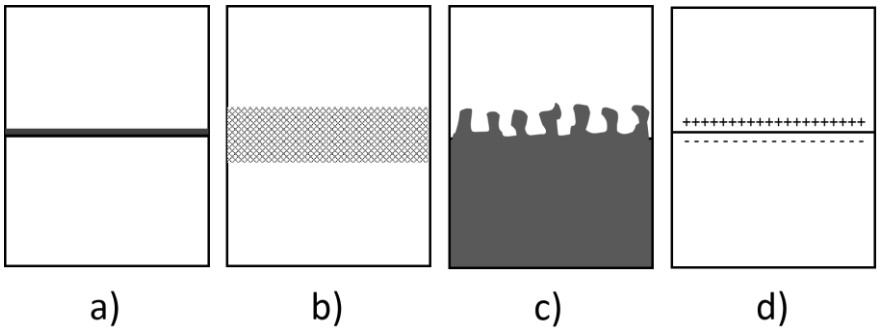

Figure 2.5 Illustration of the adhesion theories: adsorption (a), diffusion (b), mechanical anchoring (c) and electrostatic (d). Adapted from [56].

The main advantages of joints produced by adhesive bonding are the low stress concentration, good surface finishing, hermetic sealing and weight reduction. However, the adhesive bonding technique has disadvantages such as the long curing time for the adhesive, the difficulty of disassembly, and

susceptibility to damages in the joint components. Additionally, the parts need an extensive surface preparation -e.g. sand blasting or acid pickling - to improve the surface roughness or activate the surface (i.e. increase surface energy), which add costs to the process [57]. Environmental factors, such as temperature and humidity, have a negative influence on the final mechanical performance and durability of an adhesively bonded joint. One of the major factors limiting the use of adhesives is the uncertainty in predicting the long-term durability of this type of joint [5,6].

2.2.2 Mechanical Fastening

Mechanical fastening is one of the oldest methods used to join materials. The mechanical fastening is based on interactions and mechanical forces between components. There are several mechanical fastening techniques, but generally it relies on an additional part – a mechanical fastener – which is used to join the components. These fasteners can be, for instance: bolts, rivets, screws, nails and other devices. Originally, this technique was used to join metallic parts, but latter the application was performed to join polymeric parts, polymer composite parts and also hybrid polymer/composite and metal parts as well [47]. Mechanical fastening methods are widely used to obtain hybrid polymer-metal joints because the assembly does not depend directly on the joining parts' properties.

Mechanical fastening is widely used in automotive [3], aircraft [7] and civil engineering [58] applications, especially due to their cost efficiency and shorter joining cycles in comparison to adhesive bonding. Also, no extensive surface preparation is needed to achieve good mechanical performances. Nevertheless, the technique presents concerns due to problems such as the fastener-related increase in the weight of the structure, the need for multiple steps in the process, and stress concentration generated by the presence of through-holes [7,47], which may cause premature failure of the joints. Another important issue is the galvanic corrosion of the metallic joining parts in metal-CFRP hybrid structures [59].

2.2.3 Injection Over Molding

Injection over molding is a technology to join metal parts with polymers by polymer injection molding, several variants of this process exist. One of these variants is the metallic insert molding illustrated in Figure 2.6. Firstly, the metallic part (Figure 2.6-a) is placed into the injection mold cavity (Figure 2.6-b). Then molten polymer is injected over/around it (Figure 2.6-c). After cooling, the joining is achieved (Figure 2.6-d). The main joining mechanism is mechanical anchoring. Nevertheless, a possible adhesion between the parts is not discarded. Knifes and screwdrivers are examples of products manufactured by metallic insert molding process [60,61].

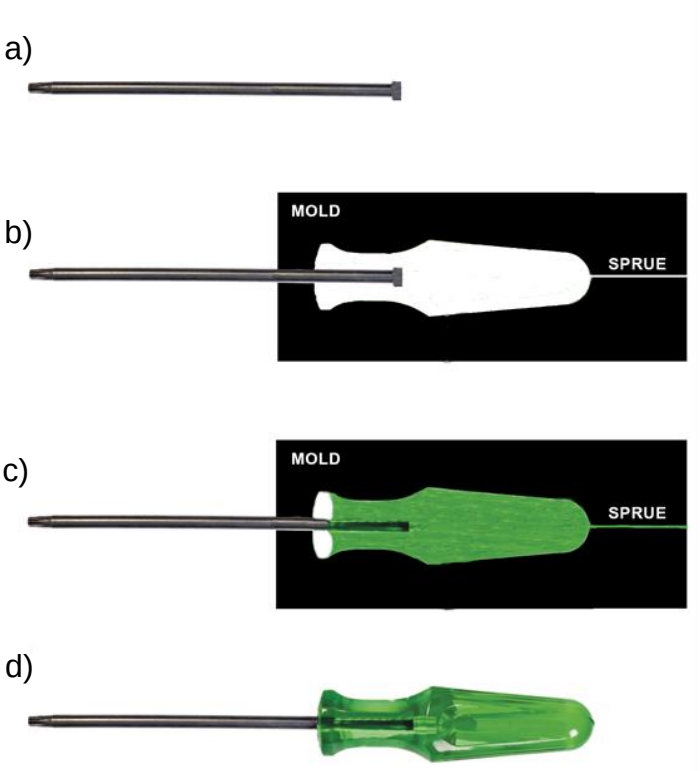

Figure 2.6 Illustration of the metallic insert molding process: metallic part (a), metallic part placed into injection mold (b), the mold is filled with molten polymer (c) and after the cooling the product is obtained (d). [Personal archive]

Injection over molding has been used in some industrial areas, such as in automotive [48]. Currently, this technique has been used in automotive front-end modules [62], instrument-panels and bumper cross-beams, door modules, and tailgates [48,63]. The main advantages are the sealing, reduction of the number

of components, high degree of automation and no further finish operations. However, restrictive features like complex design and large size reduce the application of the technique and it cannot be used for all thermoplastics due to the shrinkage behavior of the polymer materials in comparison with the metals [48,60,64].

2.2.4 Friction Riveting

Friction Riveting is a joining technique for polymer-metal hybrid joints developed and patented in Germany by Amancio *et al.* from the Helmholtz-Zentrum Geesthacht [8,65]. The development of the technique started with unreinforced thermoplastics joined with aluminium alloys in the mid 2000's. Following that, the feasibility of new combinations of materials, such as fiber reinforced thermoplastics and thermosets joined with different metallic bolts [10-13,15] were addressed. It is assumed that friction-riveted joints have less stress concentration when compared to classical bolted connections due to the absence of a through-hole. Additionally, it does not need extensive surface preparation as adhesive bonding and the process time is fast in comparison with the two traditional techniques.

Friction Riveting is based on mechanical fastening and friction welding. During the process, a rotating cylindrical metallic rivet is pressed into a polymeric base plate producing frictional heat that allows the rivet to be deformed and anchored inside the plate. Example of possible configurations of friction-riveted joints are "metallic insert joint", "overlap joint"(metal-polymer and polymer-polymer) and "sandwich joint", as schematically shown in Figure 2.7 [65].

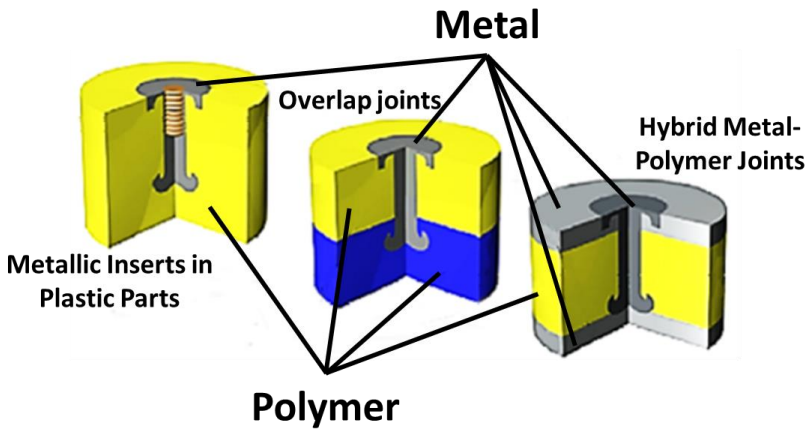

Figure 2.7 Possible Configurations of friction riveted joints. From the left to the right: metallic insert joint; overlap joint; sandwich type joint [9].

The Friction Riveting process is schematically shown in Figure 2.8 for its basic joint configuration (“metallic insert joint”).

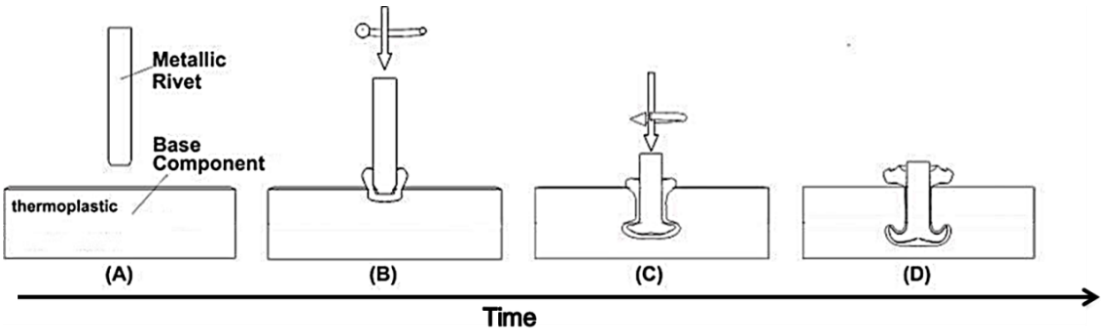

Figure 2.8 Simplified scheme of the Friction Riveting process for the “metallic-insert joint” configuration: start position of the joining parts (a); rotating rivet is insert in the polymeric plate (b); deceleration and rivet forging (c) consolidation of the joint (d) [11].

Prior to the process, the parts are positioned and clamped: the metallic bolt in the magazine and the polymer plate in the specimen holder (with backing support) (Figure 2.8-a). The spindle takes the metallic rivet from the magazine. After, the spindle moves towards the polymer plate. When the spindle is in the pre-set position, the process begins. The rivet starts to rotate until a pre-set rotational speed is achieved. Afterwards, the joining head begins the axial movement inserting the rotating metallic rivet into the polymeric plate. Herewith frictional heat is generated, causing the melting (in the case of semi-crystalline

polymers) or softening (in the case of amorphous polymers) of the polymer around and underneath the tip of the rivet due the local increase in temperature. The continuous force and rotational speed make the rivet penetrate deeper into the polymeric plate, expelling the molten/softened polymer as a flash (Figure 2.8-b). The temperature at the tip of the rivet continues to increase. This occurs because the heat input becomes larger than the heat outflow due the low thermal conductivity of the polymer, thus generating a concentration of heat. At the end of the friction phase, the temperature at the tip of the rivet is high enough to plasticize it (the plasticized/softened state of the rivet is achieved in temperatures above 50% of the alloy melting point [22]) (Figure 2.8-c). At this point, the rotational speed is decreased to zero and the axial force is increased up to a pre-set value (the so called forging force is applied) or kept constant (forging force is absent). The plasticized tip of the rivet is deformed due to the opposite forces related to the colder polymeric volume, assuming a paraboloidal geometry with larger diameter and forming the anchoring zone. Then, the joint consolidates under pressure, since no forced cooling is applied (Figure 2.8-d) [8, 9,15].

In the past studies, Friction Riveting was carried out in a RSM 400 high-speed friction welding machine, manufactured by Harms & Wende GmbH [10,11]. In this study, a new machine that consists in a commercially available high-speed friction-welding spindle (RSM 410, Harms & Wende GmbH, Germany) mounted on an automated structure (HZG, Henry Loitz Robotik, Germany) with tri-axial force sensors and an integrated position sensor was used (Figure 2.9) [12,15]. The new Friction Riveting joining equipment has additional features and provides thus further development opportunities for the technique, as it will be described in the following paragraphs.

Figure 2.9 Friction Riveting equipment (commercially available high-speed friction- welding spindle on automated structure with tri-axial force sensors and an integrated position sensor) available at Helmholtz Centre Geesthacht, Germany.

When FricRiveting was performed via the RSM 400 high-speed friction welding machine, the process can be only controlled by time and the process had three key joining parameters: Rotational Speed (RS), Joining Time (JT) and Joining Pressure (JP) [9-12]. The Rotational Speed is the angular velocity of the rotating rivet and influences directly the heat generation. Indirectly, this parameter influences the viscosity of the molten/softened polymer and the deformation of the tip of the metallic rivet. The Joining Time (JT) consists in sum of the Friction Time (FT) and Forging Time (FoT). The Friction Time (FT) is the time in which the bolt rotates inside the polymeric plate and the Forging Time (FoT) is the duration in which an higher axial load is applied to the rivet after during (e.g. at 30% decrease of set up rotational speed [9-11]) or after the deceleration. The Joining Time (JT) influences on the generation of voids because of the polymer degradation during friction and/or because of the polymer shrinkage in the consolidation during the forging phase. The Joining Pressure (JP) is separated in Friction Pressure (FP) and Forging Pressure (FoP). The Friction Pressure (FP) is the pressure applied during the Friction Time. When used, the Forging Pressure (FoP) is the pressure applied during the Forging Time in order to deform

the tip of the metallic bolt. This parameter is related to the normal pressure distribution, rivet deformation and consolidation of the joint [9-12].

With the new available joining equipment (Figure 2.9), the process can be controlled either by or as a combination of time, force or spindle displacement; additional set-up parameters may be used to support process control, such as rotational speed and spindle-rotation angle. Taking into account the hardware improvements, a new variant of the process was introduced [15]. The new joining procedure was divided into two controlled steps. The first step is the friction phase. In this step the process was controlled by force and limited by displacement (position control) to avoid the complete perforation of the polymer composite plate and control indirectly the heat input. This means that the friction phase will finish when the spindle reaches the set displacement and rotation speed decreases to zero; at this point the second process step initiates. This step is represented by the final rivet forging and joint consolidation, whereas the axial force can be kept constant or increased (application of forging force); in this last step, the process is controlled by force and limited by time. This step is more adequate to be limited by time since the consolidation of the joint is dependent on the resulting cooling rate of the components, while the rotation has come to an end, thus reducing the risk of full penetration.

The new process parameter introduced in this process variant is Displacement at Friction (DaF). Axial force in the friction (Frictional Force, FF) and forging phases (Forging Force, FoF) is set in Newton instead of MPa (pressure unit) as force sensors allow for a more precise setup. The Displacement at Friction (DaF) is the spindle displacement during the friction phase. In the time-controlled process variant, Friction Time is responsible for controlling heat development and spindle displacement. Rivet penetration is variable and a more complex control of heat input is required to avoid base plate perforation. Therefore the new process parameter DaF provides a better control of rivet penetration.

A typical FricRiveting monitoring curve for time-control (the description of the monitoring curve for the new process variant is presented in Section 4) with major controlled joining parameters and variables is presented in Figure 2.10.

The process starts in t_0 when the rivet touches the polymer plate with a certain rotational speed and pressure (Friction Pressure). The course (straight line) indicates the spindle displacement. The frictional phase ends when the Friction Time (FT) is achieved. Then, the rotational speed is decreased to zero and, in this case, the pressure is increased (Forging Pressure). This pressure is relieved when the Forging Time (FoT) is achieved and the process is ended.

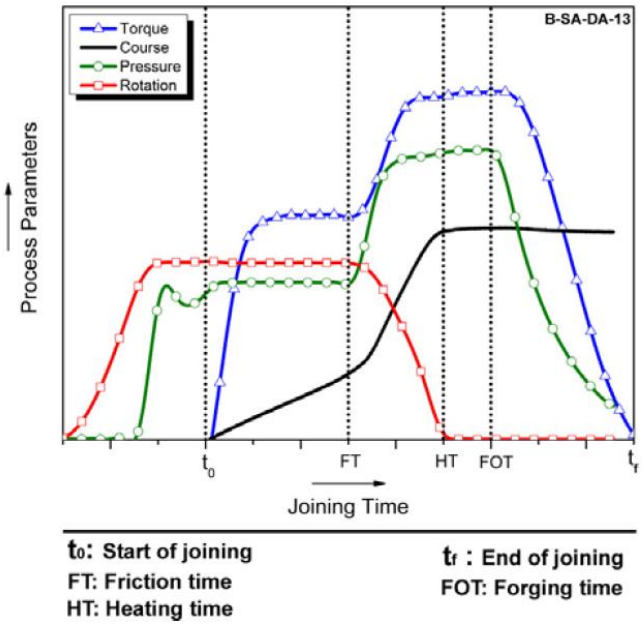

Figure 2.10 Typical FricRiveting monitoring curve [9] with process parameters and variables.

The process variables of FricRiveting are Heating Time (HT), Burn-Off (BO), Burn-Off Rate (BOR), Temperature (T) and Frictional Torque (Mz). The Heating Time (HT) is the time between the touch-up of the rotating rivet on the polymer plate surface and the moment in which the rotational speed is stopped. It provides good estimates of the thermal cycle in the process. The Burn-Off (BO) is the axial displacement (course) shown in the monitoring curve and is associated with the penetration depth and deformation of the rivet into the polymer plate. The Burn-Off Rate (BOR) is a ratio between the burn-off and the heating time and provides an approximation of the real joining speed. The Temperature (T) achieved, usually measured on the expelled flash material with an infrared camera; it is a variable used to explain the physicochemical changes

in the polymer and in the metal. The Frictional Torque (Mz) torque helps to estimate the energy input of the joints and can be correlated with the behaviour of the molten polymer and the plasticized metallic rivet [9,11,12].

The microstructural zones of friction-riveted joints were described for the first time by Amancio-Filho [66] using polyetherimide and AA2024-T351. Four microstructural zones were identified and described (Figure 2.11). Two affected zones were identified in the polymer: the polymer heat affected zone (PHAZ) and the polymer thermo-mechanically affected zone (PTMAZ). The other two zones were identified in the metallic joining part: the metal heat affected zone (MHAZ) and the metal thermo-mechanically affected zone (MTMAZ). The PHAZ and MHAZ are only affected by the heat generated. The PTMAZ and MTMAZ are affected by the heat as well as by the high plastic deformation imposed by the rivet movement along the process. Because of that, these zones are susceptible to metallurgical (in the rivet) and physicochemical (in the polymer) phenomena.

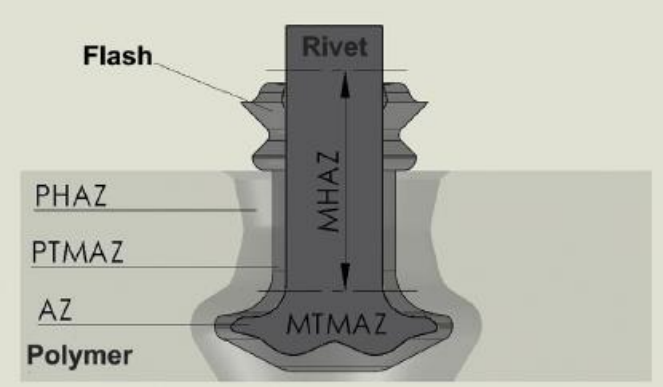

Figure 2.11 Representation of the four microstructural zones described in friction-riveted joints. Polymer heat-affected zone (PHAZ), polymer thermo-mechanically affected zone (PTMAZ), Metal heat-affected zone (MHAZ) and metal thermo-mechanically affected zone (MTMAZ). The Anchoring Zone (AZ) is also shown [66].

The anchoring zone (AZ) of the deformed rivet tip is also shown in Figure 2.11. The geometry of the anchoring zone dictates the joint strength. Three geometrical models for the anchoring efficiency were proposed trying to predict the mechanical strength of insert type friction-riveted joints under static load (T-pull tensile testing). For all these models the anchoring efficiency is calculated using the dimensions of the deformed rivet within the polymeric plate. The first method developed was the aspect ratio (AR) [65], where the efficiency is obtained

by the ratio between the width of the deformed rivet (W) and the penetration depth of the rivet (H); when W is greater than H is the reversal of the ratio. Friction riveted joints of polyetherimide (PEI) with aluminum alloy AA2024-T351 [65] and polycarbonate (PC) with aluminum alloy AA2024-T351 [10] showed an increasing trend on the ultimate tensile force when AR increases. However, with other combinations of materials the same behavior was not observed [11]. It seems that the simplified two-dimensional approach to calculate the efficiency is not applicable to all deformed rivet geometries. Thus, Blaga *et al.* [67] devised the volumetric ratio (VR) concept (Figure 2.12), which considers the interaction volume of the polymer that is above the deformed area of the tip of the rivet. VR is calculated using Equation 1, where H is the penetration of the metallic rivet, B is the height of the deformed tip of the rivet, W is the deformation of the metallic rivet and D is the original diameter of the metallic rivet. Recently, Altmeyer *et al.* [12] proposed a third model named Mushrooming Efficiency. From ballistics, this two-dimensional method takes into consideration only the deformation of the tip of the metallic rivet. Besides being two-dimensional, the Mushrooming Efficiency is applied only to cases where the depth of penetration has no significant changes between the conditions examined [68]. This limits the use of this method and becomes invalid under conditions with high variations in the depth of penetration.

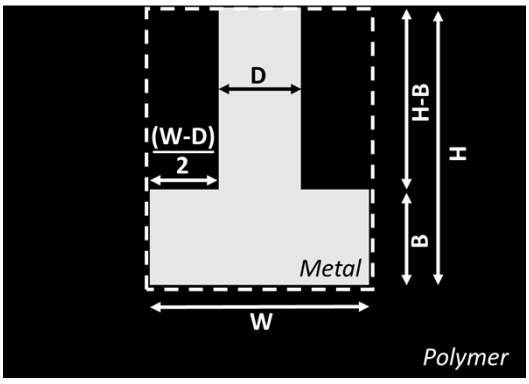

Figure 2.12 Simplified geometry of an insert type of friction-riveted joint used to calculate the Volumetric Ratio [67].

$$VR = \frac{(H - B) \cdot (W^2 - D^2)}{W^2 \cdot H} \quad (1)$$

The types of failure of metallic insert type friction-riveted joints under tensile loading (T-pull testing) were described by Amancio-Filho *et al.* [69], as shown in Figure 2.13.

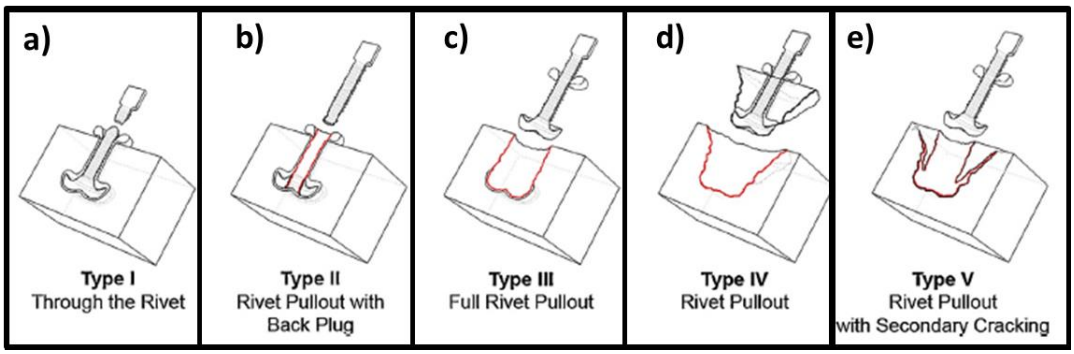

Figure 2.13 Friction-riveted joints failures under T-pull testing. The thicker red lines indicate the path of crack propagation upon final failure [69].

Figure 2.13-a shows a ductile fracture that occurred in the metallic rivet outside of the polymer plate (“through the rivet”). This failure is the best in terms of joint strength since the maximum tensile strength of the joint is comparable to the maximum strength of the metallic rivet. Figure 2.13-b shows a fracture that occurred within the deformed tip of the rivet (“rivet pullout with back plug”). The rivet is pulled out from the polymer, leaving a part of the anchoring zone inside of the polymer plate. Figure 2.13-c shows a fracture that occurred around the anchoring zone of the polymer (“full rivet pullout”). The rivet is completely removed leaving a cylindrical cavity in the polymer plate. Figure 2.13-d shows a fracture that also occurred around the anchoring zone of the polymer but the crack propagates toward the upper surface of the polymer (“rivet pullout”). The rivet is pulled out together with an amount of polymeric material. Figure 2.13-e shows the rivet pullout with secondary cracking fracture. In this failure, the nucleation starts at multiple sites in the polymer around the anchoring zone but the rivet is eventually pulled out. The influence of the anchoring zone on the failure type have been shown for several combinations of materials [10,11,15]. Joints with great values of volumetric ratio might fail through the rivet (Type I) and joints with small values of volumetric ratio might suffer the failure type three (“full rivet pullout”).

3 MATERIALS AND METHODS

3.1 Experimental Approach

This dissertation focused on the optimization of the FricRiveting process for aluminum alloy 6056-T6 and glass fiber reinforced polyamide 6 composite. For this purpose, the experimental approach of this research work was divided into four main phases, which are shown in Figure 3.1

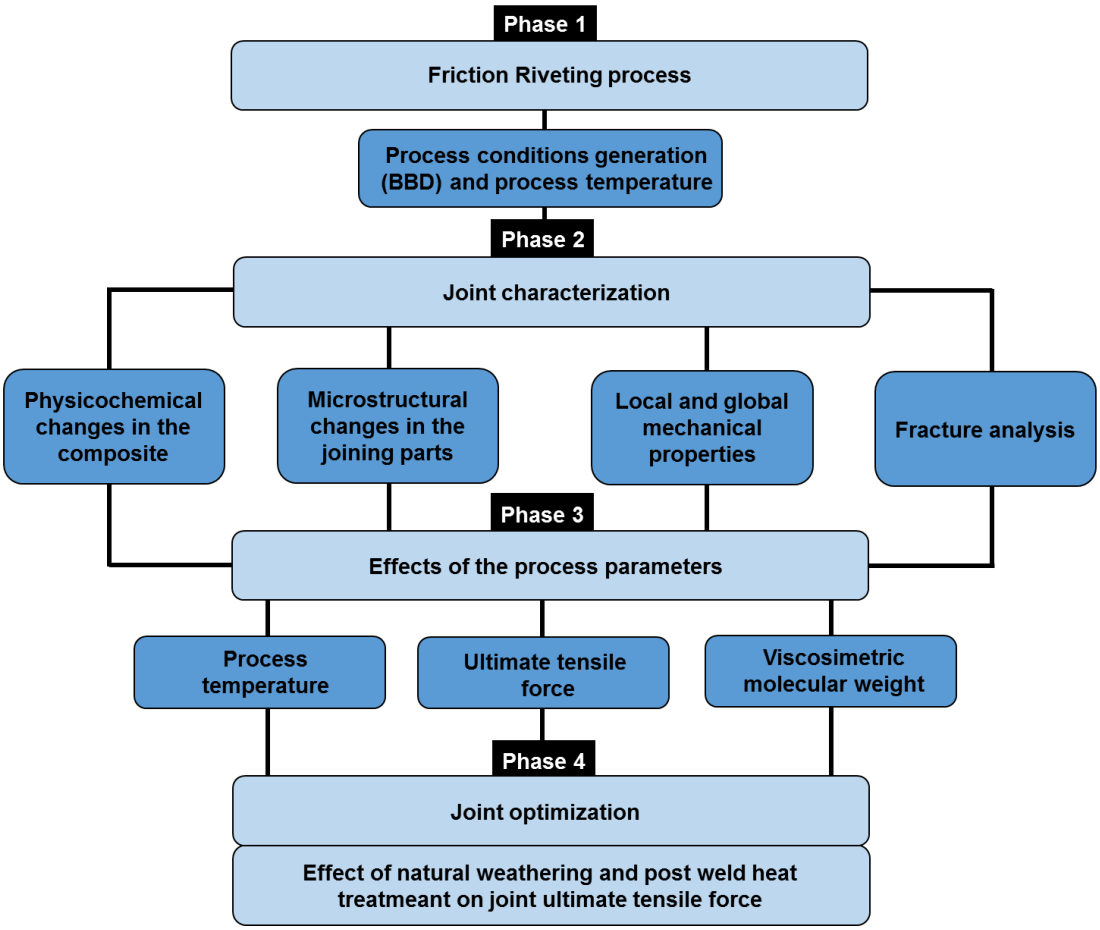

Figure 3.1 Schematic illustration of the experimental approach.

In the first phase, the process parameters screening was selected taking in account previous studies [15]. Box-Behnken Design of Experiments (BBD) and response surface methodology (RSM) were applied to generate the joining conditions and evaluate the process. The joints were produced in the metallic-insert configuration. The process temperatures along the FricRiveting process were measured using an infrared thermo-camera.

In the second phase, the characterization of the joints was carried out. In this phase, the following investigations were carried out: determination of the physicochemical changes in the composite (ATR/FT-IR, DSC and dilute solution viscosity measurements), microstructural changes in the joining parts (LOM, SEM and EBSD), investigation of local (microhardness) and global (T-pull tensile testing and X-Ray radiography) mechanical properties and fracture analysis (SEM).

In the third phase, the relationships between FricRiveting conditions and joint properties were established. The influence of process parameters (RS, DaF and JF) on the responses process temperature, ultimate tensile force of joints and viscosity average molecular weight of PA6 and its significance were determined through analysis of variance (ANOVA) and RSM. Regression models were estimated and validated for the investigated responses.

In the fourth phase, the joint was optimized in terms of ultimate tensile force and its behavior after post-weld heat treatment, and natural weathering analyzed. The validated statistical models were used to achieve an optimized friction-riveted joint.

3.2 Base Materials Characterization

The materials used in this work were provided by EJOT GmbH. Aluminum alloy 6056-T6 rivets and 30 wt% short glass fiber reinforced polyamide 6 composite plates (PA6-30GF) were used. Figure 3.2 shows their geometries and dimensions. Usually, for FricRiveting, it is suggested that the polymer plate thickness must be at least two times the rivet diameter to obtain a good rivet deformation and consequently anchoring. In a possible future application, these geometries should be adapted as well as the configuration of the joint.

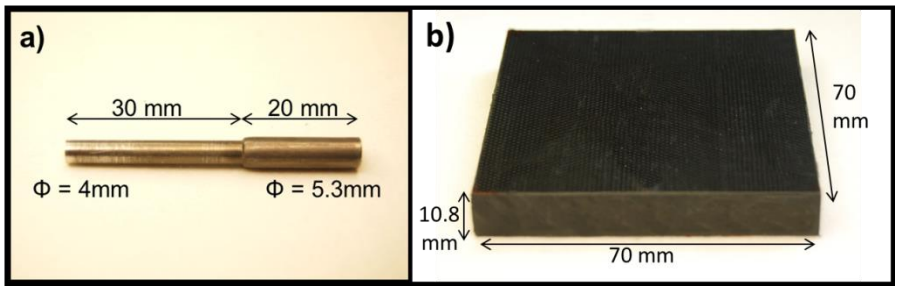

Figure 3.2 Base material: a) Metallic rivet of AA6056-T6 and b) Plate of polyamide 6 reinforced with short glass fiber.

Since there was little information on the base materials used, a preliminary characterization was performed.

In this study an AA6056-T6 solution heat treated and artificially aged extruded alloy is used for the rivets. The main microstructural characteristics of AA6056-T6 rivets used in this study were determined by optical microscope and are shown in Figure 3.3. Samples were prepared by longitudinal mid-sectioning of the rivet.

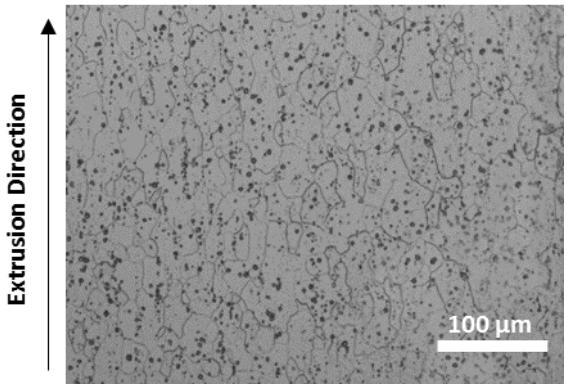

Figure 3.3 Longitudinal cross-section view of the microstructure of Aluminum alloy 6056-T6 rivets.

It can be seen from Figure 3.3 that the grains are slightly aligned to the extrusion direction. Besides, there are a high number of inclusions (secondary particles emerged from the ingot casting process). Density and Vickers microhardness measurements as well as tensile testing were performed, with the results presented in Table 3.1.

Table 3.1 Properties of AA6056-T6 as determined experimentally.

Properties	Value
Density [g/cm³]	2.65
Ultimate tensile force [N]	5320 ± 102
Microhardness [HV 0.2]	139 ± 2

The physical-chemical properties of the PA6-30GF are shown in Table 3.2. Bulk density was measured by taking the weight to volume ratio of a composite plate. Thermal properties (T_c and T_m) and the degree of crystallinity were measured by differential scanning calorimetry (DSC). Total filler (glass fiber and carbon black) content was measured by ash content method based on ASTM D3171–99 standard [70].

Table 3.2 Properties of short glass fiber reinforced PA6 composite as determined experimentally

Properties	Value
Bulk density [g/cm³]	1.38
T_c; T_m [°C]	185 ± 1; 215 ± 1
Crystallinity degree [%]	26.6 ± 0.73
Filler content [wt%]	32 ± 1

3.3 Friction Riveting Joining Equipment

The automated gantry system RNA (H.Loitz-Robotik, Germany) equipped with a commercially available friction welding head (RSM410, Harms+Wende, Germany) was used. The gantry system works with rotational speeds in the range 6000-21000 rpm and axial forces up to 24 kN. Monitoring curves from rotational speed, joining force and spindle displacement can be obtained.

3.4 Methods

3.4.1 FricRiveting Procedure

Prior to joining, the parts were cleaned to remove surface impurities like as dust or machining fluids. The rivets were cleaned with ethanol in an ultrasonic bath and the polymer composite plate was manually wiped with ethanol.

The joining procedure was divided into two controlled steps as described in Section 2.2.4. In the first step (the friction phase) the process was controlled by force and limited by displacement (position limited). The axial force was kept constant during the entire process; in other words a typical forging force higher than the friction force was not used. The theoretical forging phase (in some cases rivet may start deforming during the friction phase, as unpublished results have shown) and consolidation phase start in the second step when the rotation speed is stopped. In this last step, the process was controlled by force and limited by time.

3.4.2 Process Temperature Monitoring

The temperature evolution during the FricRiveting process was monitored on the expelled composite material flash. This temperature was considered the process temperature in this study. An infrared thermo-camera (High-end Camera Series ImageIR, Infratech GmbH, Germany) was used connected to a computer with IRBIS 3 Professional software. A temperature filter with a range between 150 °C and 700 °C was selected. The camera positioning and the focused area are schematically shown in Figure 3.4. The process temperature supported the understanding of the process-related changes on the microstructure of the metallic and polymer composite parts.

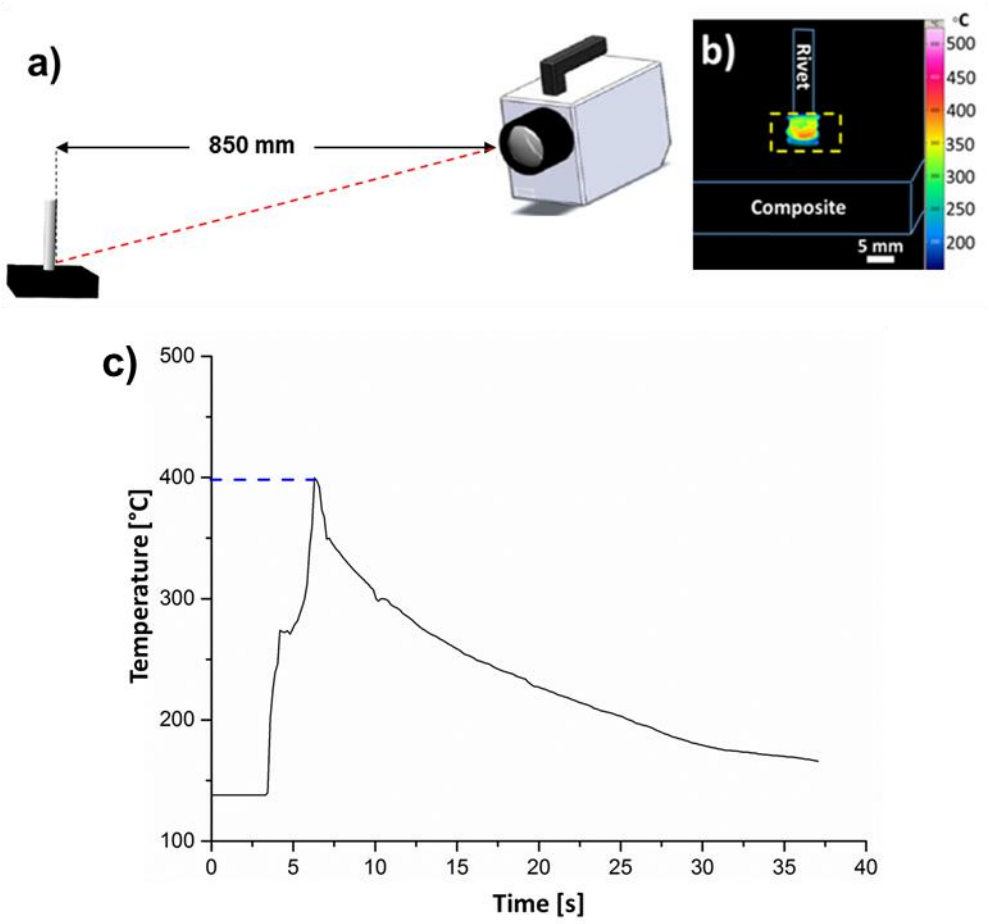

Figure 3.4 Infrared thermo-camera positioning (a), Thermogram showing the maximum temperature of the softened composite flash being expelled out of the composite plate, the yellow rectangle is the measuring area selected for software evaluation (b); Evolution of the maximum temperature during the process measured by infrared thermography adapted from [15] (c).

It should be mentioned that temperature monitoring by thermocouples was also evaluated in addition to infrared measurements. However, this procedure failed leading unreliable measurements of process temperature because of rivet motion breaking some of the thermocouples installed in the composite base plate. Moreover, due to the low thermal conductivity of the PA6-30GF, some of the thermocouples were unable to measure any variation temperature, even for cases where thermocouples have been place very close to the PTMAZ (i.e. the region experiencing the largest process temperatures).

3.4.3 X-Ray Radiography

X-ray radiography was performed according to the EN 1435 standard [71] while using a Seifert Isovolt 320/13 with a tube voltage of 60 kV and a tube current of 3.7 mA. The focus-to-film distance was 800 mm, and the focal spot was 1.5 x 1.5 mm. The joints were scanned with X-rays before mechanical testing. The X-ray images were measured using Image J software to reveal the real dimensions of the anchoring zone at the center of the joints as shown in Figure 3.5. Thus, the relation between volumetric ratio and ultimate tensile force could be investigated precisely.

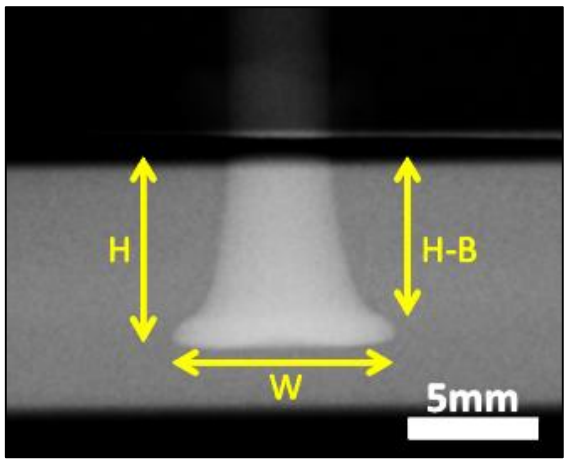

Figure 3.5 X-ray image of a friction-riveted metallic-insert joint

3.4.4 Joint Microstructural Analyses

In order to analyze the microstructure of the joints, light optical microscopy, LOM (Leica DM IRM, Germany) and scanning electron microscopy, SEM (FEI Inspect S50) were used. The analyses were performed on the cross-section of a metallic insert joint configuration. The portion of the metallic rivet outside of the composite plate was cut and a cross section near to the middle of the joint was prepared using a low speed saw with diamond blade (ISOMET, Buehler). The cut samples were embedded in low cure-temperature thermoset epoxy-resin (Epoxicure, Buehler); after that, they were ground and polished in an automatic metallographic sample preparation machine (Struers Tegramin-30).

For microstructural investigations of the joined aluminum rivet, the grain structure was revealed using chemical etching with Airbus reagent (5 mL HF in 95 mL H_2O and 10 mL H_2SO_4 in 90 mL H_2O). Due to their different metallurgical transformations, to reveal the microstructure of the BM and TMHAZ, specimens were immersed in the reagent during 5 s, while for the MTMAZ during 15 s. Nonetheless, the chemical etching did not reveal clearly the grain structure in the MTMAZ. Thus, Electron Backscattered Diffraction (EBSD) was used to provide better understanding of the process-related microstructural changes in the metallic rivet, such as annealing phenomena (dynamic recovery and recrystallization). The EBSD analyses were carried out in a thermal emission gun scanning electron microscope (FEI Inspec S50, United States) operating at 25 kV.

For microstructural investigations of the polymer composite part, only LOM was used to investigate the presence of voids and some fiber orientation owing to the joining process. LOM was also used to analyze the interface between the metal and the polymer composite.

3.4.5 Local Mechanical Properties

Vickers-microhardness measurements were performed on the metallic part of the joints prepared by materiallography. The measurements were performed using an UT100 machine (BAQ GmbH, Germany) with procedure based on ASTM E384-10 [72]. A microhardness map was created with a distance of 0.3 mm between indentations and force of 2 N during 10 seconds. Assuming the symmetry in properties of the cylindrical rivet, only half of the rivet cross-section was measured. Figure 3.6 illustrates the position of the indentations. This test supports the evaluation of the process-related microstructural transformations in the metallic rivet. Microhardness was not measured in the polymer composite part because of the presence of micrometric glass fibers randomly distributed into the PA6 matrix. Consequently, it is difficult to obtain reliable microhardness measurements for this area/material.

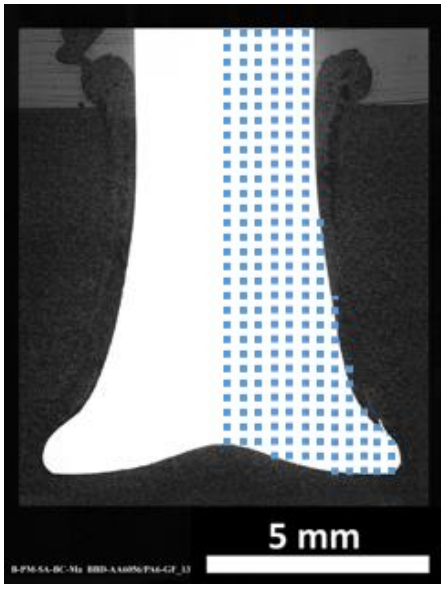

Figure 3.6 Schematic view of the indents performed on metallic part of the joint (squares).

3.4.6 Physical- Chemical Changes in the PA6-30GF Composite

Differential Scanning Calorimetry (DSC) analysis was performed in a DSC Q2000 equipment (TA Instruments, United States) based on procedures described in [73] and in ASTM D3418-08 [74]. Aluminum crucibles were used. Samples weighing between 4.5 and 5 mg with precision of ± 0.01 mg were extracted from the PTMAZ. Samples were submitted to a heating-cooling cycle in the range from 30 to 270 °C at heating rate of 10 °C min^{-1} under nitrogen flow of 50 mL min^{-1}. This procedure were applied to determine the melting enthalpy (ΔH_m), as well as the melting (T_m) and crystallization (T_c) temperatures for the composite thermo-mechanically affected (CTMAZ) zone as well for the base material.

The degree of crystallinity ($\%C$) of the PA6 samples was calculated using the Equation 2 [75].

$$\%C = \frac{\Delta H_m}{\Delta H^\circ_m (1 - W_f)} \qquad (2)$$

where:ΔH_m is the enthalpy of fusion (J/g) of the sample, ΔH°_m is the enthalpy of fusion (J/g) for 100% crystalline PA6 (190 J/g [73]) and W_f is the weight fraction of filler (glass fiber and carbon black) in the composite.

Dilute solution viscosity measurement was employed to determine the viscosity average molecular weight of polyamide 6 and then to characterize the extension of PA6 degradation caused by the FricRiveting process. Samples were taken from the flash material expelled during the process. Samples from the base material were also analyzed for comparison. The procedure was based on the ASTM D2857 standard [76] along with a methodology developed by the author [77]. The samples were properly weighed, dissolved in 85 % formic acid and filtered through a PTFE membrane (average pore size of 0.2 μm) to separate the polymer solution from the filler (glass fiber and carbon black). The weighting procedure took into account the PA6-30GF composition (32 wt% filler content; see Table 5.2) in order to obtain a PA6 solution with final concentration of 0.1 g/dL. After complete solubilization and filtration, the PA6 solution was placed in an Ubbelohde viscosimeter type 1 immersed in a bath with temperature controlled at 25 ± 0.1 °C. The intrinsic viscosity values were determined by the single point method of Billmeyer [78], which consists in determining the intrinsic viscosity using a single polymer solution concentration through the Equation 3:

$$[\eta] = (0.25 \cdot \eta_{red}) + (0.75 \cdot \eta_{iner}) \qquad (3)$$

where $[\eta]$ is the intrinsic viscosity, $[\eta_{red}]$ is the reduced viscosity and $[\eta_{iner}]$ is the inherent viscosity.

The viscosity average molecular weight ($\overline{M}_v$) of the polyamide 6 was calculated by the Mark-Houwink-Sakurada approach (Equation 4):

$$[\eta] = K \cdot \overline{M}_v^{\,a} \qquad (4)$$

where $[\eta]$ is the intrinsic viscosity and the constants K = 2.26x10^{-4} dL/g and a = 0.82 [79].

Attenuated total reflection Fourier transformed infrared spectroscopy (ATR/FT-IR) was carried out on a Varian 640 FT-IR spectrometer (Varian Inc., United States) to monitor some PA6 characteristic absorption bands and then to

evaluate the degradation level of the PA6 caused by the FricRiveting process. Samples were extracted from the flash material expelled during the joining. All spectra were acquired with 100 scans, resolution of 4 cm^{-1} and spectral range of 4000 to 500 cm^{-1}.

3.4.7 Polyamide 6 Composite Integrity

Optical microscopy was used to analyze the breakage of the fibers in the PA6-30GF composite caused by the FricRiveting process. The samples were taken from flash expelled during the process and from the base material for comparison. The lengths of the glass fibers were determined by use of image analyzer software (Image J software). The glass fibers were recovered from the separation procedure described in Section 3.4.6. The fibers were distributed over a glass plate with the aid of a 1:1 solution of distilled water and ethanol and then left to a hot plate until the complete evaporation of the solution. Around 1000 fibers were counted for each condition following the approach reported in [80-82]. The number average length (l_n), the weight average length (l_w) and the polydispersity index (*P*) of the glass fibers were calculated using Equations 5, 6 and 7, respectively, where (n_i), is the number of glass fibers with length l_i and $\sum_{i=1}^{N} n_i = N$ is the total number of glass fibers.

$$l_n = \frac{\sum_{i=1}^{N} n_i \cdot l_i}{\sum_{i=1}^{N} n_i} \quad (5)$$

$$l_w = \frac{\sum_{i=1}^{N} n_i \cdot l_i^2}{\sum_{i=1}^{N} n_i \cdot l_i} \quad (6)$$

$$P = \frac{l_w}{l_n} \quad (7)$$

Finally, the aspect ratio of the glass fibers of the flash material were compared with the critical value $(L/D)_c$ from Kelly-Tyson model (Equation 8) [83]

$$\left(\frac{L}{D}\right)_c = \frac{\sigma_f}{2\tau_{\text{int}}} \qquad (8)$$

where: L is the length of the fiber, D is the diameter, σ_f is the tensile strength of the fiber and is τ_{int} interfacial shear stress. The value of τ_{int} can be approximated to the value of the shear stress of the polymer matrix by assuming that there is perfect adhesion between the fiber and the polymer. Taking into account that the shear stress values for PA66 are around 45 MPa [80] and considering a typical value for the fiber strength of 1500 MPa [80], it results that the critical fiber aspect ratio is 16.7. Considering that average glass fiber diameter is 10 µm, hence, the critical fiber length for the effective reinforcement of the PA6 used in this work is 167 µm.

3.4.8 Quasi-Static Global Mechanical Performance

Tests were performed on T-Pull tensile specimens [65] (Figure 3.7-a) in a universal testing machine Zwick/Roell equipped with a load cell of 100 kN with crosshead speed of 1 mm.min^{-1} at room temperature (21 °C). The sample holder for the T-pull tests is schematically illustrated in Figure 3.7-b.

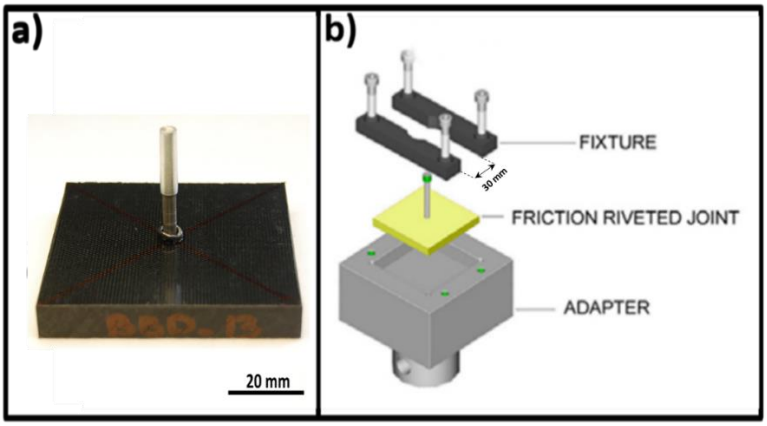

Figure 3.7 T-Pull AA6056/PA6-30GF specimen (a) and Schematic representations of the joint sample holder (b) [84]**.**

3.4.9 Fracture Analysis

Scanning electron microscopy (SE-SEM, model Quanta FEG 650, FEI, USA) was carry out under secondary electrons detection mode to observe the joint fracture surfaces. The selected fractured joints were sputtered with gold. SEM analysis was performed at 5 kV; working distance of 19.5 mm for the composite part and 15 mm for the metallic part; atmosphere pressure of 0.001 Pa. This technique helped to evaluate the types of fracture micromechanisms (e.g. ductile or brittle behavior) that occurred on the tested joints.

3.4.10 Effect of Process Parameters on Joint Properties

The process parameters used in this work were Rotational Speed (RS), Displacement at Friction (DaF), Joining Force, JF (Friction Force equal to Forging Force), and Forging Time (FoT). The range and level of each parameter is shown in Table 3.3. The Forging Time (FoT) was kept constant at 3 s since this parameter did not affect the anchoring zone formation. The value of the FoT was selected from preliminary feasibility studies.

Table 3.3 Parameters range used to obtain the AA6056-T6/PA6-30GF joints.

	Process parameters		
Levels	Rotational Speed [rpm]	Displacement at Friction [mm]	Joining Force [N]
Minimum (-1)	14000	8	1600
Maximum (+1)	16000	10	2200

A statistical approach was chosen to evaluate the individual effects of the process parameters and their interactions on flash temperature, ultimate tensile force and viscosity average molecular weight. The design of experiment chosen was the Box-Behnken Design (BBD) with 3 factors [85]. The joining conditions (runs), were generated using Minitab and Statistica software with the parameter range shown in Table 3.4. The BBD is an efficient design because it allows a good analysis of the process with a few numbers of runs in comparison with other designs of experiment [86]. The BBD has been used in many areas, from chemistry [86] to welding studies [87-91]. The significance of the effects of factors on the responses was evaluated using evaluate (ANOVA). The factors were

considered statistically significant using 95 % of confidence interval (α=0.05) and slightly statistically significant using 90 % of confidence interval (α=0.1).

Table 3.4 Combinations of parameters resulted from the BBD for the AA6056-T6/PA6-30GF friction-riveted joints.

	Process parameters		
Conditions designation	Rotational Speed [rpm]	Displacement at Friction [mm]	Joining Force [N]
C1	16000	10	1900
C2	15000	8	1600
C3	14000	9	1600
C4	15000	8	2200
C5	14000	9	2200
C6	14000	8	1900
C7	14000	10	1900
C8	15000	10	2200
C9	15000	9	1900
C10	16000	9	1600
C11	15000	9	1900
C12	15000	10	1600
C13	16000	9	2200
C14	16000	8	1900
C15	15000	9	1900

Regression models for the responses were obtained with Minitab and Statistica software. The regression models were reduced considering only the statistically relevant factors determined from ANOVA tables. The reliability of the models was evaluated using the adjusted coefficient of determination, R^2_{adj}. The correlation of predicted data by the model with experimental data is considered very good when the value of R^2_{adj} is near to 1.

3.4.11 Post Joining Heat Treatment

The FricRiveting process leads to metallurgical transformations that might decrease or increase joint mechanical properties of the joints. For precipitation hardenable aluminum alloys (e.g. Al 2XXX and 6XXX series) undermatching of properties (decrease in mechanical properties) is a common phenomenon in FricRiveting [10,84]. Post joining heat treatment (PJHT) can partially recover the original precipitate distribution and consequently alter the strength and ductility of

aluminum [92] Based on that, a PJHT was performed to improve the global mechanical property of the optimized joint (C13). The PJHT used was the artificial aging treatment selected from literature [93]. An example of PJHT diagram in this work is shown in Figure 3.8. A set of joints was heated in an oven (P330 from Nabertherm-GmbH) from 20 ^{o}C up to 180 °C at 150 ^{o}C h^{-1} and kept at this temperature for 6 hours. Afterwards, the joints were cooled outside of the oven to room temperature (23 °C). After 72 hours these joints were submitted to T-pull tensile testing. The joints were weighted before and after the test to obtain the water uptake during the PJHT. Microhardness on the metallic part and DSC of the polymer composite were performed to better understand the effect of PJHT on the local mechanical properties and polymer degree of crystallinity.

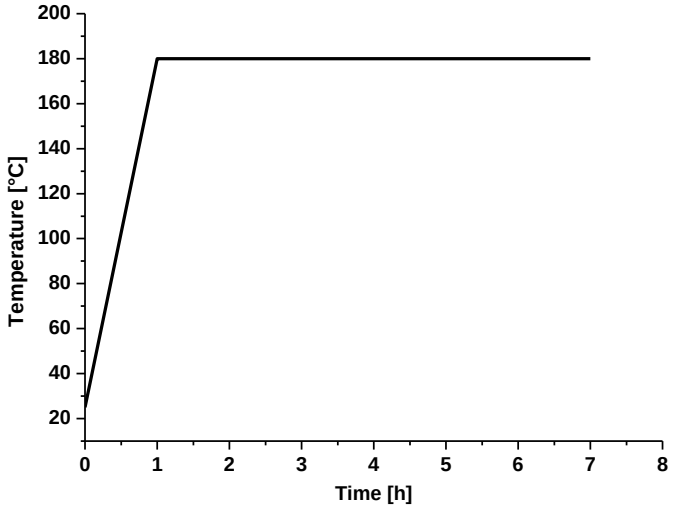

Figure 3.8 Example of a post-joining heat treatment cycle used to treat a selected set of friction riveted joints (conditions C13).

3.4.12 Natural Weathering

The natural weathering tests were performed on a set of joints at HZG for a testing times of 6 and 12 months to evaluate the effect of environmental conditions (i.e. ultraviolet (UV) radiation, humidity, temperature, pollutants, and other factors) on the ultimate tensile force. Figure 3.9 shows the testing jig where the tests were conducted based on ASTM D1435-13 [94]. The joints were weighted before and after the test to obtain the water uptake during the natural weathering. Dilute solution viscosity measurements were performed on polymer taken from the flash of these joints to analyze the extension of degradation. The

weathering data were obtained online at Weather Undergroung (https://www.wunderground.com/). Detailed data for the Geesthacht weather in the period of the experiments is shown in Appendix A.

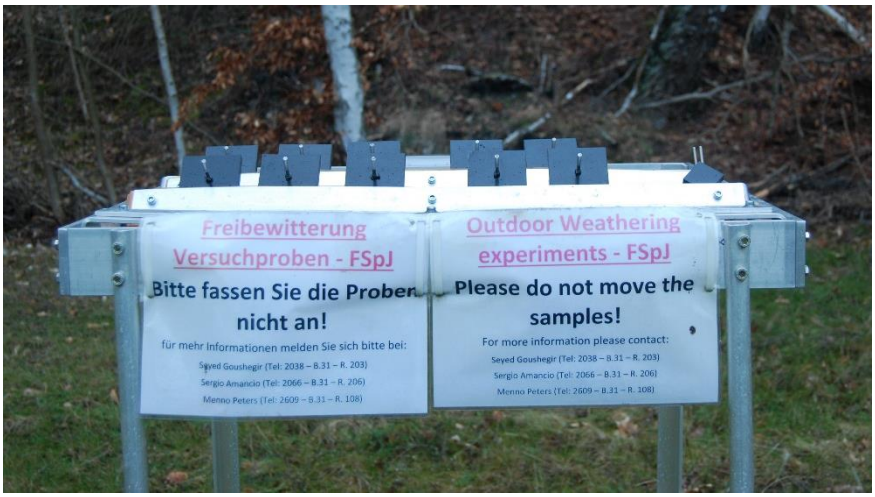

Figure 3.9 Natural weatherability testing jig for the friction-riveted AA6056-T6/PA6-30GF joints.

4 RESULTS AND DISCUSSION

4.1 General Aspects of Joint Formation in Friction Riveting

Friction-riveted joints were produced using two-process phases described in Section 3.4.1. Figure 4.1 shows an example of the process monitoring diagram for the FricRiveting joining cycle with this process variant for the joint produced with condition C13 (Table 3.4). For this condition the rotational speed was set to 16000 rpm, displacement at friction to 9 mm and joining force to 2200 N. The forging phase (second phase) had the duration of 3000 ms (FoT= 3000 ms). This condition was selected because combines a high shear (higher value of rotational speed) with a high strain rates (higher value of joining force). The following sections describe the positive effect of it on the heat generation, anchoring zone formation and global mechanical properties.

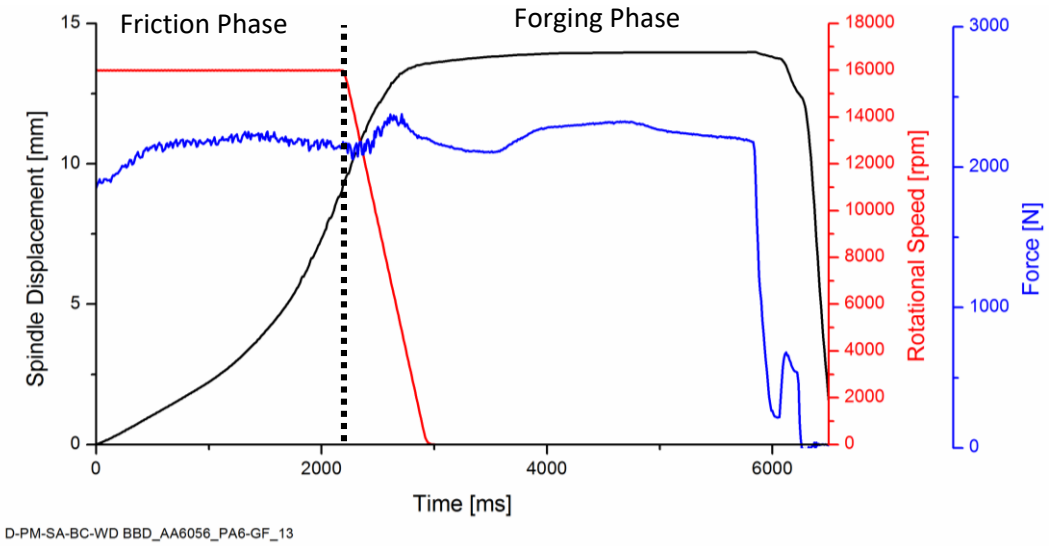

Figure 4.1 Process monitoring diagram for condition C13 (RS: 16000 rpm, DaF: 9 mm, JF: 2200 N).

The process temperature for the BBD conditions showed a wide spread difference between the minimum and maximum measured values and it had direct influence on the formation of the anchoring zone. Figure 4.2 shows the process temperature and volumetric ratio for the joints produced with fifteen BBD conditions. In terms of process temperature the minimum value was 323 °C for condition C3 and the maximum value was 399 °C for condition C13. In terms of

anchoring efficiency the minimum value for volumetric ratio was 0.35 for condition C3 and the maximum value was 0.72 for condition C13.

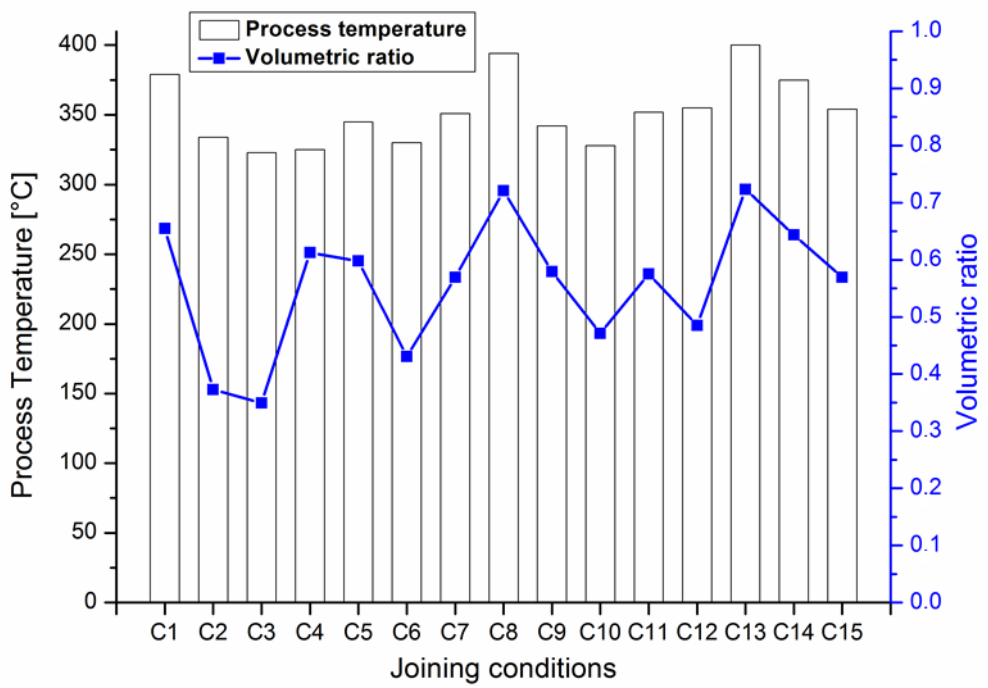

Figure 4.2 Maximum temperature and volumetric ratio for the joints produced with fifteen BBD conditions.

Figure 4.2 shows that process with low temperatures generated joints with low anchoring efficiency. The level of deformation is related to the heat generated during the process which follows the Equation 9 [95]:

$$Q_{total} = \left[\left(\frac{l_w}{l_n} * \mu * P_{(r)}\right) + \frac{\eta * V_{max}}{H}\right] * V_{max} \qquad (9)$$

Where: Q_{total} is the total heat input in the joint area, μ the kinematic friction coefficient, P(r) the normal pressure distribution on the tip of the rivet, η the molten polymer viscosity, V_{max} the maximal tangential speed of the rivet obtained from the angular speed (w) and the radius of the original rivet (R): $w = V_{max}/R$, and H the average width of the consolidated polymeric layer. This equation considers that the heat input is generated mainly by friction; in thermoplastics it is related to viscous dissipation (internal shearing in the molten polymer) [95].

Figure 4.3 shows the cross section for three selected joints produced with low, medium and high heat inputs by concomitantly increasing RS and JF (see

Table 3.4). The joints in Figure 4.3-a, Figure 4.3-b and Figure 4.3-c were obtained with a low (C3), medium (C9) and high (C13) heat input respectively.

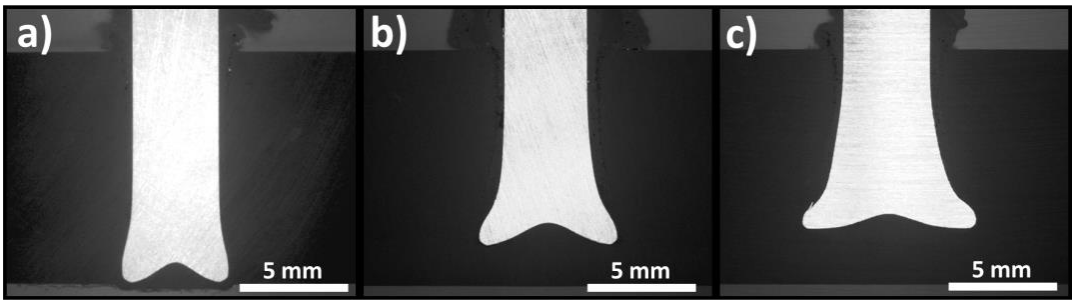

Figure 4.3 Cross section of AA6056-T6/PA6-30GF joints – selected conditions: C3 (RS = 14000 rpm, DaF = 9 mm and JF = 1600 N) (a), C9 (RS = 15000 rpm, DaF = 9 mm and JF = 1900 N) (b) and C13 (RS = 16000 rpm, DaF = 9 mm and JF = 2200 N) (c).

The maximum temperatures achieved for these conditions were C3 = 323 °C, C9 = 342 °C and C13 = 399 °C. Therefore, the deformation on the tip of the metallic rivet is greater for joints with a higher heat input. This occurs because higher temperatures lead to larger plasticized volumes at the tip of the metallic rivet, thus resulting in a greater deformation.

4.2 Process-Related Changes in the Materials Joined by Friction Riveting

The previous section described the influence of the heat input on joint formation, precisely on the formation of the anchoring zone. The interaction of the rivet with the polymer generates frictional heat that in combination with a force affect both joining parts. During the process, the metallic rivet suffers plastic deformation while the polymer matrix of the composite melts. This section describes the changes in the microstructure and local mechanical properties of metallic and polymer composite parts. Figure 4.4 exemplifies the microstructural zones of the AA6056-T6/PA6-30GF joints. The limit between the polymer heat-affected zone (PHAZ) and the base material could not be identified by optical microscopy or Vickers microhardness measurements.

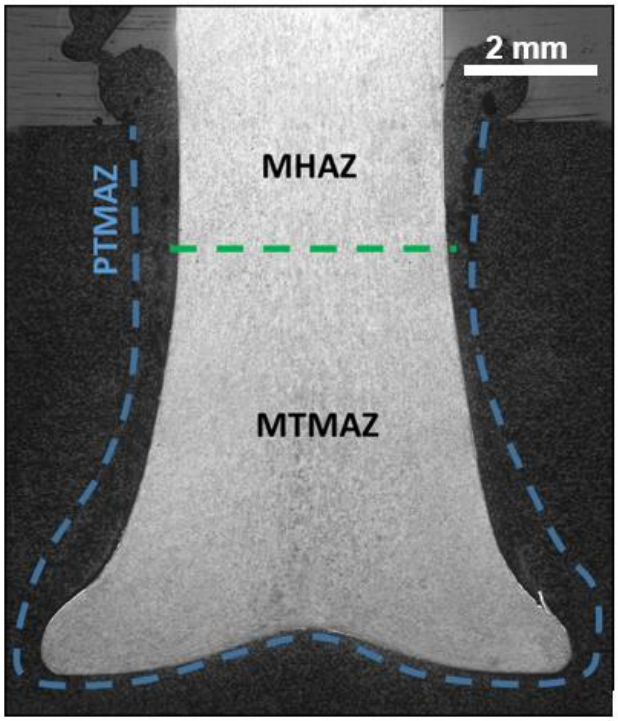

Figure 4.4 Microstructural zones of a FricRiveted AA 6056-T6/PA6-30GF joint C13 (16000 rpm, 9 mm and 2200 N).

4.2.1 Changes in the Metallic Part of Friction-Riveted Joints

Figure 4.5 shows the affected zones of the metallic rivet. As observed for the base material (Section 3.2) the selected etching procedure could not perfectly reveal the joints' rivet microstructure. Nevertheless, it is possible to observe that the grains are aligned in the direction of the deformation in the MTMAZ; furthermore, partial grain refinement can be also observed. The refinement in the microstructure during the process might be occurring by dynamic recovery and continuous dynamic recrystallization (CDRX), as already reported for FricRiveting [65], by the formation of dislocation cells and sub grains inside of the deformation bands in a similar manner as described for equal channel angular pressing (ECAP) [96]. It is known that recovery and recrystallization are excluding each other. Also, the preferable annealing phenomenon for aluminum is the recovery due to the high stacking fault energy of it. Even though in aluminum alloys, due to the presence of the precipitates, the stacking fault energy is reduced and also the movement of dislocations is stopped. This allows the recrystallization

phenomenon to occur at high temperatures (usually process temperature higher than 50 % of the alloy melting temperature) and higher shear rates (10^{-1}-10^{-3} s^{-1}) [96]. In the MHAZ, no microstructural change in comparison to the base material (Figure 3.3) has been observed by LOM. However, the temperature achieved within this area may induce microstrutural changes that are only visible using a transmission eletron microscope, such as static recovery and solubilization of the precipitates [10,84].

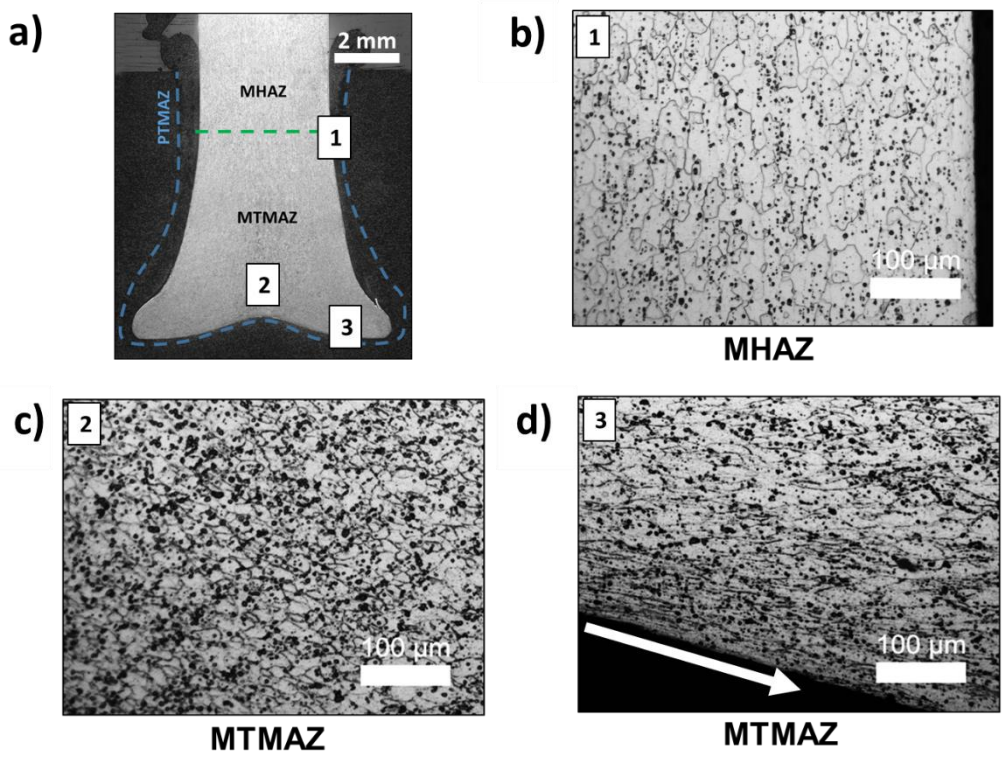

Figure 4.5 Microstructural zones of a friction-riveted AA 6056-T6/PA6-30GF joint C13 (16000 rpm, 9 mm and 2200 N) (a); Detailed microstructural zones of joint's metallic rivet: Detail of the Heat Affected Zone of the metal, MHAZ (b); Thermo-Mechanically Affected Zone of the metal, MTMAZ (c), and the realignment of the grains in the direction of the material flow in the bottom of MTMAZ (d).

EBSD analysis was performed to improve the observations from LOM results. Using this technique, metallurgical phenomena, such as dynamic recovery and recrystallization, can be observed and measured. Figure 4.6 shows the inverse pole figures (IPF) for the base material (Figure 4.6-a), MHAZ (Figure

4.6-b) and MTMAZ (Figure 4.6-c) in the metallic rivet of joint condition C13. The grains were colored according to their crystallographic orientation. In Table 4.1 the fractions of low angle boundary (LAB) for each area is presented.

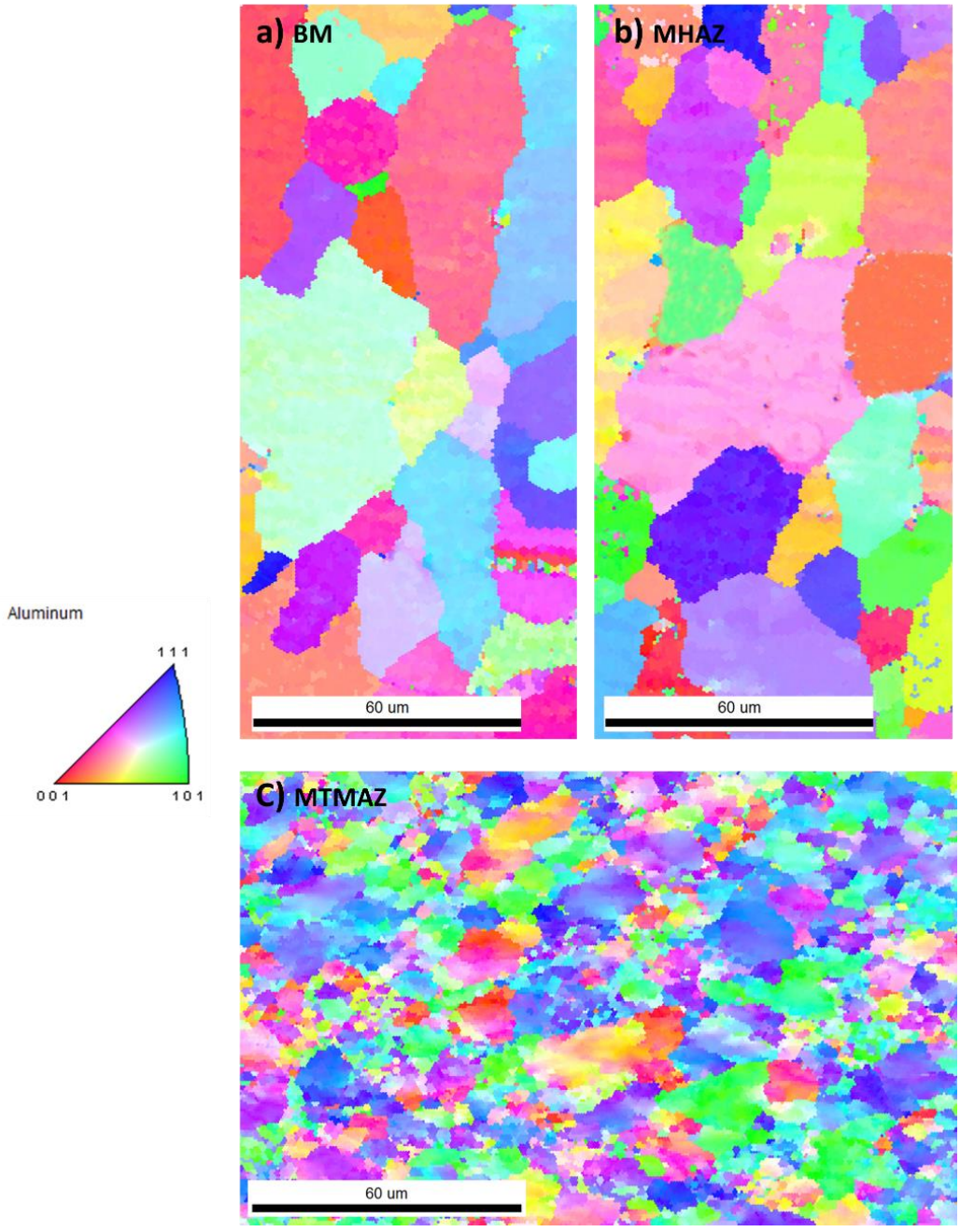

Figure 4.6 Crystallographic orientations of base material (as-received rivet) (a), metal-heat-affected (b) and metal-thermo mechanically-affected-zones (c) are detailed through EBSD maps. Condition C13 was used.

Table 4.1 Fraction and low-angle boundaries of regions shown in Figure 6.6.

Region	LABs (2-15°) [%]	Covered area [µm^2]
Base material	49.1	14104
MHAZ	45.2	14924
MTMAZ	62.5	16720

Comparing Figure 4.6-a, b and c the assumption from the LOM observations can be validated. No relevant differences between BM and MHAZ are observed while partial grain refinement can be also observed on MTMAZ due to the plastic shear deformation and high process temperatures. The percentage of LAB increased in the MTMAZ in comparison to the BM; this indicates that dynamic recrystallization may be occurring in this region [96, 97].

The annealing phenomena (dynamic recovery and recrystallization) in FricRiveting has been reported to cause significant decreases in local mechanical properties (e.g. Vikers microhardness) of precipitation hardenable aluminium alloys. Amancio *et al.* [84] reported a hardness undermatching of 10 % on the MHAZ and 15 % on the MTMAZ PEI/AA2024-T351 in relation to the base material. Rodriguez *et al.* [10] reported a decrease in hardness of 12% on the MHAZ and 31 % on the MTMAZ PC/AA2024-T351 in relation to the base material. Figure 4.7 shows the microhardness map of the rivet base material and for condition C13.

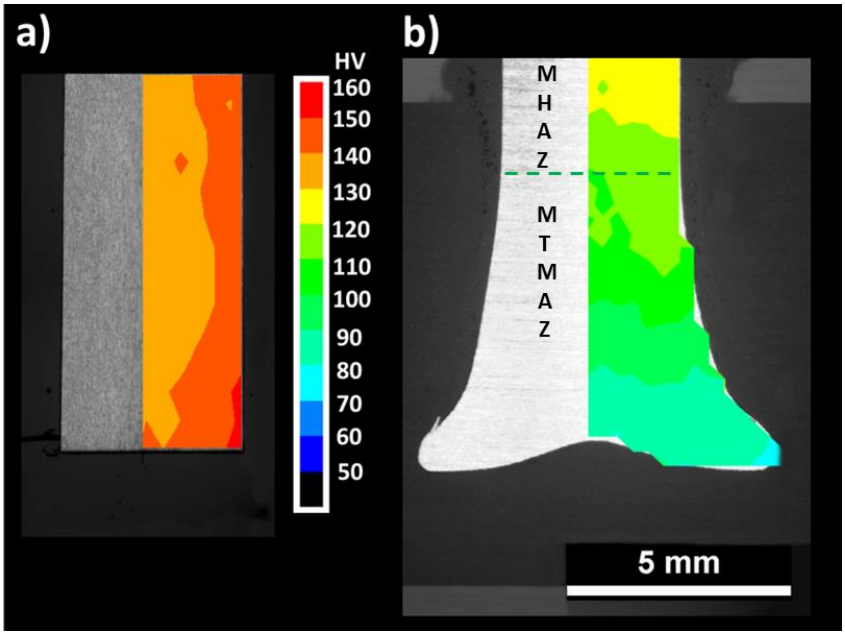

Figure 4.7 Microhardness map: Base material (a) and Condition C13 (16000 rpm, 9 mm and 2200 N) (b).

A significant decrease in the microhardness of the rivet before and after the FricRiveting process can be observed in Figure 4.7. In the MTMAZ (Figure 4.7b) the microhardness decreased by 40 % compared with the base material. In the MHAZ (Figure 4.7b), the decrease in microhardness is smaller (21 %). In the case of AA6056-T6, the main factor that affects the strength/hardness is the presence of precipitates. The base material used is already artificially heat treated (T6), whereby the precipitates are already in the aluminum matrix helping with the alloy strengthening. For AA6XXX, a decrease in hardness has been reported for other friction-based joining process, such as friction stir welding [93,98,99]; hardness undermatching has been reported to be associated with the dissolution of precipitates as a result of high process temperatures and strain rates. As discussed earlier other annealing phenomena such as, dynamic recovery and recrystallization might be also occurring as indicated by the microstructural changes shown in Figure 4.6.

The determination of local mechanical properties provides an important relation between process-structure-properties. The variation in the microhardness values supported the microstructural changes discussed above. Tabor has proposed a correlation between hardness and yielding stress (HV ≈

3Y) [100]; therefore a decrease in the hardness implies a the decrease of the local joint strength. This will be further discussed in Section 4.3.

4.2.2 Changes in the Polymer Composite Part of Friction-Riveted Joints

4.2.2.1 Defects in the Polymer Composite Affected Zones

The FricRiveting is a severe thermo-mechanical process to the polymeric part because of the high heat generated and shearing imposed by the rivet during the process. Figure 4.8 shows the thermo-mechanically affected zone of the polymer composite (abbreviated as “CTMAZ” to differ from the PTMAZ for unreinforced polymer) on the region 1 of Figure 4.5.

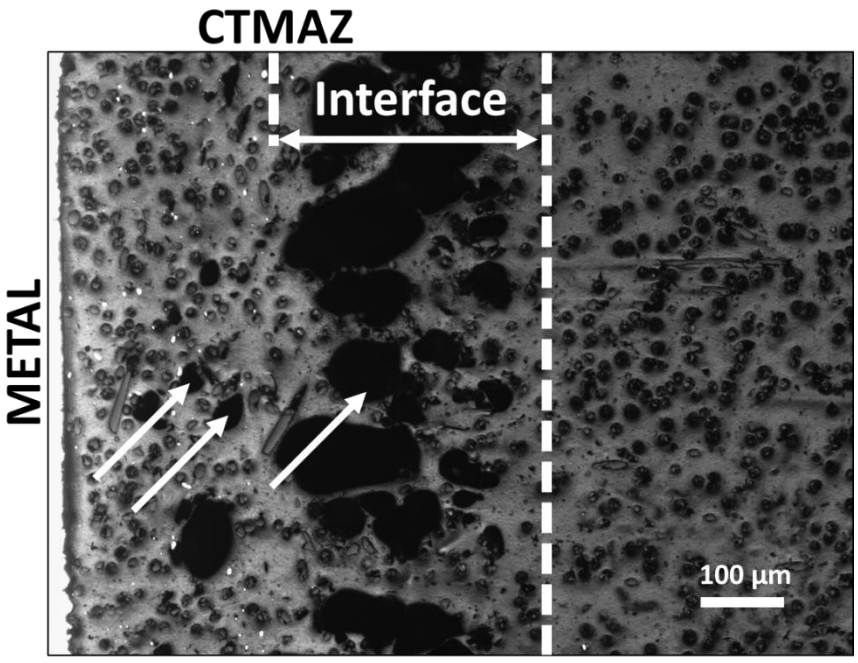

Figure 4.8 Detail of the composite thermo-mechanically affected zone (CTMAZ) showing the presence of voids (marked with arrows) in the CTMAZ and in the interface with the CHAZ.

In Figure 4.8, an intimate contact is observed between the polymer composite and metal, which indicates that their interface is possibly sealed. The presence of voids (see arrows in Figure 6.8) and the reorientation of the glass fibers are also seen, as well as the presence of a large number of voids at the interface between the CTMAZ and CHAZ. The presence of voids in the CTMAZ

can be related to the process-related evolution of water and additives of the polymer matrix, and partial thermos-mechanical degradation of the matrix [28].

Apart from being formed by the phenomena previously described, the voids at the interface of the CTMAZ and CHAZ may be generated due to the interaction between the molten composite and the rotating rivet. This interaction is known as the Weissenberg effect [101] and it occurs due to the elasticity of the fluids. This effect of elasticity is generated during shear flow because of normal stresses [102-104]. Basically, this phenomenon is observed when a spinning rod is inserted into a solution of non-newtonian fluid. Instead of being thrown outward like in newtonian fluids (Figure 4.9a), the solution climbs the rod due to the positive normal force (Fn) (Figure 4.9b).

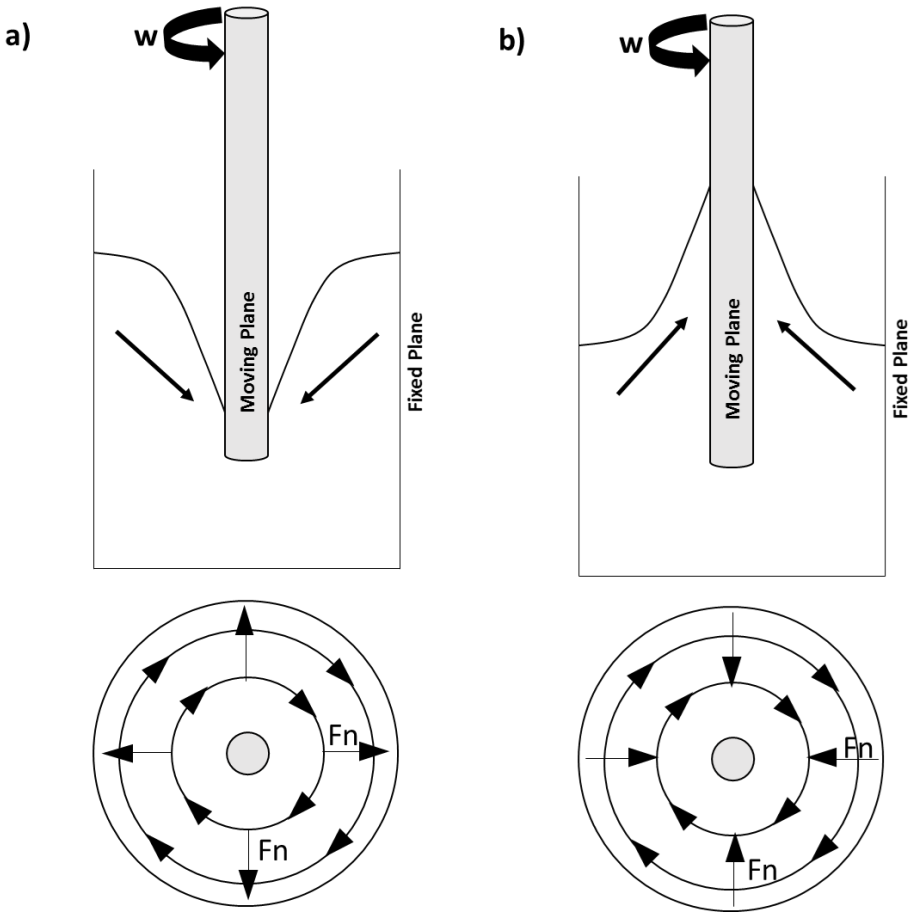

Figure 4.9 Scheme of: rod-climbing experiment with a non-newtonian fluid (a) and with a newtonian fluid (case of Friction Riveting) (b).

In the case of FricRiveting, the rod (rivet) is not only rotating with high tangential speeds inside of a non-newtonian fluid (CTMAZ) but it is also been inserted into the polymer composite plate. Therefore, the rheological assumptions and conclusions should be deeper investigated in further studies. Nonetheless, the FricRiveting process was recorded using a high-speed camera to analyze the behavior of the flash expelled during the process, in order to help proving correlations with the Weissenberg effect. Figure 4.10 shows a sequence of screen shots taken from the high-speed video; it is obvious that the flash is not just being expelled randomly but it is climbing the rotating rivet.

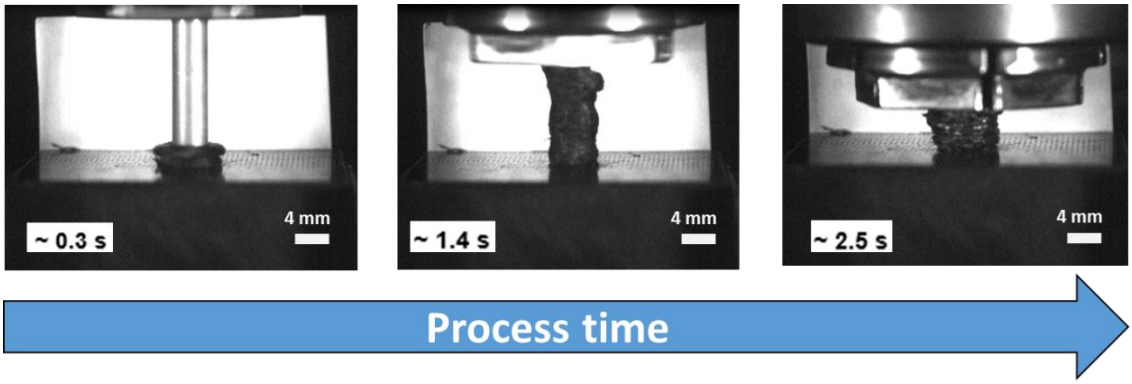

Figure 4.10 Sequence of screenshots taken from a high-speed camera video where it is observed the flash climbing the rotating rivet.

Figure 4.11 shows schematically how the Weissenberg effect might be generating defects in AA 6056-T6/PA6-30GF joints. The normal forces related to the Weissenberg effect (white arrows in Figure 4.11-a) together with the upward force related to the squeeze flow contributes to the generation of a thin layer of voids between CTMAZ and CHAZ. The layer of defects is thicker close to the top composite plate, since this region interacts longer with the metallic rotating rivet. Thus, the effects of the normal forces seems to be more prominent in this region (Figure 4.11-b). Additionally, the squeeze flow might be also pushing bubbles from the related water evolution, additives and degradation products to this region. The rheological theories should be deeper investigated in further studies to confirm these assumptions in friction-riveted joints.

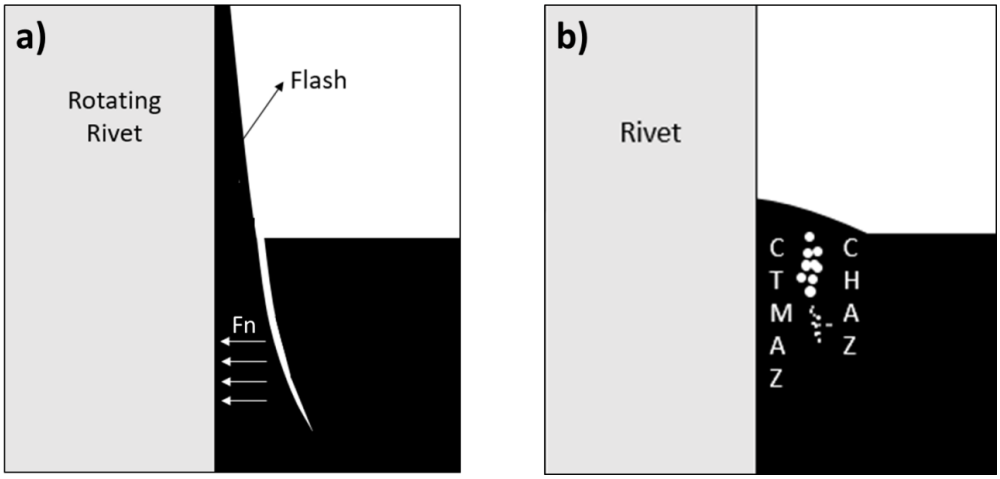

Figure 4.11 Scheme for the generation of defects in AA 6056-T6/PA6-30GF joints caused by Weissenberg effect: During the friction phase of the joining process (a) and after the friction phase of the joining process (b).

Figure 4.12-a and Figure 4.12-b show, respectively, the interface between metal and polymer composite for the zones 3 and 2 of Figure 4.5.

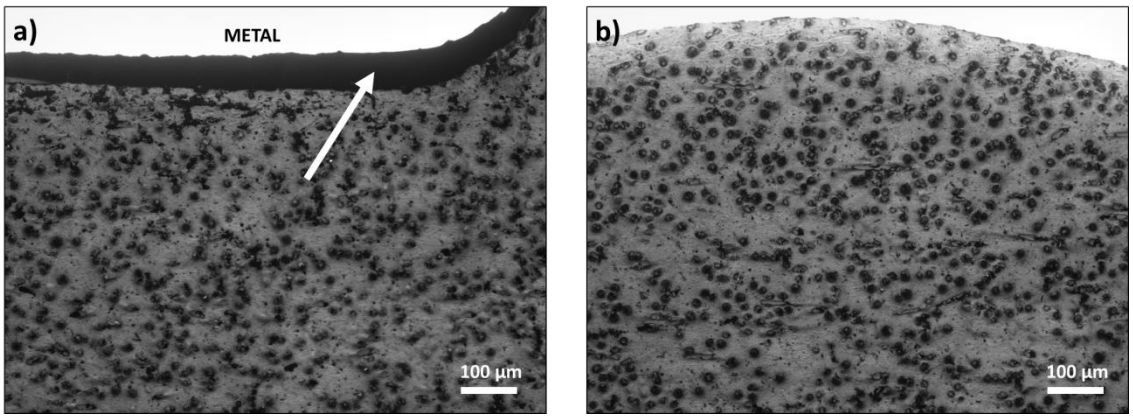

Figure 4.12 Detailed interface zones: small gap under the anchoring zone leg (a) and the gap is absent under the center of the anchoring zone (b).

In Figure 4.12-a, a small gap underneath the leg of the anchoring zone can be seen at the composite - metal interface, while in Figure 4.12-b an intimate contact underneath the center of the anchoring zone is observed.

There are two main assumptions to be taken into consideration to explain the presence of the gap at the composite-metal interface. Firstly, the gap is a result of differential contraction between consolidated polymer composite and metal. Secondly, the elastic recovery at the legs of the anchoring zone after thermo-mechanical plastic deformation. The spring-back phenomenon is defined

by the elastic recovery of a metal being stretched (i.e undergoing compression and tension) tending to return to its original position after loading is removed [105]. Considering that at higher temperatures (i.e. warm forming conditions) formability is increased (the initial yielding stress is decreased) reducing spring-back. For aluminum alloys of the AA 6XXX series, temperatures above 250 °C show reduced elastic recovery [106,107]. Considering that our range of process temperature are well above the warm forming range of AA 6XXX series, spring-back can be probably ruled out. Therefore, the presence of the gap underneath the leg of the anchoring zone may be related to the large differential shrinkage between consolidate CTMAZ material (38 µm/m°C [35]). and rivet (23.4 µm/m°C [27]).

The issue regarding the large differential shrinkage between the materials is not observed in the center of the anchoring zone (Figure 4.12-b). The intimate contact between polymeric material and metal in this region could be occurring due to two reasons. Firstly, during the consolidation phase Joining Force is kept constant and, as the shape of the deformed rivet tip varies, the pressure distribution is not uniform at the tip of the deformed rivet, as shown in Figure 4.13-a.. Secondly, differences in crystallinity in the PTMAZ may occur during the consolidation phase because the shear and heat generation (i.e. the process temperature) in the area under friction is non-homogeneous [65,95] (see Figure 4.13-b) and dependent on the tangential speed ($V_{(r)}$) (which is directly proportional to the rivet radius). It is known that semi-crystalline polymers like PA6 may suffer differential contractions related to different local rates of heating and cooling. It is also known that shrinkage is directly proportional to the percentage of the crystalline phase that might be induced by shear [28]. Nevertheless, these differences in percentage of crystallinity and recrystallized volume are very difficult to determine or predict in FricRiveting; for simplification one may assume that no large variations in the distribution of crystallinity and volume of recrystallize composite will occur at the interface area along the radius of the rivet tip. Therefore recrystallization-dependent shrinkage will be probably reduced or absent in the PTMAZ volume underneath the AZ. Based on these assumptions, the differential shrinkage leading to the gap formation is basically a result of the

non-uniform pressure distribution, which compensates the large contraction of the PTMAZ composite material at the center rivet portion underneath the AZ.

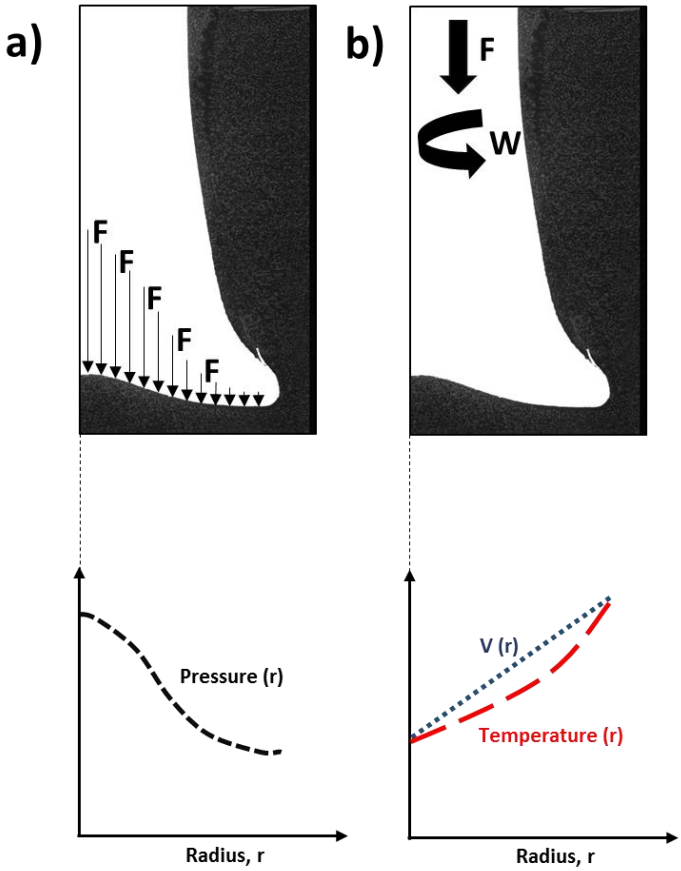

Figure 4.13 Schematic Illustration for the pressure distribution in the cross-sectional area of the rivet tip (a) and tangential speed ($V_{(r)}$) and process temperature at the rivet tip (b). The shape of the temperature curve is arbitrarily defined.

Therefore, the defects generated in the polymer composite affected zones are not only caused by the high temperatures and/or high shear rates inducing thermo-mechanical degradation. The interaction between the metallic rivet and the molten polymer inducing chain recovering (associated to the Weissenberg effect, Figure 4.10), and the differential shrinkage must be considered because it will directly influence the formation of voids and gaps during the friction and consolidation phases. These assumptions must be further studied, for instance with the aid of finite element analysis and stop action procedures to validate these conclusions.

4.2.2.2 Physical-Chemical Changes in the Polymer

The physicochemical changes of the polymeric part were investigated through DSC, viscosity measurements and ATR/FT-IR analysis as described in Section 3.4.6. These investigations are important because the mentioned changes may influence the joint strength and behavior. As described in Section 2.2.4, the volume defined theoretically by the Volumetric Ratio will interact directly with the metallic rivet. The polymer above the anchoring zone should have unaltered mechanical properties (free of voids or flaws) to support the load applied during the T-pull tensile testing.

Viscosity measurements were performed with samples taken from the flash expelled during the FricRiveting process for all BBD conditions and base material. Figure 4.14 shows the viscosity average molecular weight of PA6 for each of the welding conditions, together with the base material. Generally, the process induced an average reduction in the viscosity average molecular weight of 10 ± 4 % for all the samples in relation to the base material, which is assumed to be due to thermo-oxidative degradation of PA6 (chain scission) during FricRiveting. It should be mentioned that PA6-30GF parts were not dried before the joining and the FricRiveting process was performed in an oxidative environment (normal atmosphere) presenting an average water content of 0.35 ± 0.03 %. Hence, these boundary conditions may have contributed to increase the loss in molecular weight of the polyamide 6. Further studies are necessary to understand the influence of initial amount of structural water as well as the environment prior to joining. However this is out of the scope of this work.

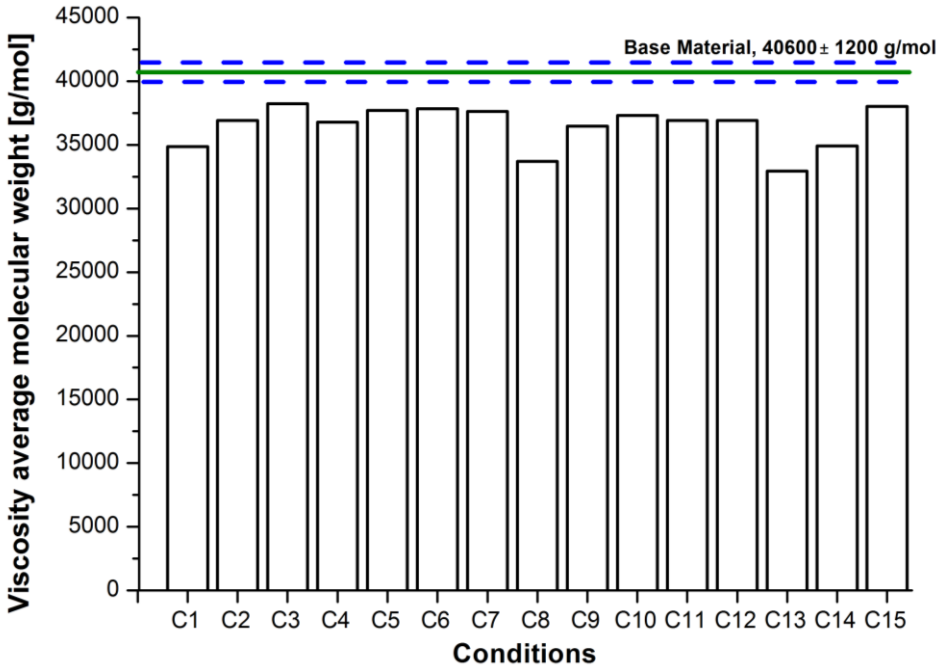

Figure 4.14 PA6 viscosity average molecular weight of samples taken from the flash expelled during FricRiveting of joints produced with the fifteen BBD conditions.

Figure 4.14 shows that the sample taken from the joining condition C13 (highest heat input) had a larger reduction in viscosity average molecular weight (33,100 $g.mol^{-1}$), which represents 19 % reduction as compared to the base material (40,600 $g.mol^{-1}$). The sample taken from condition C3 (lowest heat input) had only a minor reduction on the viscosity average molecular weight of PA6 (38,000 $g.mol^{-1}$) with 6 % of reduction in relation to the base material. The temperature achieved during the process and how this temperature was reached will determine the level of thermo-oxidative degradation of PA6 in the joints. Figure 4.15 shows the relationship between viscosity average molecular weight of PA6 and process temperature for the joints produced with BBD joining conditions. As it was expected, the viscosity average molecular weight decreases almost linearly with the increase in the process temperature. The influence of the process parameters on the process temperature and viscosity average molecular weight are discussed in the following sections.

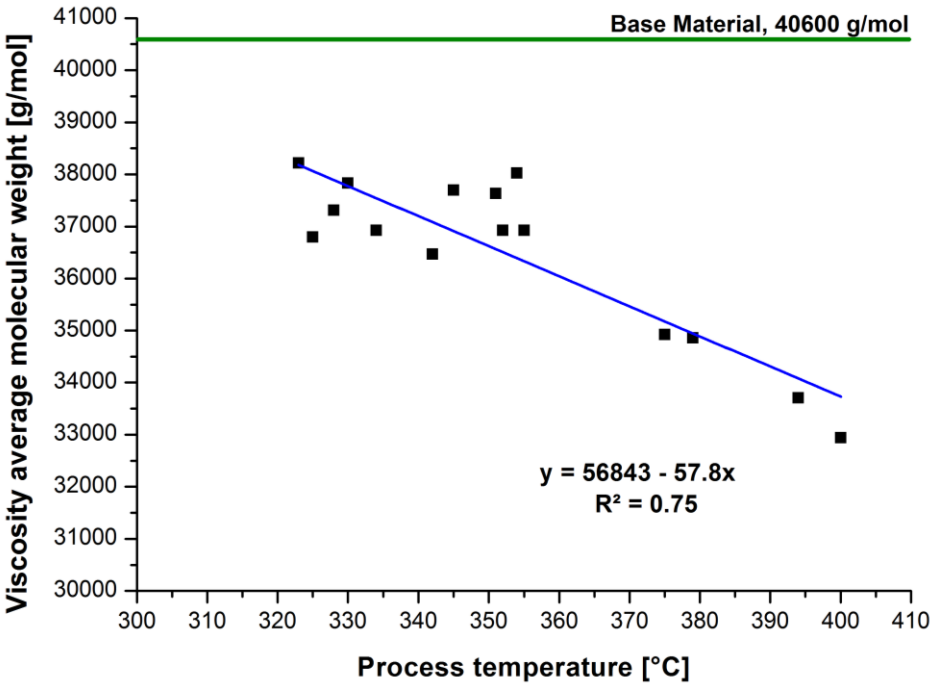

Figure 4.15 Correlation between PA6 viscosity average molecular weight and process temperature for the BBD conditions.

Complementary analysis using the ATR/FT-IR technique was performed on the flash material expelled during FricRiveting of joints produced with different heat inputs: low C3 (process temperature = 323 ºC), medium C9 (process temperature = 342 ºC) and high C13 (process temperature = 399 ºC) heat inputs. This technique was used to try to corroborate with the degradation pointed out by viscosity measurements. Figure 4.16 shows the characteristic absorption bands for the samples of the three conditions and base material in the range of 1900-1200 cm^{-1}. This range was selected because two strong IR absorption bands at about 1645 cm^{-1} (amide I) and 1545 cm^{-1} (amide II) can be observed within this range. Other bands are observed within the 1200 -1500 cm^{-1} region of the IR : 1417 cm^{-1} and 1477 cm^{-1} (CH_2 scissors vibrational mode), 1374 cm^{-1} (amide III and CH_2 wagging vibration), 1264 cm^{-1} (N-H bending and C-N stretching) and 1305 cm^{-1} (CH_2 wagging) [42].

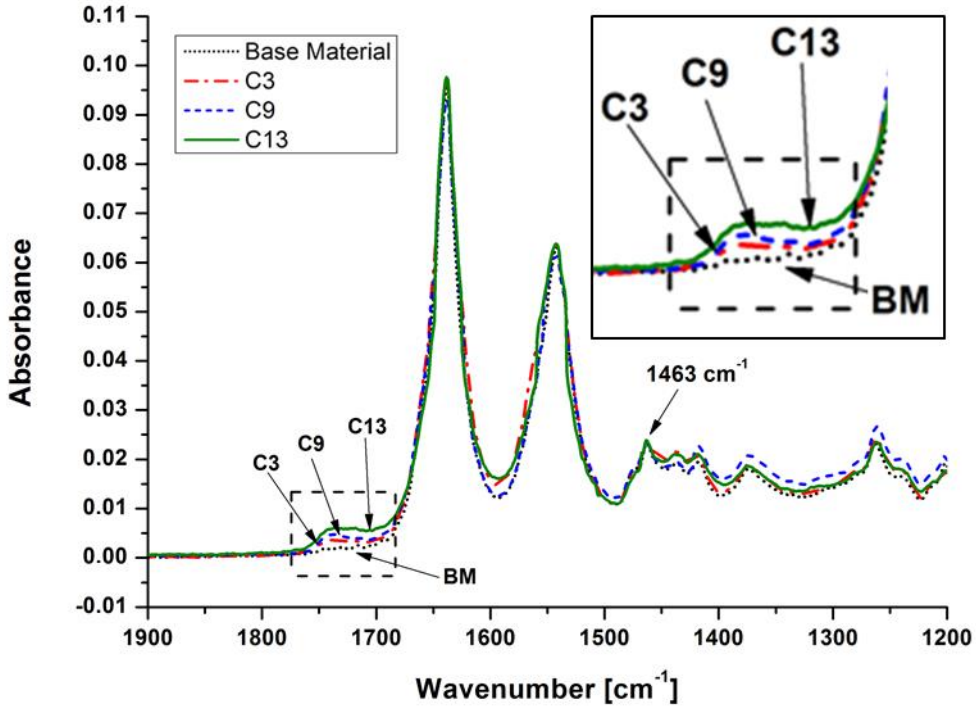

Figure 4.16 IR spectra of polyamide 6 composite samples in the range of 1900 -1200 cm^{-1} showing the growth in carbonyl region (marked with dashed rectangle). Note the unchanged polyamide 6 reference band at 1463 cm^{-1}.

As it can be seen from spectra of Figure 4.16, a new band is observed between 1710 cm^{-1} and 1760 cm^{-1} for the joined samples in comparison with the base material. According to Dong and Gijsman [42] and reported in Section 2.1.2, the thermo-oxidative degradation of PA6 produces carbonyl compounds such as aldehydes and ketones (Figure 2.4-a). The new absorption band between 1710 cm^{-1} and 1760 cm^{-1} is a combination of ketones at ~ 1715 cm^{-1}, aldehydes at ~ 1725 cm^{-1} , esters at ~ 1735 cm^{-1} and aliphatic carboxylic acids at ~ 1750 cm^{-1} as proposed by Dong and Gijsman [42].

Figure 4.17 shows the carbonyl index as a function of the process temperature for the joints produced with three selected conditions. The carbonyl index was determined as the ratio between the area of the carbonyl band (1710-1760 cm^{-1}) and the reference band (CH_2 scissors at 1458-1468 cm^{-1}). An example of the deconvolution procedure of IR spectrum is given in Appendix B. The band at 1463 cm^{-1} corresponding to the methylene scissoring and rocking modes was

used as a reference to compare the spectrums since this group is not sensitive to thermal-oxidation [42] in the temperature range achieved during FricRiveting.

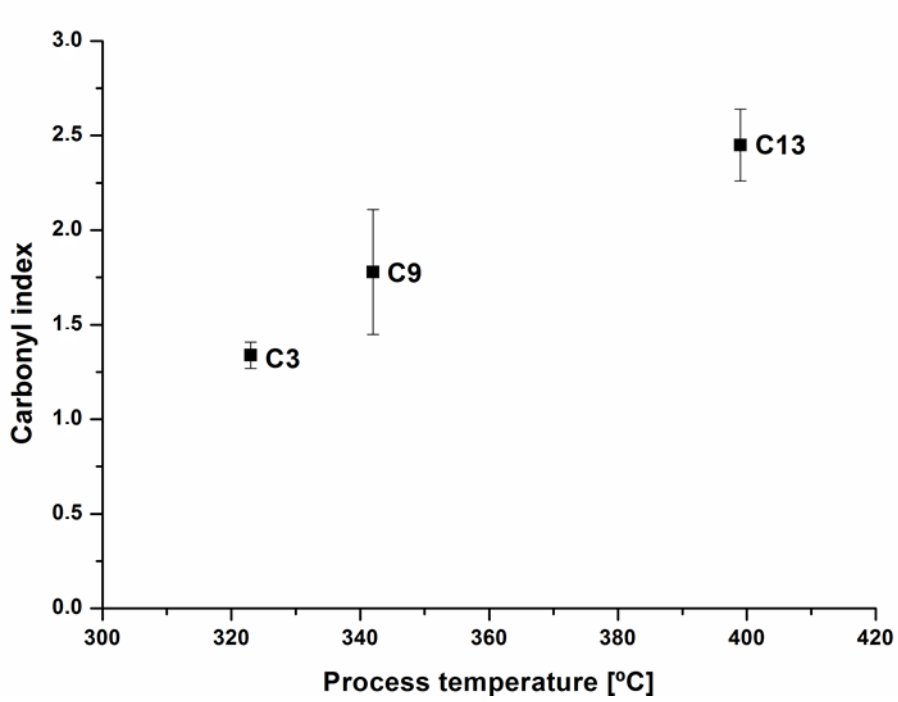

Figure 4.17 Correlation between PA6 carbonyl index and process temperature for samples taken from the flash material expelled during FricRiveting of joints produced with the selected conditions C3, C9 and C13.

It appears that the process temperature has a direct influence on the carbonyl index, whereby higher temperatures cause higher levels of thermo-oxidative degradation (represented by the increase the carbonyl index, Figure 4.17). Therefore the same trend observed in the viscosity analysis was thus verified by ATR/FT-IR. In FricRiveting, the process achieves high temperatures in an oxidative environment. In this way the degradation to a certain extent is unavoidable for the studied combination of materials and joining parameters range. Future studies of specimens with different water contents before joining could be helpful to elucidate the role of thermo-oxidative degradation in friction-rived polyamide specimens.

DSC measurements were carried-out with samples extracted from the CTMAZ of joints produced with different heat inputs, C3 (323 ºC), C9 (342 ºC) and C13 (399 ºC) to determine the melting enthalpy (ΔH_m), as well as the melting (T_m) and crystallization (T_c) temperatures. Table 4.2 displays the average degree

of crystallinity (X_c), melting (T_m) and crystallization (T_c) temperature of PA6 for these samples. The FricRiveting process as a whole did not affect significantly X_c, T_m and T_c values of PA6 in the composite as compared to the base material. This shows that the heat-cooling cycle (thermal history) imposed by FricRiveting does not lead to significant changes in the degree of crystallization of PA6 with respect to the base material. In FricRiveting, the CTMAZ of composite is submitted to high shear rates and process temperatures, which resulted in different levels of PA6 chain scission for each BBD joining condition, depending on the heat input, as shown earlier. However, this does not result in any significant change in the degree of crystallization of PA6, as well as in T_c. Besides, the high level of PA6 chain orientation in the CTMAZ imposed by the rotating tool does not appear to influence the recrystallization of PA6.

Table 4.2 Degree of crystallinity, melting and crystallization temperature of PA6 samples taken from CTMAZ of joints produced with conditions C3, C9, C13 and base material.

Sample	Degree of crystallinity [%]	Melting temperature [°C]	Crystallization temperature [°C]
Base material	26.6 ± 0.7	214.6 ± 0.4	184.4 ± 0.1
C3	27.4 ± 1.4	215.4 ± 0.7	184.1 ± 0.4
C9	27.8 ± 0.3	215.0 ± 0.5	184.4 ± 0.3
C13	27.8 ± 0.4	215.2 ± 0.1	184.4 ± 0.2

4.2.2.3 Polymer Composite Integrity

The effect of the joining process on the average glass fiber length was measured for the three selected conditions with different heat inputs, C3 (323 ºC), C9 (342 ºC) and C13 (399 ºC) and compared with the PA6-30GF base material. Samples were extracted from the flash material expelled and collected during the process. Although the samples used may not correspond directly to the material at the CTMAZ in the joints, it is reasonable to assume that they provide a good estimate of the process-related breakage of the fibers, as the expelled material has been direct sheared and heated by the rotating rivet. Figure 4.18 shows the

LO micrographs with the separated glass fibers for the base material and the three selected conditions.

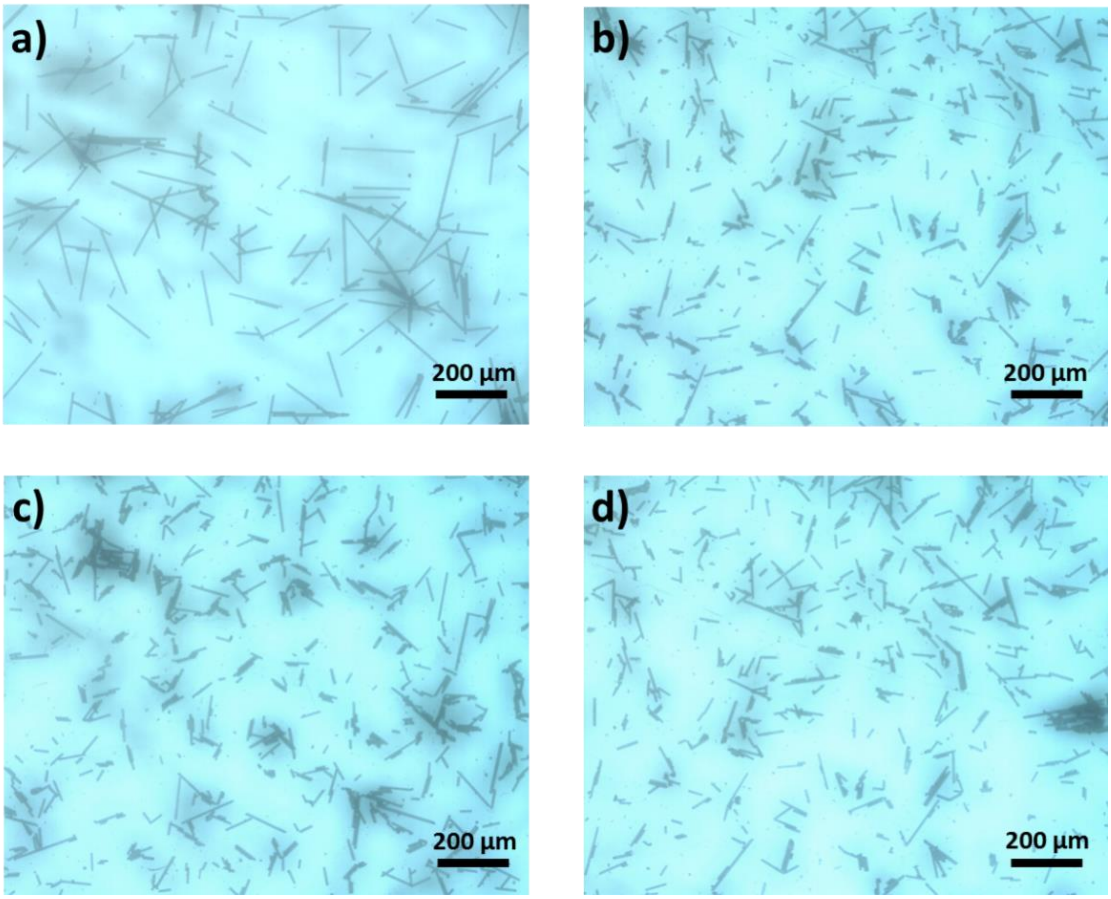

Figure 4.18 OM images of glass fibers recovered from: PA6-30GF base material (a); joints produced with condition C3 (b), condition C9 (c) and condition C13 (d).

The glass fiber length distributions in the PA6-GF after the process are shown as histograms in Figure 4.19. The values for the average glass fiber lengths l_n and l_w and the polydispersity index P are enclosed in the histograms.

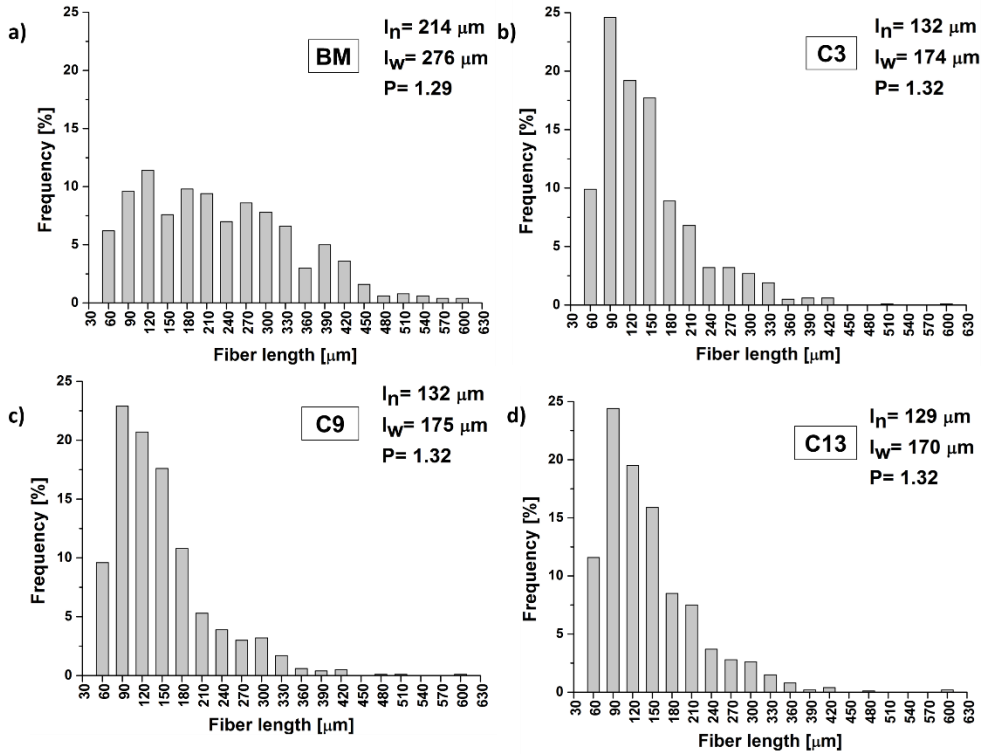

Figure 4.19 Histograms of the glass fiber lengths in the PA6-GF composite for samples taken from: PA6-30GF base material (BM) (a) and joints produced with: condition C3 (b), condition C9 (c) and condition C13 (d).

For all FricRiveting conditions analyzed, similar fiber length distribution patterns were observed. However, a considerable decrease in the average fiber lengths (l_n and l_w) was detected as compared to the PA6-30GF base material. The weight-average fiber length (l_w) measured in the expelled flash of joints produced in the conditions C3 (l_w = 174 μm), C9 (l_w = 175 μm) and C11 (l_w = 170 μm) are higher but very close to the critical fiber length for effective reinforcement, which is 167 μm according to the estimation using the Kelly-Tyson model [83]. This model is applied to polymer composites where fibers are aligned in the direction of the uniaxial tensile loading, which differs from the real fiber distribution in a standard friction-riveted metallic-insert composite joint. Additionally, in the T-pull testing, the load distribution is more complex than a uniaxial tensile testing. However, when using the Kelly-Tyson model, it is assumed that several fibers present in CTMAZ may be aligned to a uniaxial tensile loading; therefore one may assume that they are effective as reinforcement. The high breakage of the glass fibers and the similar average sizes and distribution for the investigated joining

conditions occur mainly because the FricRiveting process starts in the solid state. Thus, at the beginning of the process, the glass fibers are not covered by the molten PA6 and this leads to the breakage of the fibers independently from the preset parameters. In the manufacturing of PA6-30GF sheets two steps are undertaken in order to control the breakage of the glass fibers. Firstly, the extruder is filled with PA6 pellets and secondly, after the PA6 is already molten, the extruder is filled with the glass fibers in the form of chopped roving of about 5 mm length [108]. Following these steps, the glass fibers are dispersed and covered by the polymer matrix, while the combination of the extruder parameters determines the final fiber length. In FricRiveting, glass fiber breakage seems to be unavoidable and this might not be influenced by the process parameters. Nevertheless, due to larger volume CHAZ in comparison to the very thin CTMAZ (i.e. the consolidated composite layer around the rivet), it will be the polymer composite portion in the volume of interaction that most supports the load during the T-pull testing. This will be further discussed in the following sections.

4.3 Quasi-Static Mechanical Performance of Friction-Riveted Joints

The mechanical strength of the AA6056-T6/PA6-30GF joints was evaluated by T-pull tensile tests as described in Section 3.4.8. The joint strength was evaluated through the maximum value of the force (ultimate tensile force, UTF) recorded in the force-displacement curves. The elongation of the friction-riveted joints cannot be interpreted like the elongation of a standardized specimen for tensile tests because it is usually influenced by the insertion of the rivet. Thus, the analysis of elongation is not addressed in this study.

Figure 4.20 shows the ultimate tensile force achieved for the AA6056-T6/PA6-30GF joints produced with BBD conditions along with the strength of the rivet. Joints produced under the described conditions achieved between 35 % (1862 N) and 92 % (4937 N) of the ultimate tensile force of the rivet (5320 ± 102 N). The force-displacement curves for all the joining conditions are summarized in Appendix C.

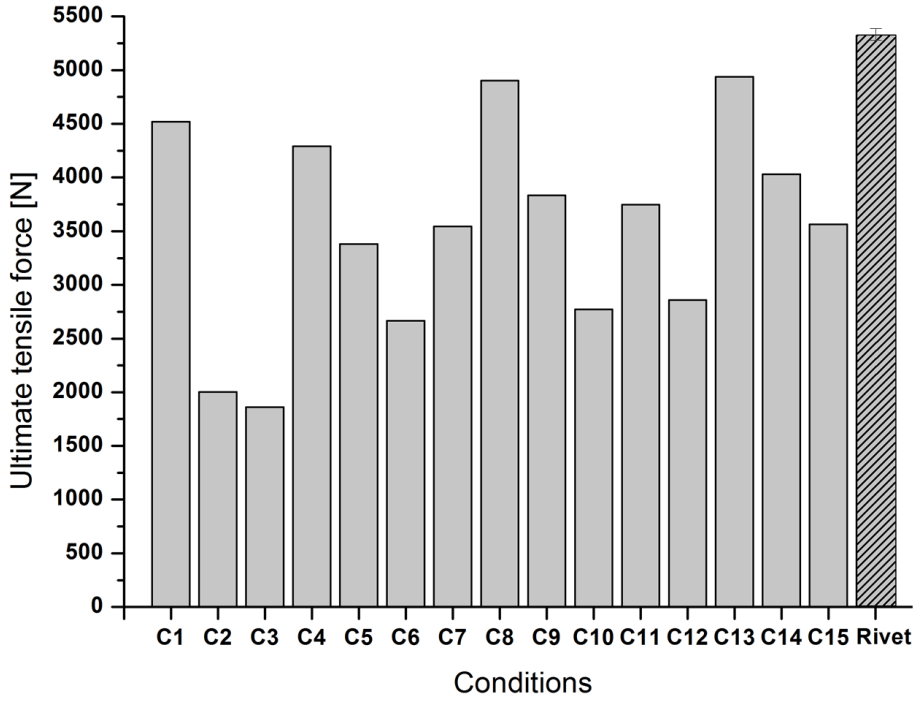

Figure 4.20 Ultimate tensile force for the joints produced with the BBD conditions and the base material.

In Figure 4.21, UTF, VR and Process temperature are shown to summarize the results and support the analysis of the correlation of the responses.

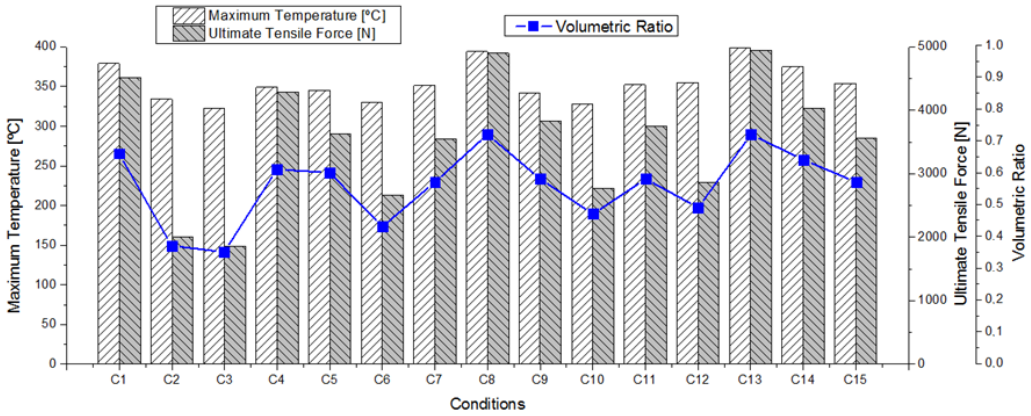

Figure 4.21 Maximum temperature, ultimate tensile force and volumetric ratio for the 15 BBD conditions.

One can observe in Figure 4.2 that process conditions leading to low temperatures generated joints with lower anchoring efficiency and consequently lower mechanical strength. The joint produced with condition C13 achieved 399 °C and 4937 N, while the one produced with condition C3 achieved 323 °C and

1862 N, a temperature lower by 19 %, leading to a decrease of 62 % in UTF. The joint mechanical strength seems to be mostly influenced by the geometry of the anchoring zone, with little or no effect of the level of PA6 degradation (Figure 4.16) and GF breakage (Figure 4.19) observed in the CTMAZ. For instance, despite of condition C13 (a high heat input condition) has resulted in the largest decrease of viscosity average molecular weight of PA6 and similar level of fiber breakage, it led to the strongest joint. Therefore the increase in anchoring performance in this study represented by the volumetric ratio appears to be the main mechanism influencing joint quasi-static tensile strength. This might occur because the CTMAZ volume is smaller than the CHAZ in the Volumetric Ratio thus CHAZ that most supports the load during the T-pull testing (Figure 4.3). Although this general behavior should be further confirmed by simulation and detailed experimental analysis. Considering this, the level of degradation seems to be less relevant to joint mechanical performance within the parameters range selected in this study.

The mechanical performance of friction-riveted joints is directly influenced by the features of the anchoring zone (depth and deformation of the metallic rivet) and the polymer stiffness, since it transfers the load from the rivet to the polymeric matrix [10,11,66]. The volumetric ratio was introduced to quantify the influence of the anchoring zone on the mechanical performance of friction riveted joints. The joints were scanned with X-rays before mechanical testing, as described in Section 3.4.3. With the obtained measurements of the rivet anchoring, the correlation between volumetric ratio and ultimate tensile force can be described. The graph of Figure 4.22 shows the correlation between the ultimate tensile force with the respective volumetric ratio for AA6056-T6/PA6-30GF joints. The green horizontal dotted line represents the average ultimate tensile force of the metallic rivet and the blue dashed line represents the limit at which a fracture through the rivet started occurring for the investigated joints.

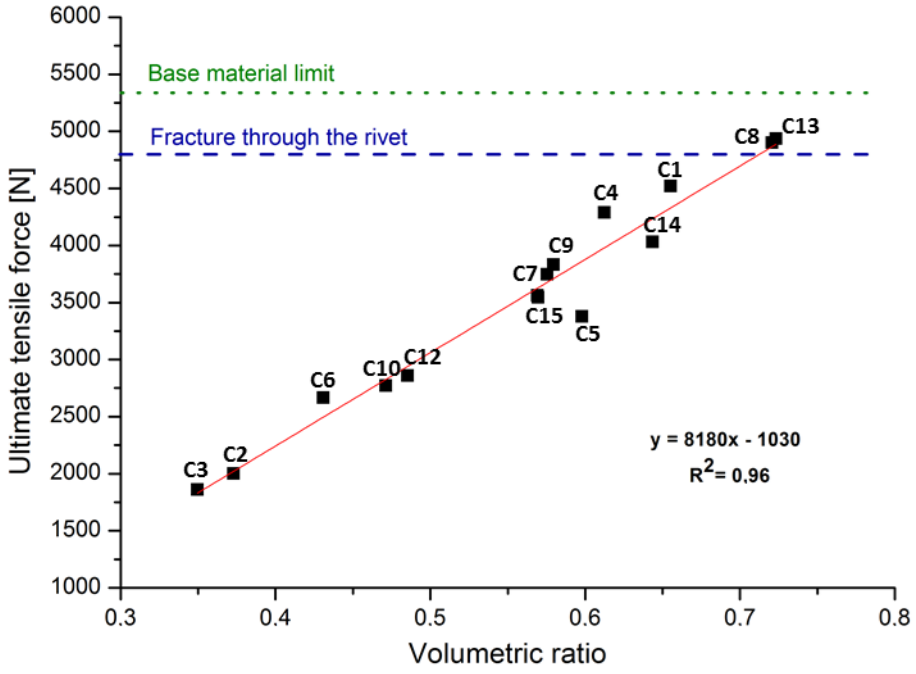

Figure 4.22 Correlation between ultimate tensile force and volumetric ratio for AA6056-T6/PA6-30GF joints.

As shown in Figure 4.22, the correlation between UTF and VR is linear, following the Equation 1. The reliability of the model was evaluated through the value of the regression coefficient (R^2). In this case, R^2 is equal to 0.96, which indicates a good model agreement with the experimental data. Moreover, it is noted that high volumetric ratio values resulted in joints with high mechanical strength, following the trend reported in the literature [10,11,15]. It has been shown in this work that X-ray radiography in combination with volumetric ratio has a good potential to be used to non-destructively evaluate the quality of the friction-riveted joints and estimate quasi-static tensile strength in future industrial applications.

4.4 Fracture Analysis

Friction-riveted AA6056-T6/PA6-30GF joints underwent two failure modes in T-pull testing. As shown in Figure 4.22, two joints (C8 and C13) had a ductile fracture that occurred in the metallic rivet outside of the polymer composite plate (fracture Type I) (see detailed analysis in Figure 4.23-a,b). All the other joints (C1-

C7; C9-C12; C14-C15) failed by full rivet pullout (fracture Type III) from the composite plate (Figure 4.23-c,d). The joints which fractured in the metallic rivet are the stronger joints and they presented ultimate tensile force up to 92% of the metallic rivet. This small loss in mechanical strength occurs due to annealing phenomena, as described in Section 4.2.1, which decrease the global and local mechanical properties of the metallic rivet.

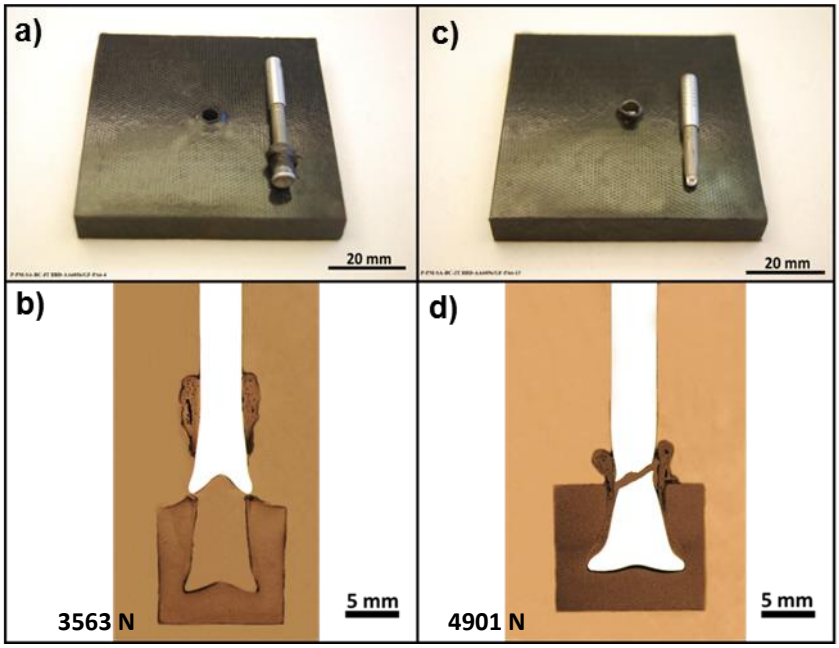

Figure 4.23 Joint failure modes: a) and b) full rivet pullout, condition C15 (RS: 15000 rpm, DaF: 9 mm and JF: 1900 N) and c) and d) through the metallic rivet. Joint produced with condition C8 (RS: 15000 rpm, DaF: 10 mm and JF: 2200 N).

The micro-mechanisms of fracture were analyzed by SEM at the fracture surfaces of selected joints. Figure 4.24 shows the fracture surface of the polymer composite for a representative joint (C9) that had a high value of VR but failed by full rivet pullout (Type III) from the composite plate.

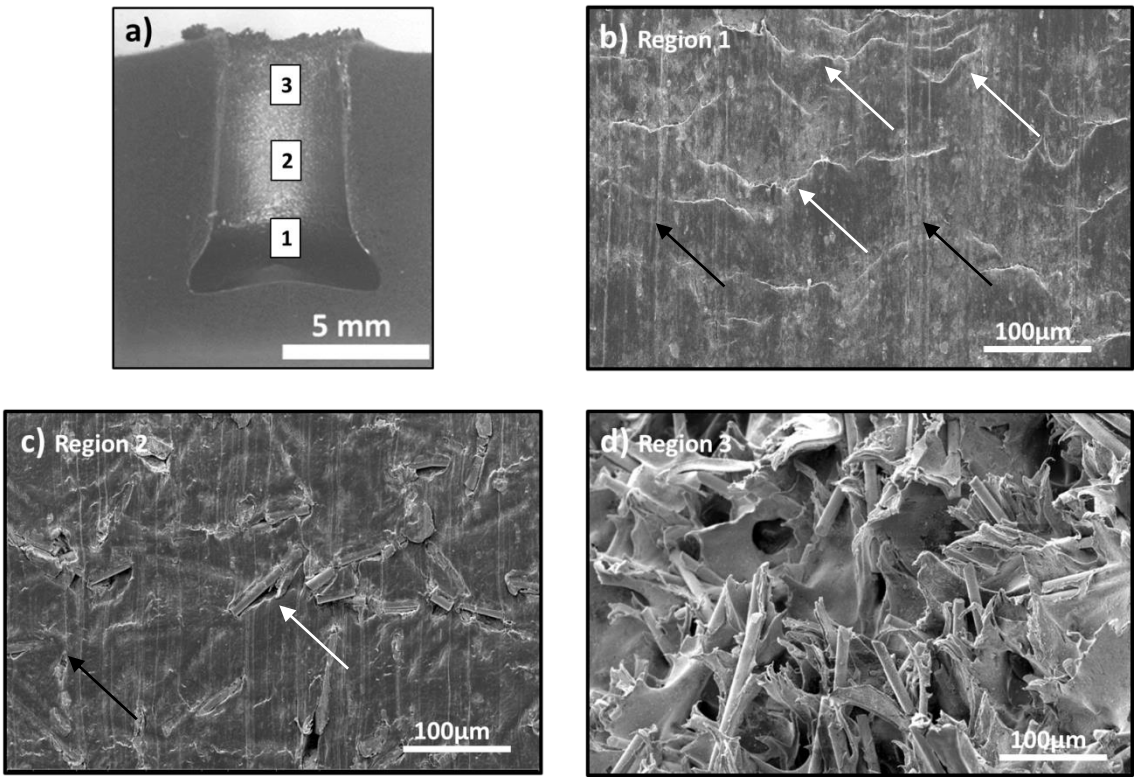

Figure 4.24 SEM images of fracture surfaces of the PA6-30GF part from which the rivet has been fully pulled out from the polymer composite plate. Joint produced with condition C9 (RS: 15000 rpm, DaF: 9 mm and JF: 1900 N).

In Figure 4.24 some deformations aspects of PA6-30GF are observed. The deformation of the composite (white arrows) and the vertical marks (black arrows) are observed in Figure 4.24-b. In Figure 4.24-c, exposed glass fibers (white arrows) and the vertical marks (black arrows) can be visualized. In Figure 4.24-d, the deformation aspects indicate that a ductile fracture of the composite took place. These features were caused by the interaction with the pulled rivet during T-pull tensile testing. This interaction appears to increase from Region 1 to Region 3, because the diameter of the tip of the metallic rivet is wider than the diameter of the rivet keyhole in the composite. Thus, the composite is less deformed in Region 1, where the keyhole is slightly wider, than in Region 2. In Region 2, the plastic deformation by the rivet pull action is more severe, leading to a greater damaging of the polymer composite and consequently to glass fiber exposure. The bigger deformation that lead to fracture occurred in Region 3, the same area where the joint has a high concentration of voids at the CTMAZ/CHAZ

interface (compare with Figure 4.8). Probably, during the rivet pull-out action, the polymer composite at this volume did not support the load and the crack propagates through the CTMAZ/CHAZ interface, as the defects may act like notches.

In Figure 4.25, the fracture surface of the metallic rivet and the polymer composite part attached to it for a joint that failed by full rivet pullout (Type III) is shown.

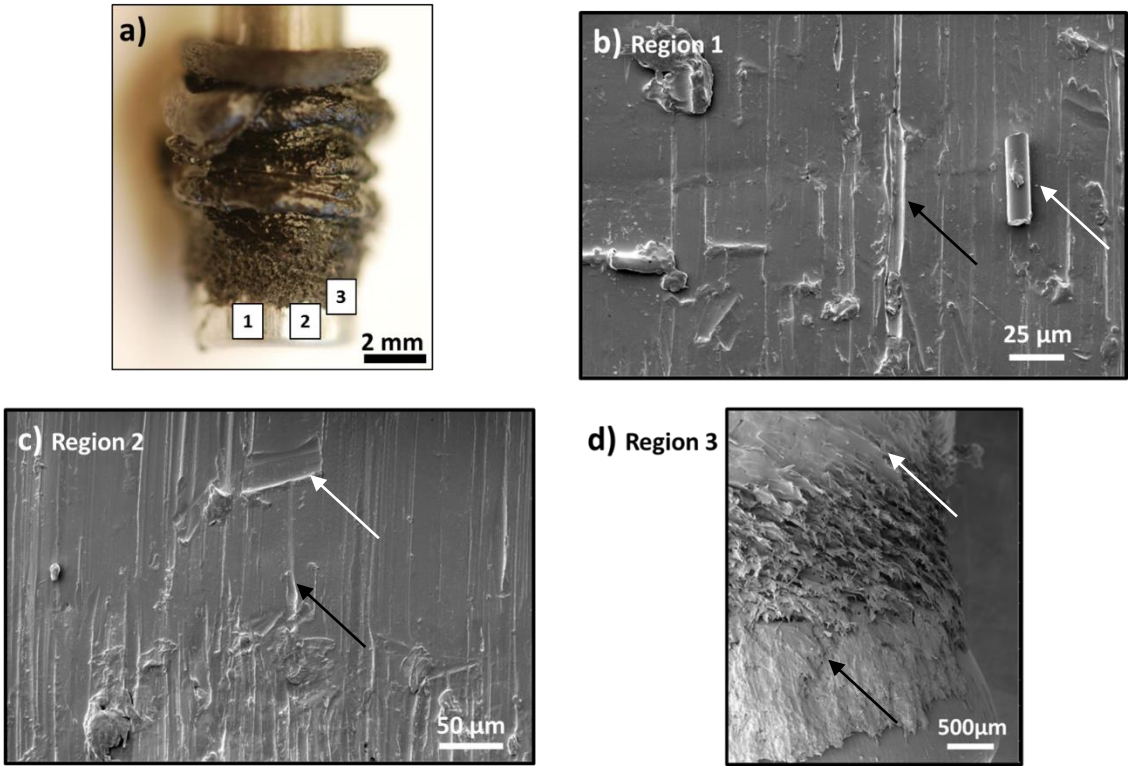

Figure 4.25 SEM images of fracture surfaces of the AA6056 rivet being fully pulled out from the polymer composite plate. Joint produced with condition C9 (RS: 15000 rpm, DaF: 9 mm and JF: 1900 N).

The rivet surface and the polymer composite part attached to it are observed in Figure 4.25. Vertical marks (black arrow) and glass fibers (white arrow) are observed in Figure 4.25-b. In Figure 4.25-c, the vertical marks (black arrow) are present whereby an impression left by a glass fiber can be seen (white arrow). These vertical marks in the aluminum rivet were produced by the exposed glass fibers which were identified in Figure 4.24-b. The polymer composite part that is attached to the metallic rivet is observed in Figure 4.25-d. This polymeric part is composed by two different regions, the flash material (white arrow) and a

small part of the CTMAZ (black arrow). This CTMAZ part might have fractured at the interface with the CHAZ due to the high concentration of defects already described in Section 4.2.2.1.

The joints produced with conditions C8 and C13 fractured through the metallic rivet outside the polymer composite plate (Type I fracture, Figure 2.13); this is the best fracture in terms of ultimate tensile force reported for the friction riveted joints. Figure 4.26 shows the ductile fracture characterized by the cup-and-cone shape of the fracture surface typically observed for T-Pull tensile specimens failing through Type 1 fracture [10,12,69].

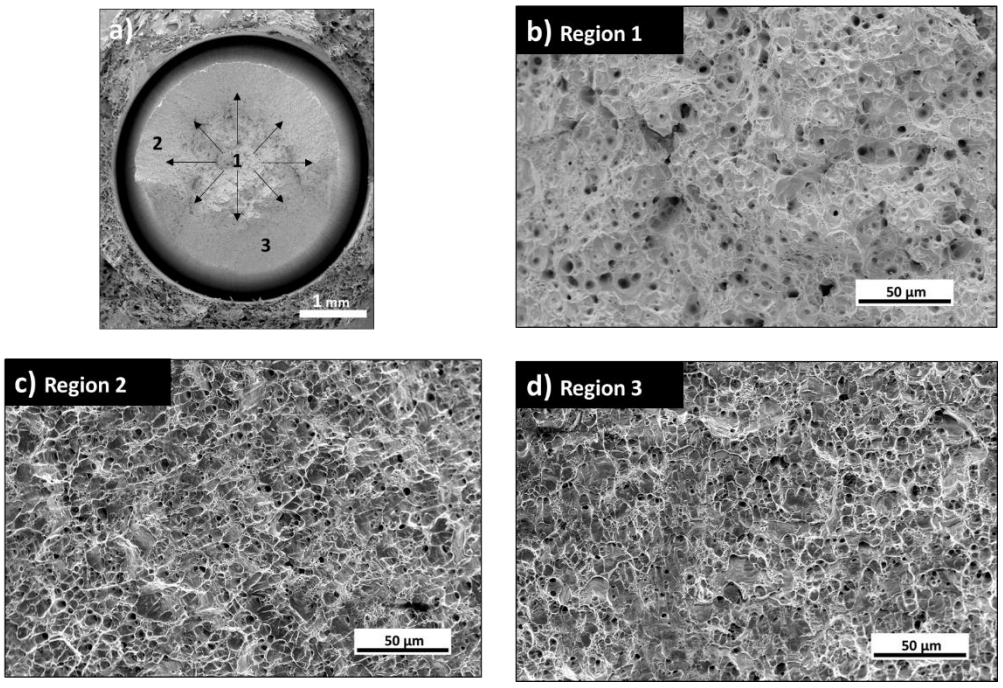

Figure 4.26 SEM images of fracture surfaces of the AA6056 rivet with the fracture occurring through the metallic, rivet outside the polymer composite plate. Joint produced with condition C13 (RS: 16000 rpm, DaF: 9 mm and JF: 2200 N).

The central geometry of the fibrous zone of a cup-and-cone fracture can be observed in Figure 4.26-b. These fibrous zones are related to the presence of spherical dimples; dimples are microvoids which grow under local tensile loads to coalesce with adjacent dimples and eventually nucleate a crack [109]. Figure 4.26 –c and Figure 4.26-d present a smooth shear surface related to the geometry transition from the spherical to elliptical dimples. These regions are commonly named shear lips [109]. The fracture started in the emphasized region in Figure

4.26-b (Region 1) due to uniaxial tension and propagated at 45 degrees, where the shear stress is maximum, until the region emphasized in Figure 4.26-c (Region 2) and Figure 4.26-d (Region 3) [97].

For the first time in literature, it is hereby reported that a part of the CTMAZ is pulled out with the metallic rivet during T-pull tensile testing for a failure Type III in FricRiveting (Figure 2.13). This occurred because of the high concentration of voids at the CTMAZ/CHAZ interface, leading to preferential crack propagation in this region. Nonetheless, this notch effect has occurred only with joints that had a volumetric ratio lower than 0.72, since the CTMAZ might be composing a large volume of the VR's volume of interaction (see Section 3.3.4). Joints with a VR equal or greater than 0.72 suffered a ductile failure in the metallic rivet, as shown in Figure 4.26. This might be occurring due to a reduced CTMAZ volume compared to the total volume of composite material (i.e. the volume of interaction) resisting the pull-out of the rivet. A more detailed analysis of the micro-mechanisms is required to better understand these phenomena. However, this is out of the scope of this work.

4.5 Effect of Process Parameters on Joint Properties

The previous sections elucidated the main microstructural properties and mechanical strength of friction-riveted AA6056-T6/PA6-30GF joints. This section analyzes the effects of joining process parameters on the process temperature, ultimate tensile force of joints and viscosity average molecular weight of PA6 by means of statistical analysis. These analyses are based on the Box Behken Design of experiments (Section 3.4.10, Table 3.4). In order to study the influence of parameters and their interactions on the selected responses, analysis of variance (ANOVA) was performed with 90 % and 95% confidence level (strongly significant when $p<0.05$ and marginally significant when $0.05<p<0.1$), in combination Response Surface Analysis.

4.5.1 Effect of the Process Parameters on the Process Temperature

The temperature achieved in FricRiveting is closely related to the heat input during the frictional phase. The temperatures were measured on the expelled flash material following the procedure described in Section 3.4.2. For the BBD conditions the maximum temperatures measured ranged between 323 and 399°C (as presented in Figure 4.2). The advantage of response surface methodology in comparison to others designs of experiments, such as two-level full factorial, is that it can account for nonlinear behaviour. Furthermore, two and three dimensional graphs are generated, respectively, a contour plot and a response surface. With these plots it is possible to obtain an optimal process parameter window [110]. In Figure 4.27a,c,e, surface graphs are presented to analyze the interaction of the Rotational Speed and Joining Force at constant levels of Displacement at Friction (8, 9 and 10 mm) and their influence on the maximum process temperature. The contour plots in Figure 4.27b,d,f represent the projection (i.e. a top view) of the mentioned surface graphs at the respective values of the Displacement at Friction, helping to identify the regions of interest/optimal parameter windows.

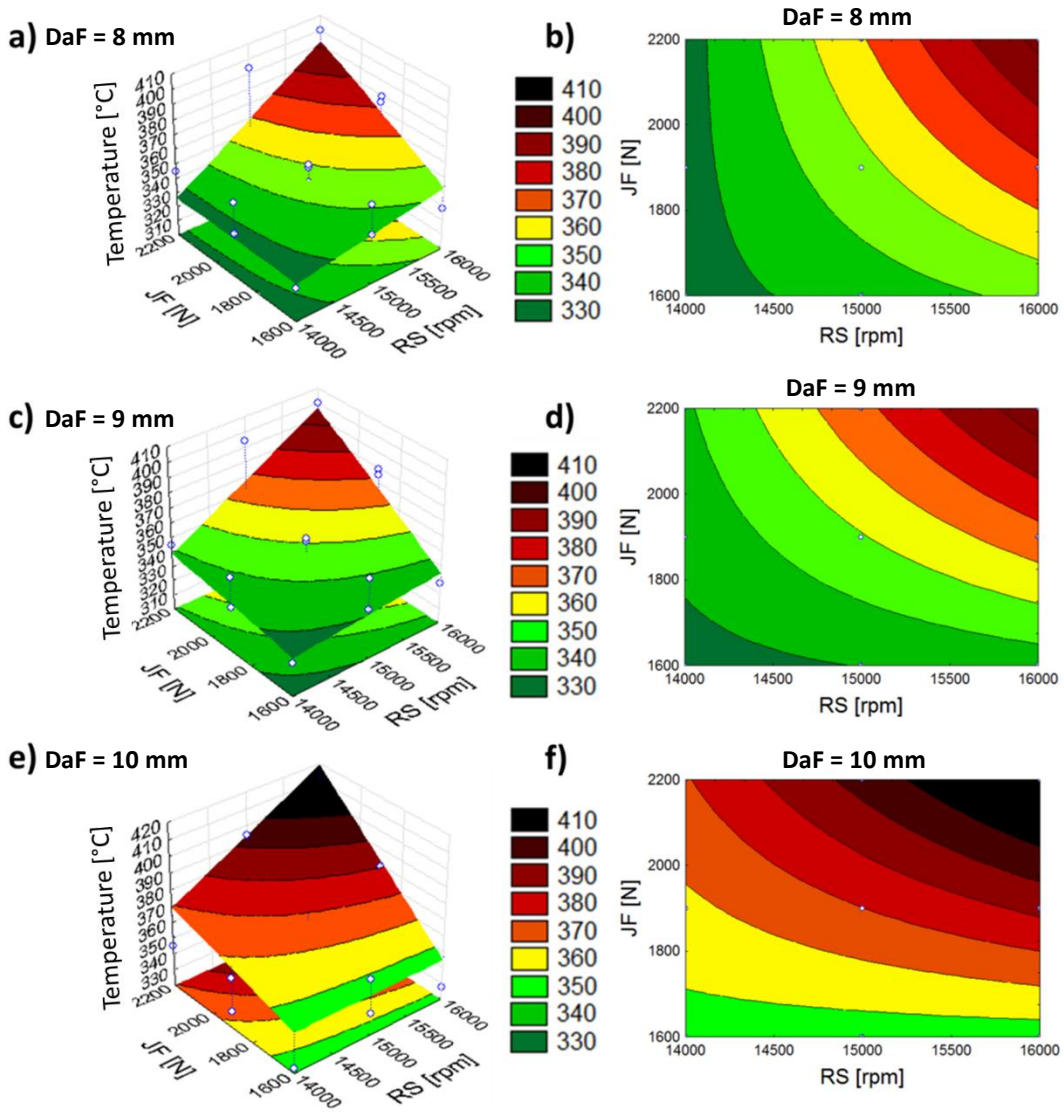

Figure 4.27 Surface graph for the maximum temperature achieved in the FricRiveting process at constant Displacement at Friction equal to (a) 8 mm, (c) 9 mm and (e) 10 mm. The respective contour plots for the maximum process temperatures when keeping Displacement at Friction constant at 8 mm (b), 9 mm (d) and 10 mm (f).

From the data of Figure 4.27, it can be observed that the higher Rotational Speed and Joining Force the higher maximum process temperature will be during the FricRiveting process. It is also possible to observe that when the Displacement at Friction is increased (Figure 4.27-a to e and Figure 4.27-b to f), the maximum temperature is higher. The difference between the temperatures in Figure 4.27-a and Figure 4.27-e is clear; an increase of 2 mm on the Displacement at Friction increases the maximum process temperature and the

joining parameter range (i.e. a bigger area of process peak temperatures of 370-410 ^{o}C will be formed at DaF=10 mm). When analyzing the surface plots, it is possible to say that the influences of Rotational Speed and Joining Force on the maximum temperature changes at different Displacements at Friction. From the shape of contour plot in Figure 4.27-b, the maximum temperature is more sensitive for RS when DaF is 8 mm. The JF behavior is exactly the opposite; JF had a higher influence when DaF is 10 mm (Figure 4.27-f). This might be related to the rivet feeding rate. When JF is increased, the spindle velocity (feeding rate) is also increased shortening the frictional phase. In other words, for a DaF kept constant at 8 mm, an increase in JF might not be sufficient to increase the temperature because the shorter frictional phase means less heating. But for a DaF of 10 mm, a higher JF appears to be sufficient to increase the temperature (Figure 4.27-f); despite of a shorter frictional phase, the heat development will be sufficient to achieve a higher temperature as the way to be covered by the plunging rivet is longer. This means that there should be a balance between the time and the force used during the frictional phase; sometimes an increase in the frictional force will not lead to a higher temperature because the extension of the frictional phase will be shorter (shorter frictional times) will not be long enough to generate an appropriate amount of heat.

Nevertheless, the RSM analyses does not allow for the significance of each parameter and their interactions in a certain response (e.g. process temperature), as it cannot be determined from the surface and contour plots. A better way to accomplish this understanding it through the evaluation through the p-value test. The value selected for the significance level was 5 % (α=0.05). In other words, the parameters and interactions that had a p-value smaller than 0.05 can be considered statistically significant for the maximum temperature achieved during the process [111]. The results of the analysis of variance (ANOVA) are shown in the Table 4.3.

Table 4.3 ANOVA table for the maximum temperature achieved in the process.

Factors	SS	df	MS	F	p-value
RS	2211.125	1	2211.125	53.49496	0.018185
DaF	1035.125	1	1035.125	25.04335	0.037688
JF	2738.000	1	2738.000	66.24194	0.014763
RS^2	0.160	1	0.160	0.00388	0.956013
DaF^2	313.083	1	313.083	7.57460	0.110554
JF^2	1.083	1	1.083	0.02621	0.886266
RS*DaF	72.250	1	72.250	1.74798	0.317080
RS*JF	625.000	1	625.000	15.12097	0.060221
DaF*JF	144.000	1	144.000	3.48387	0.202947
Residual error	513,917	5	102.78		
Lack of Fit	431.250	3	143.750	3.47782	0.231304
Pure error	82.667	2	41.333		
Total SS	7658.933	14			

From the Table 4.3, the strong significant individual parameters are the RS, DaF, JF and the slight significant interaction is RS*JF. The individual and combined contributions of each factor to the process temperature are presented in Figure 4.28.

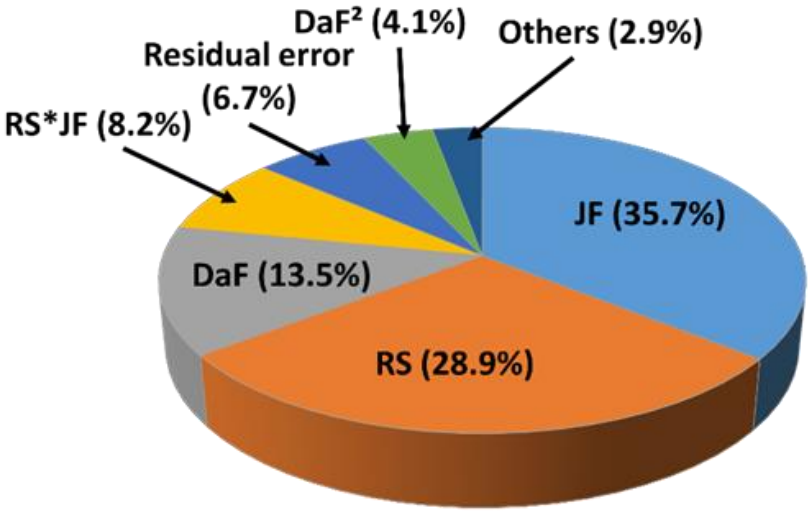

Figure 4.28 Percentage individual and combined contributions of the joining parameter on maximum process temperature.

In Figure 4.28, one can observed that the Joining Force (JF) was the parameter with the highest contribution to the temperature development, followed by the Rotational Speed (RS). This result could not be directly related with the heat input equation; in the heat input equation (Equation 9) the parameter that has the highest influence is the Rotational Speed (quadratic influence). The same trend of the current results were reported by Rodrigues *et al*. [112] using a full factorial design of experiments; the authors concluded that the variation, in percentage, is greater for the Joining Force in comparison to the Rotational Speed. For the production of the AA6056-T6/PA6-30GF joints, the variation in percentage for the Rotational Speed was 14.3 % and for the Joining Force was 37.5 %, therefore the current results did not follow the theoretical trend of heat input. The proposed heat input model by Amancio [95] is an analytical model assuming different simplifications related to materials properties, physical-chemical changes and boundary conditions (e.g. heat losses by conduction and convection are assumed to be absent). Therefore the actual temperature behavior may differ from the total heat input. Current efforts are in progress to use FEM to model heat development allowing for a more precise estimate of temperature.

Nonetheless, the results obtained are still reasonable, since both parameters are physically directly responsible for the heat generation and the difference between the influence of JF and RS on the maximum temperature is not extremely high (6.2 %). This can be better understood from the energy input model for friction-based process shown in Equation 10 [113], where both RS and JF and also DaF have the same contribution in the transformation of mechanical work into energy.

$$E = (M_{total} \cdot \omega \cdot \Delta t) + (F \cdot \Delta x) \ \ [J] \qquad (10)$$

Where: M_{total} is the Frictional torque, ω is the Angular Velocity, Δt is the Joining Time, F is the Axial Force and Δx is the Axial Displacement. As this simple equation shows a good correlation with the current experiments and corroborates with the findings of previous works of the group [12,114], it can be used as simple

and straightforward tool (i.e. it only requires set up data and frictional torque obtained from monitoring curves) to estimate heat generation.

The four statistically significant factors (RS, DaF, JF and RS*JF) contribute altogether with 86.3 % to the maximum temperature. The evaluated parameters have only one statically significant interaction, RS*JF interaction. Analyzing the RS*JF interaction in Figure 4.27, it can be observed that there is a real correlation between these joining parameters' interactions and the process temperature (the RS seems to influence more the process when JF is higher). The analysis of variance showed that this interaction has a slight statistical significance on the response ($0.10 = p > 0.060221$).

4.5.2 Effect of the Parameters on the viscosity average molecular weight of PA6

The molecular weight (MW) of the PA6 matrix of composite in the CTHAZ was evaluated by dilute solution measurements, as described in Section 3.4.6. As discussed earlier the process parameters influence directly the temperature and the shear rates of the process. The study of the influence of parameters on MW was carried out by analysis of variance (ANOVA), as presented in Table 4.4, in combination with the surface and contour plot analysis similar to Section 4.5.1. The surface and contour plots for the MW are given in Appendix D.

Table 4.4 ANOVA table for the viscosity average molecular weight of PA6.

Factors	SS	df	MS	F	p-value
RS	14299270	1	14299270	22.41246	0.041838
DaF	321659	1	321659	0.50416	0.551302
JF	14121770	1	14121770	22.13425	0.042331
RS^2	601391	1	601391	0.94261	0.434022
DaF^2	1123412	1	1123412	1.76082	0.315748
JF^2	866947	1	866947	1.35884	0.363953
RS*DaF	103615	1	103615	0.16240	0.725950
RS*JF	1807326	1	1807326	2.83278	0.234390
DaF*JF	2485854	1	2485854	3.89629	0.187102
Residual error	2465360	5	493072		
Lack of fit	1189349	3	396450	0.62139	0.664924
Pure error	1276011	2	638005		
Total SS	37859825	14			

The RS and JF had a p-value lower than 0.05, so they are statistically significant to the response MW. The contribution of each factor on the MW was calculated and the results are shown in the pie chart of Figure 4.29.

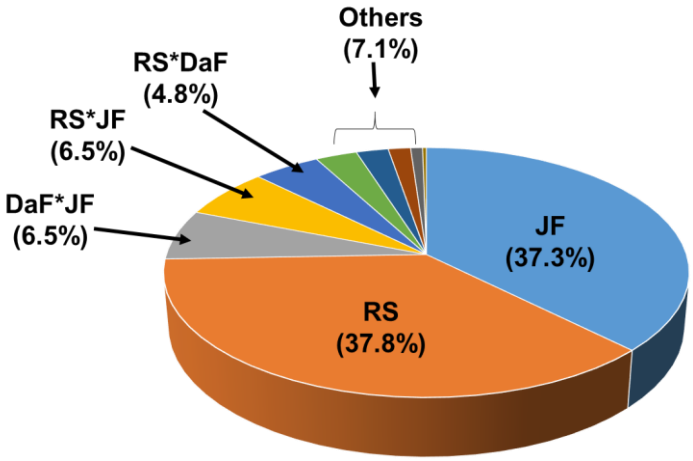

Figure 4.29 Percentage individual and combined contributions of the joining parameter on the viscosity average molecular weight of PA6.

From the data of Figure 4.29, it can be observed that the Rotational Speed and Joining Force were the factors with the largest effect on the values of MW. The influences of the RS and JF on the MW are similar in percentage contribution among then, respectively, 37.8 % and 37.3 %. The two statistically significant parameters contribute altogether with 75.1 % on the decrease of the MW. As described previously in Section 4.5.1, both parameters are physically responsible for the heat generation by friction. Consequently, an increase in these parameters might decrease the MW of PA6 (chain scission) because of higher process temperatures and higher shear rates. However, the level of PA6 degradation achieved in the CTMAZ seems not to have influence on the quasi-static mechanical strength of the joints (Section 4.3). This assumption must be checked since it is well known the mechanical strength of polymers decreases below a given MW value; nevertheless, critical values of viscosity average molecular weight for the PA6 were not found. Therefore no direct correlations could be made with the levels of decrease in MW induced by the process and possible losses in local and global mechanical properties of the joints.

4.5.3 Effect of the parameters on the ultimate tensile force (UTF) of joints

The quasi-static mechanical strength of the joints was evaluated by T-pull testing, as described in Section 3.4.8. The global mechanical performance of friction-riveted joints is influenced by the anchoring geometry of the deformed rivet, as already shown in Figure 4.22. The study of the influence of parameters on UTF was determined by ANOVA (Table **4.5**), in combination with the surface and contour plot analysis in the same manner as in Section 4.5.1. Appendix D presents the surface and contour for ultimate tensile force (UTF).

Table 4.5 ANOVA for the joint ultimate tensile force (UTF).

Factors	SS	df	MS	F	p-value
RS	2588950	1	2588950	212.2551	0.000028
DaF	1006071	1	1006071	82.4828	0.000271
JF	8544978	1	8544978	700.5602	0.000001
RS^2	51412	1	51412	4.2150	0.095273
DaF^2	32625	1	32625	2.6748	0.162877
JF^2	322959	1	322959	26.4778	0.003628
RS*DaF	38025	1	38025	3.1175	0.137719
RS*JF	38612	1	38612	3.1656	0.135331
DaF*JF	15500	1	15500	1.2708	0.310792
Residual error	60987	5	12197		
Lack of fit	22633	3	7544	0.3934	0.773925
Pure error	38354	2	19177		
Total SS	12706772	14			

The RS, DaF, JF and JF*JF had a p-value lower than 0.05, so they are statistically significant for the ultimate tensile force. The contribution of each parameter on the UTF was calculated and the results are shown in the pie chart of Figure 4.30.

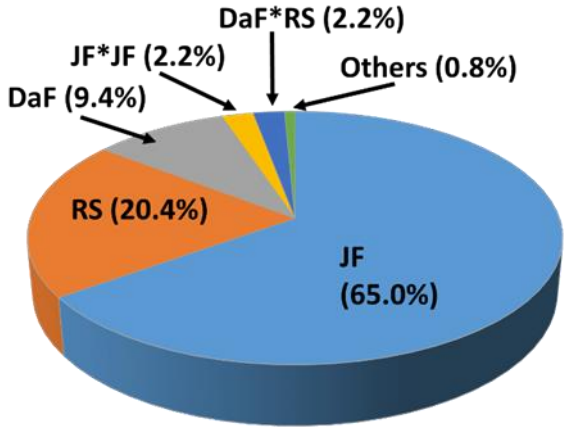

Figure 4.30 Percentage individual and combined contributions of the joining parameter on the ultimate tensile force (UTF) of joints.

The Joining Force was the factor with the highest individual effect on the values of UTF as shown in Figure 4.30. The four statistically significant parameters contribute altogether with 97.0% on the ultimate tensile force. Higher values of Joining Force increase the rivet deformation and consequently the joint strength as described in Section 2.2.4. This trend was reported by Rodrigues *et al.* [112] for Polycarbonate and Aluminum 2024 joints and by Altmeyer *et al.* [68] for short-carbon-fiber-reinforced polyether ether ketone and Titanium grade 3 joints. The second factor in importance is the Rotational Speed followed by the Displacement at Friction. The DaF cannot be directly related with the Friction Time but its influence on the geometry of the anchoring zone are similar [15,112]. This means that high values of FT or DaF lead to greater plastic deformations of the metallic rivet tip and, consequently, increasing the joint strength. The influence of the JF is three times higher than the RS and 6 times higher compared to the DaF on UTF. This might occur because the JF in this new force-controlled process variant with constant axial force (no typical higher forging forces applied) is directly related to the heat generation and also to the deformation of the tip of the metallic rivet. When the JF is increased the heat generation is also increased, as shown in Section 4.5.1; consequently, the deformation of the tip of the rivet is larger. The previous analysis of the two responses - Process Temperature and Molecular Weight– clarify that JF and RS are the main parameters influencing the process in terms of the two responses. They are controlling the heat generation and are directly influencing all the material transformations (rivet plastic deformation and polymer degradation) during the process.

4.6 Joint Optimization by Surface Design

The use of Box-Behnken Design allowed the optimization of the process using mathematical models along with the surfaces and contour plots as already mentioned in Section 4.5.1. The mathematical model describes the behavior of each response when the joining parameters are varied. The reliability of the models was evaluated using the adjusted coefficient of determination, R^2. After the validation with additional runs (i.e. joints produced within the range of joining parameters but with different conditions then the BBD standard runs), , these

models can be used to predict a specific response for a new combination of parameters that are within the range considered in this study [110,111].

Three statistical models (Equations 11-13) with a 90% confidence interval were built considering only the statistically relevant factors determined from ANOVA results (Table 4.3 - 6.5).

$$Temperature\ [°C] = 354 + 16.6 \cdot RS + 11.4 \cdot DaF + 18.50 \cdot JF \quad (11)$$

$$Viscosity\ Average\ Molecular\ Weight\ [g/mol] = 36373\ - 1337 \cdot RS - 1329 \cdot DaF \quad (12)$$

$$Ultimate\ Tensile\ Force\ [N] = 3715 + 569 \cdot RS + 354 \cdot DaF + 1033 \cdot JF - 147 \cdot JF^2 \quad (13)$$

Four random joining conditions within the studied parameter window were tested to validate these models. The conditions are shown in Table 6.6

Table 4.6 Validation conditions for AA6056-T6/PA6-30GF joints.

	Parameters		
Conditions	RS [rpm]	DaF [mm]	JF [N]
V1	14500	8.00	1700
V2	15750	8.50	2200
V3	14250	8.75	2100
V4	16000	8.25	2200

The experimental data compared to the predicted data for the reduced model equation are shown in Figure 4.31 – 33 for each response. Square symbols indicate runs from the BBD, and triangles symbols indicate validation runs (parameters within the BBD range but not identical). The identity line shows a virtual correlation of 1:1 between predicted and actual values, the dashed lines parallel to the identity line show the 10% uncertainty limits, and the dash-dotted lines are the prediction intervals for the model (limits in which the model is able to predict a single observation).

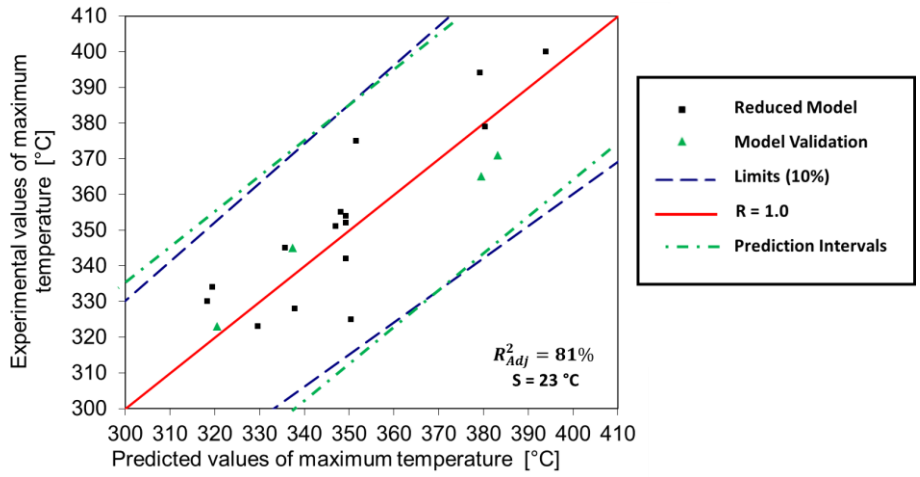

Figure 4.31 Validation of the reduced model for the maximum temperature achieved in the process.

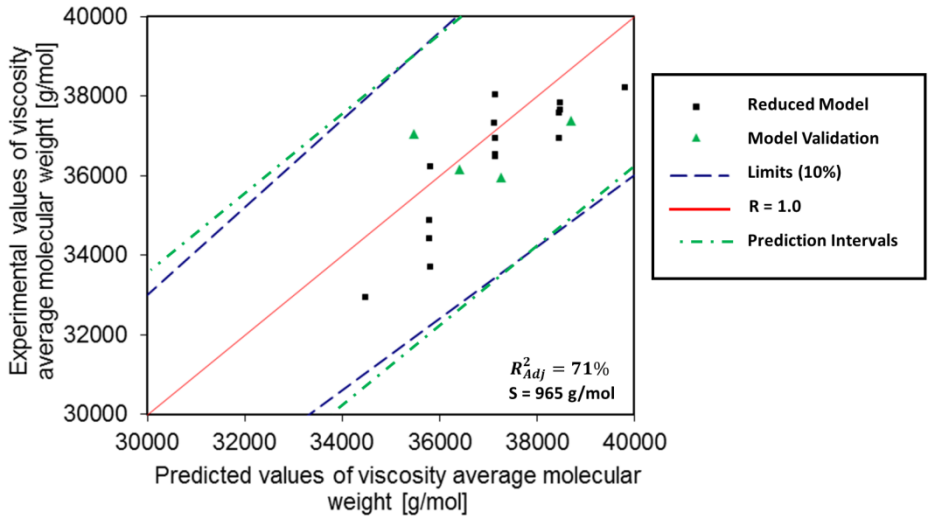

Figure 4.32 Validation of the reduced model for viscosity average molecular weight.

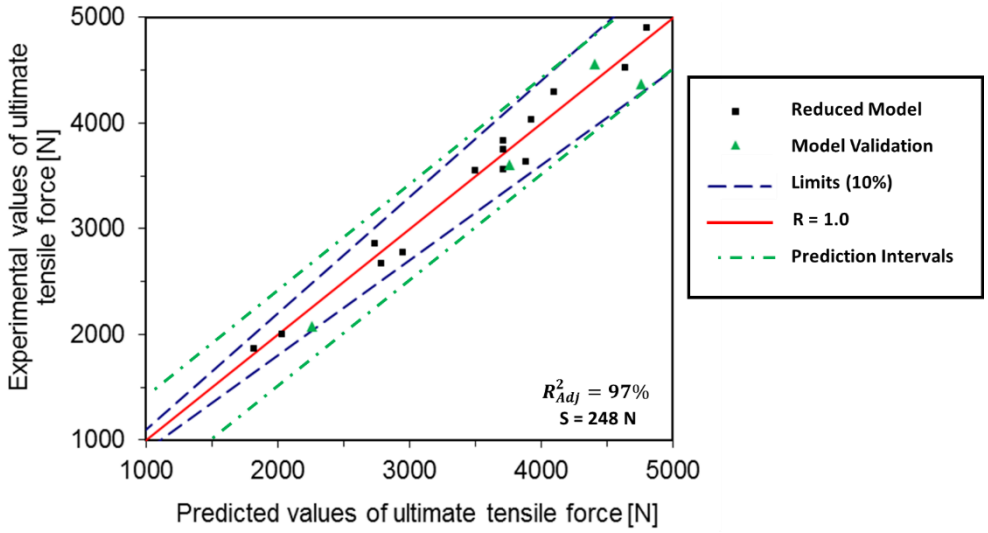

Figure 4.33 Validation of the reduced model for ultimate tensile force.

The models resulted in R^2_{Adj} values laying within 0.71 and 0.97, which proves that a good fitting of the experimental values was accomplished. The standard errors of the regressions are small. In Figure 4.31- 33, it is to be noted that all the validations were within the set 10 % variation limit. The 10 % limits are commonly applied in polymer welding/joining area, as a way to account for the variation in properties between different polymer grades and batches [12,46,112,115]. The slightly lower predictability of the Process Temperature (R^2_{Adj}=0.72) and Viscosity Average Molecular Weight (R^2_{Adj}=0.71) models can be accounted for the intrinsic experiments variance. For the Process Temperature measurement, the IR-Camera is very sensitive to any variation in ambient light or components colours, for instance. For the Viscosity Average Molecular Weight, the major variance might occur during the dissolution of PA6-30GF and its subsequent filtering. Nevertheless, the regression models still display a good predictability of the values of Process Temperature, Viscosity Average Molecular Weight of PA6 and Ultimate Tensile Force of the joints.

The selection of the optimal joining conditions was made taking into consideration the volumetric ratio and the ultimate tensile force as responses. Since the level of polyamide 6 degradation is not negatively influencing the joint strength, the variable can be left out of the optimization study. Two BBD conditions had the optimal type of failure - through the metallic rivet (Type I); this

means that during the investigations optimal conditions were already achieved. C8 had a VR=0.72 and achieved 4901 N in the tensile test; C13 also had a VR=0.72 and achieved 4937 N in the tensile test. According to the obtained data, an optimized joining condition is achieved when the Volumetric Ratio is equal or higher than 0.72 and the ultimate tensile force is equal or higher than 4900 N (see Figure 4.22). . In Figure 4.34 the overlaid contour plot of the ultimate tensile force and volumetric ratio with the boundaries selected and the two conditions, C8 and C13, are shown. The overlaid contour plot was planned using a constant value of 2200 N for the Joining Force, since this parameter has the highest influence on the ultimate tensile force.

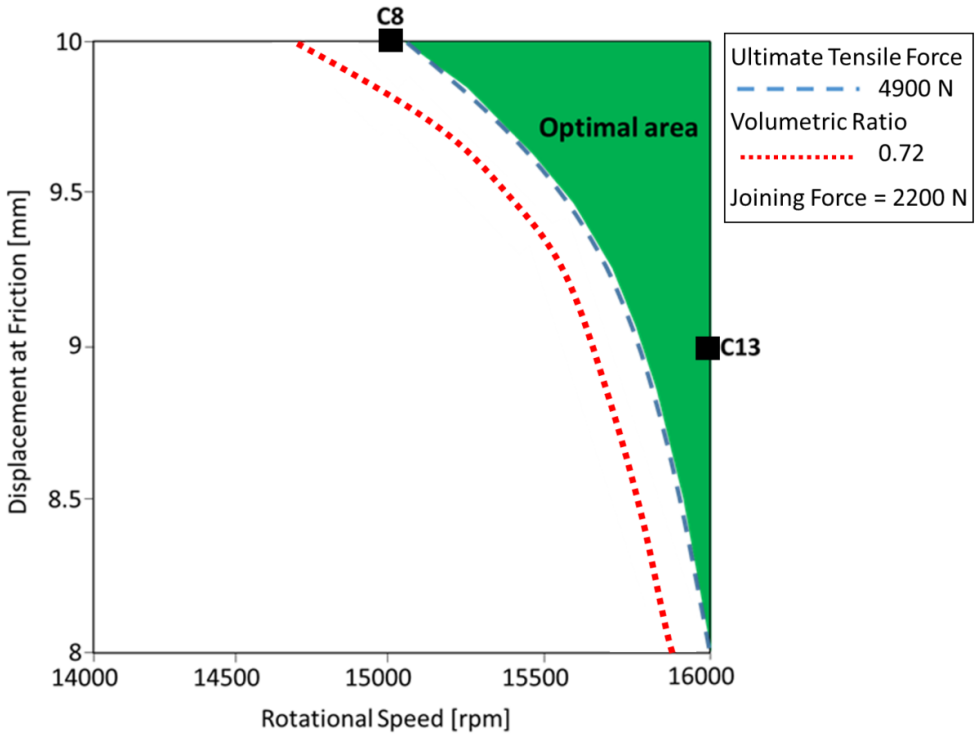

Figure 4.34 Optimal process area obtained by overlaid contour plots for both Volumetric Ratio and Ultimate Tensile Force.

It can be observed in Figure 4.34 that the condition C8 is not inside the optimum area. This occurs because the predicted value (4809 N) was slightly lower than the experimental value (4901N) while graph was plotted using the predicted values. Nevertheless, an optimal working area was determined and the BBD condition C13 is within this area. For the following investigation, C13 was selected as the optimal joining condition for the final analysis.

4.7 Effect of Post Joining Heat Treatment on the Ultimate Tensile Force of Joints

The process-related thermal changes in FricRiveting induce the undermatching of the local mechanical properties (i.e. decrease in microhardness) in aluminum metallic rivet, as discussed in Section 4.2.1, whereby the original T6 temper was lost. This led to a decrease of 8 ± 1% in the ultimate tensile force of the friction riveted joints in comparison with the base material for three replicates of the optimal condition C13. Metallurgical transformations such as, dissolution of the precipitates have been reported in the literature for other heat treatable alloys joints manufactured by friction stir welding [92,93,98,99,116,117]. In these studies the use of a post-weld heat treatment has been reported to allow for significant recovery of the local and global mechanical properties by re-precipitation (coherent precipitates are formed) [92,93,116,117] For the current work the C13 joint replicates were subjected to a PJHT as described in Section 3.3.11. The ultimate tensile force of the joint, microhardness of the metallic rivet and degree of crystallinity of the CTMAZ were analyzed after the PJHT. Figure 4.35 shows the microhardness distribution for the base material rivet, condition C13 and condition C13 after the PJHT.

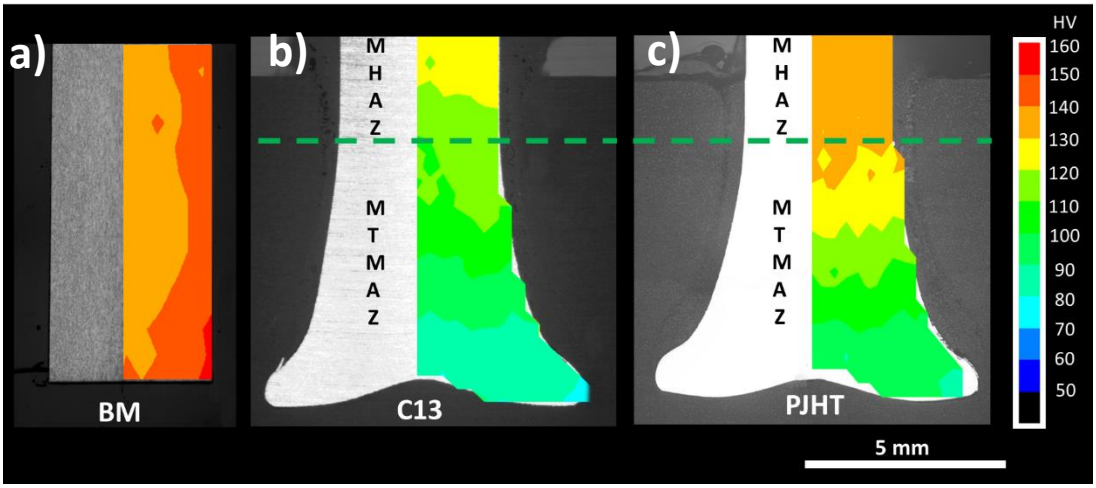

Figure 4.35 Microhardness distribution for the AA6056-T6 base material (BM) (a) and for a joint produced with condition C13 before (b) and after the post joining heat treatment (c). The dashed-line was added to emphasize the approximate transition between MHAZ and MTMAZ.

From the Figure 4.35, a significant increase in average microhardness after the PWHT can be observed for condition C13. In the MTMAZ and MHAZ the microhardness increased by 20 HV compared to condition C13. The MHAZ of condition C13 after the PJHT has almost with the same average microhardness values as the base material (BM = 139 ± 2 HV and C13 after the PWHT = 136 ± 2). Considering these results, re-precipitation may be occurring during PJHT, explaining the microhardness increase after the PJHT.

The degree of crystallinity of condition C13 after the PJHT was 31.1 ± 0.8 %, making up an increase of 15 % in comparison to the base material (26.6 ± 0.7 %). This may be explained by the heat treatment temperature of 180 °C, which is near to the crystallization temperature of polyamide 6 (T_C =185 °C [28]). Appendix E shows the DSC diagrams for the composite base materials and C13 after the heat treatment.

Moreover the joints were weighted before and after the PWHT to evaluate water content. The weight reduction related with the absorbed water was 2 % after PJHT (from 0.352 ± 0.02 % to 0.345 ± 0.03 %). It is well known that water in polyamide 6 acts like as a plasticizer [28]. Therefore, reducing water content will stiffen the composite base plate; if the combined effect of increase in crystallinity and elimination of structural is considered one may expect that an increase in resistance to the rivet pulling during the T-pull tensile testing (i.e. the composite volume of interaction is stronger).

Figure 4.36 shows the average ultimate tensile force for condition C13, C13 after the PJHT and the base material. Three replicates were produced for each condition.

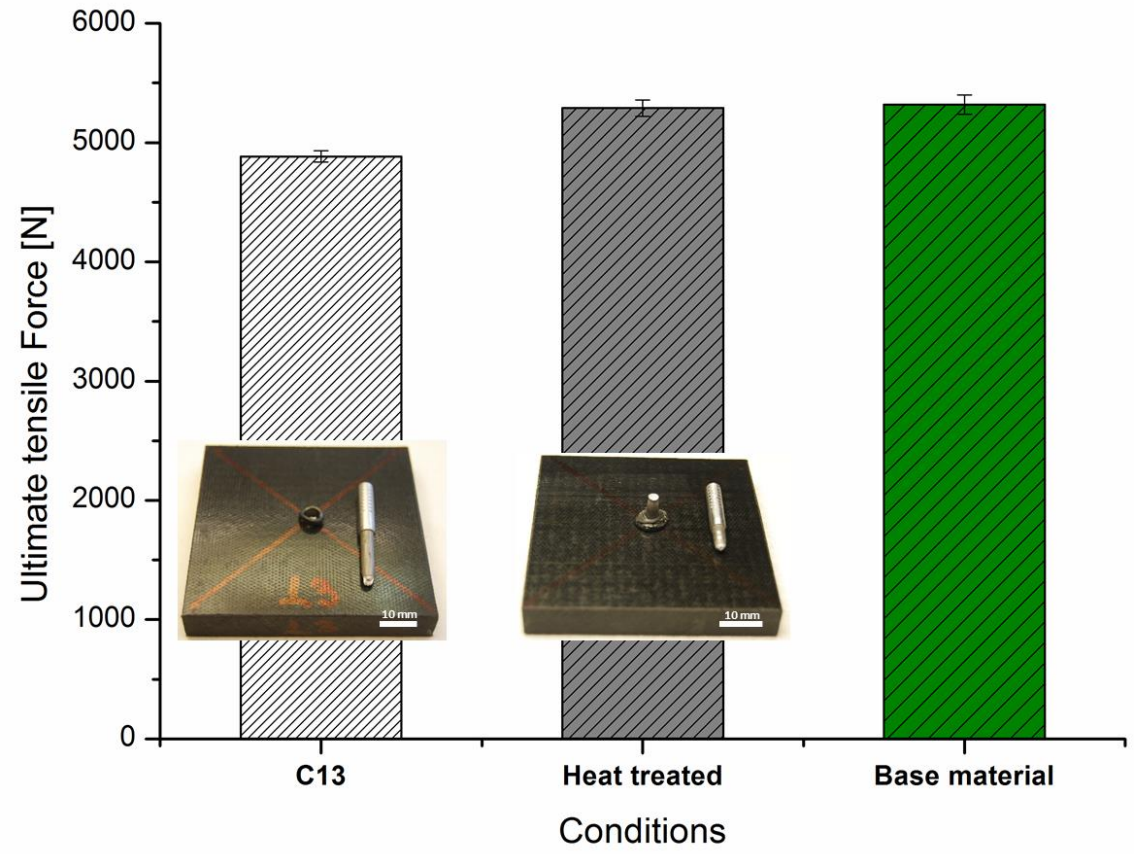

Figure 4.36 Average ultimate tensile forces for the joints produced with condition C13 before and after the post weld heat treatment and for the AA6056-T6 base material.

Figure 4.36 shows that the heat treatment increased the ultimate tensile force of the joints. AA6056-T6/PA6-30GF joints produced under condition C13 achieved 4884 ± 48 N and the fracture occurred on the metallic rivet outside of the polymer composite plate (Figure 4.36). The same condition, C13, after the post joining heat treatment achieved 5261 ± 68 N, an increase of 7.7 % on the ultimate tensile force. The fracture of C13 after the PWHT occurred on the metallic rivet outside of the polymer composite plate, further away from the surface of the composite plate than in C13. The condition C13 after the PWHT has achieved the same average ultimate tensile force as the rivet base material (5320 ± 102 N). This result shows that the mechanical properties of AA6056-T6/PA6-30GF friction-riveted joints can be improved after the process by post weld heat treatment, as the original temper T6 was reestablished and the

composite base plate had an increased strength through the combined effect of structural water elimination and increase in crystallinity.

4.8 Influence of Natural Weathering on the Ultimate Tensile Force of Joints

Glass fiber reinforced polyamide 6 is used in industrial applications where the dimensional stability and high stiffness are required [16]. Within these applications, PA6 may absorb water or suffer a certain degree of degradation. This can lead to dimensional distortion or loss in stiffness, as already described in Section 2.1.2. The effects of natural weathering on AA6056-T6/PA6-30GF friction-riveted joints were analyzed focusing on the ultimate tensile force. The optimal condition C13 (RS: 16000 rpm, DaF: 9 mm, JF: 2200 N, and FoT: 3 s) was selected and replicated for this study. The AA6056-T6/PA6-30GF joints were T-pull tensile tested after 6 months and 12 months exposure time, respectively. The joints were weighted and exposed to natural weathering conditions in Geestacht (53°26′N 10°22′E) on the 1st of February 2015. The joints underwent a large amplitude of the temperature from - 6°C in February up to 36 °C in July, a difference of 42 °C. The humidity and precipitation average for this period were, respectively, 76 % and 5.5 mm. For the 12 months period a higher amplitude of the temperature was recorded (ΔT= 45 °C) considering that the samples were exposed to colder winter conditions. The humidity and precipitation average for the 12 months period were, 81 % and 7.1 mm, respectively. Figure 4.37 shows the joints under the weathering conditions. Figure 4.37-a is a picture taken on a sunny day (June 15th, 2015, T= 15 °C and 65 % of humidity) and Figure 4.37-b on a snowy day (January 5th, 2017, T= -8 °C and 66 % of humidity).

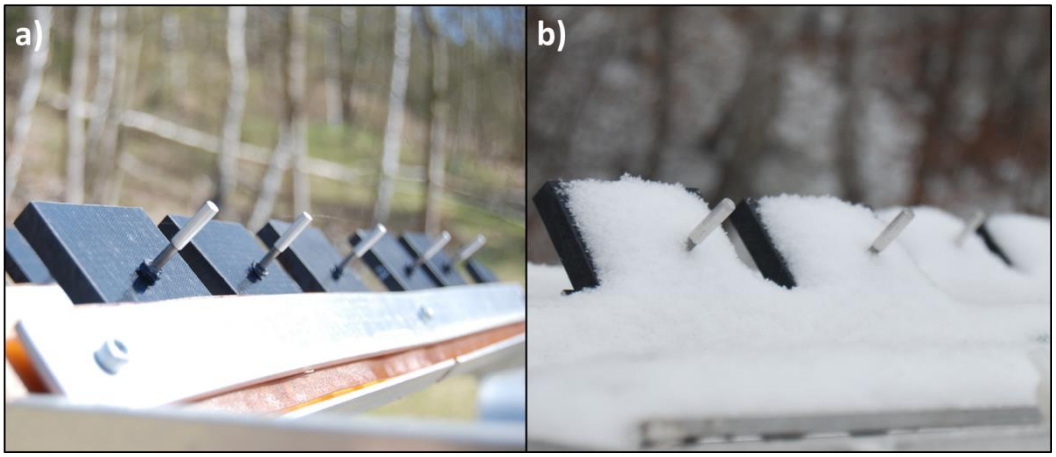

Figure 4.37 Joints exposed to natural weathering during summer (a) and winter (b).

Figure 4.38 shows the ultimate tensile force and variation in weight percent for as-joined condition C13, C13 after 6 months, and C13 after 12 months. Five replicates for each analysis were tested.

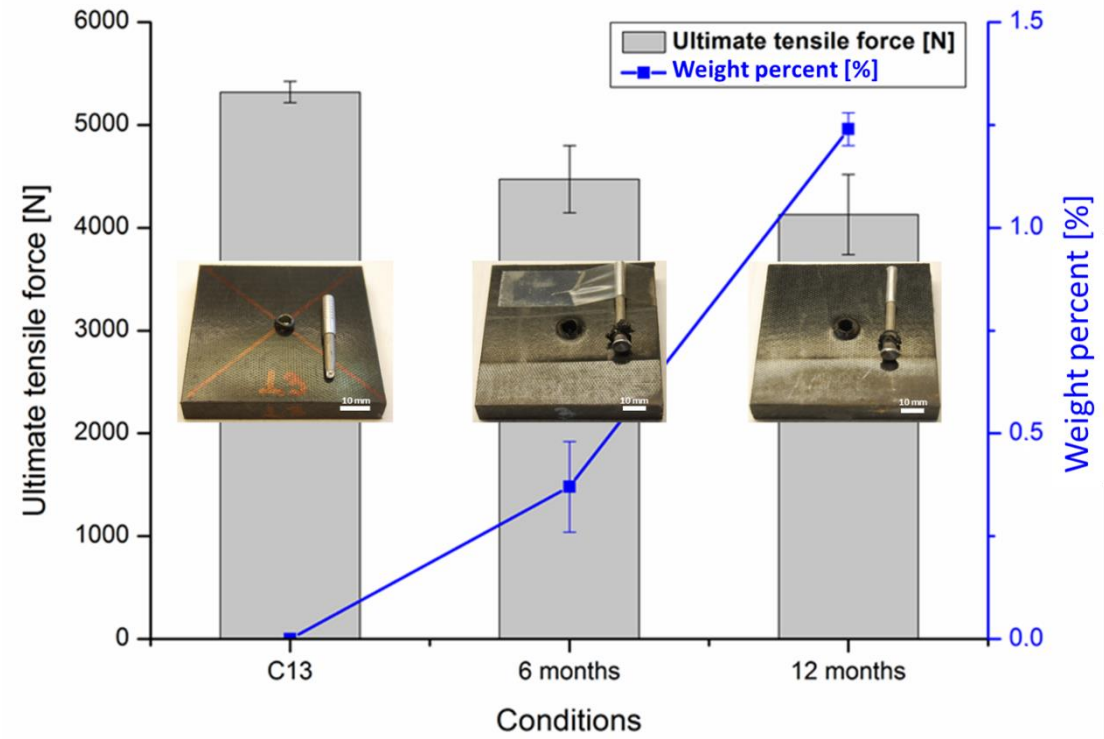

Figure 4.38 Ultimate tensile force and weight percent changes of the AA6056-T6/PA6-30GF joints produced with condition as-joined C13, C13 after 6 months and C13 after 12 months.

The joint weight increased by 0.38 ± 0.11 % in 6 months and 1.24 ± 0.04 % in 12 months. Considering that water absorption occurs by diffusion from the environment to the polyamide 6 matrix [28], two main testing variables are probably influencing the results in this case: the temperature amplitude and the high humidity values. This absorption of water leads to a loss in stiffness of the polyamide 6 matrix, as described in Section 2.1.2. The plasticizing effect of water on polyamide will decrease the rivet anchoring performance as mechanical properties undermatching will eventually take place in the polymer matrix volume of interaction. After 6 months of exposure, the UTF of AA6056-T6/PA6-30GF joints produced under condition C13 was reduced to 4473 ± 326 N, which represents a decrease of 8.4 % in comparison with the corresponding unexposed joint. Moreover, the failure type changed from Type I to Type III (full rivet pullout). After 12 months of exposure, the UTF was reduced to 4128 ± 390 N (15.5 % lower than the unexposed joint), while the fracture mode (Type III) was the same of the condition C13 after 6 months.

Another factor that should be taken into consideration in the analysis of UTF decrease after weathering is the degradation of the PA6, since hydrolysis can occur even at ambient temperatures. In order to check this, dilute solution viscosity measurement was applied on the flash material extracted from the weathered specimens following the procedure described in Section 3.4.6. The viscosity average molecular weight of PA6 in the samples extracted from the C13 joint exposed to natural weathering during 6 months and 12 months was 32700 ± 500 g/mol and 31900 ± 300 g/mol, respectively, which represents decreases of 1.3 % and 3.8 % in comparison with the unexposed joint (33100 ± 800 g/mol). Although it is reasonable to assume that the effect of degradation is less significant than the water absorption in PA6, further studies should be performed to confirm this assumption.

4.9 Summary of Results

The analyses and results covered the scientific and technical purpose of the work.

- Fifteen joining conditions were used in this study based on the Box Behnken Design. Rotational Speed (RS), Displacement at Friction (DaF) and Joining Force (JF) were the parameters varied in this study. These parameters contribute directly and indirectly to the heat generation by friction. The heat input on this study was considerably high, leading to process temperatures up to 387 ± 12 °C, 82 % of the degradation onset of PA6-30GF. Thus, some degree of degradation of the polymeric matrix in the CTMAZ was intrinsic to the process; however, this does not compromise the mechanical performance of the joints. The process temperature reached 64 % of the AA6056 melting temperature. As a consequence, the metallic rivet was deformed plastically leading to partial dynamic recovery and recrystallization and the dissolution of the precipitates in the aluminum matrix at the rivet tip (i.e. the anchoring zone). The joints achieved a wide range of volumetric ratios.
- The influence of the process on the metallic part was investigated based on a high-heat-input-joint, condition C13. In comparison with the base material, the aluminum microstructure did not change in the Metal Heat Affected Zone (MHAZ). In the Metal-Thermo-Mechanically Affected Zone (MTMAZ), grain refinement was observed possibly due to dynamic recrystallization, an increase in grain low angle boundaries was observed by EBSD analysis. The microhardness measurement within the metallic rivet evidenced a larger decrease in hardness in the MTMAZ (40 %) due to the dynamic and static metallurgical transformations observed; this change in local mechanical properties was associated with the dissolution of the precipitates and other annealing phenomena that cannot be observed by LOM or SEM. A smaller decrease in hardness on the MHAZ was observed and might be correlated to annihilation of dislocation and dissolution or growth (loss of coeherence) of the precipitates.
- The influence of the process on the polymer composite part was investigated using a high heat input joint (Condition C13). In terms of

polymer composite, the limits between the Composite-Thermo-Mechanically Affected Zone (CTMAZ) and the Composite-Heat-Affected Zone (CHAZ) was observed but the limits between CHAZ and the base material could not be solved by microscopy. The CTMAZ was identified as the region with fiber reoriented in the direction of the rivet rotation and a few volumetric defects generated by water evolution or some thermos-mechanical degradation and. The interface between CTMAZ and CHAZ was identified as the region with the largest amount of volumetric defects. These defects might be correlated to water evolution, possible thermo-mechanical degradation and the interaction between the molten composite and the rotating rivet (Weissenberg effect). The phenomena are occurring together and the squeeze flow might be also pushing bubbles from the related water evolution, additives and degradation products to the region with largest amount of volumetric defects.

- Three conditions with low, medium and high heat inputs (C3, C9 and C13, respectively) were analyzed by DSC. The high shear rates and process temperatures imposed by the FricRiveting process did not result in any significant change in the degree of crystallization of PA6, as well as in Tc. The different levels of PA6 chain scission and the high level of PA6 chain orientation in the CTMAZ imposed by the rotating tool does not appear to influence the recrystallization of PA6.
- The influence of the FricRiveting process conditions on PA6 degradation in Composite-Thermo-Mechanically Affected Zone (CTMAZ) was investigated by dilute solution viscosity measurements. Additionally, ATR/FT-IR analysis was performed, for samples taken from joint produced with conditions C3, C9 and C13. As the composite was not dried prior to joining, and the FricRiveting was performed at ambient conditions - that is, an environmental with humidity and O_2 - some degree of the thermal-mechanical degradation of PA6 is inherent. The condition that achieved the highest process temperature, C13, had a decrease on viscosity average molecular weight of 18 % in

comparison to the base material. It was shown that viscosity average molecular weight of PA6 decreases almost linearly with the increase in the process temperature. From the ATR/FT-IR measurements. a new peak related to carbonyl compounds was observed between 1710 cm^{-1} and 1760 cm^{-1} in comparison with the base material for the three selected conditions. Carbonyl compounds, such as aldehydes and ketones, are produced by the thermo-oxidative degradation of PA6. A similar trend between process temperature and thermo-oxidative degradation was observed in the ATR/FT-IR measurements. Therefore the ATR/FT-IR helped confirming the results of the dilute solution viscosity measurements, whereby the process-related thermo-mechanical changes in the composite took place.

- The glass fiber length in the Composite-Thermo-Mechanically Affected Zone (CTMAZ) of three selected joint conditions C3, C9 and C13 was measured and compared with the base material. The number-average fiber length for base material and joints produced with conditions C3, C9 and C13 was 276 µm, 174 µm, 175 µm and 170 µm, respectively. The glass fiber lengths in the CTMAZ of these joints are slightly higher than the critical value for effective reinforcement (167 µm) of composite. The high breakage of the glass fibers and the similar average sizes and distribution for the investigated joining conditions occur mainly because the FricRiveting process starts in the solid state. Nevertheless, the global mechanical performance is not affected due to larger volume Composite Heat Affected Zone (CHAZ) in comparison to the very thin CTMAZ (i.e. the consolidated composite layer around the rivet).
- The ultimate tensile force of joints ranged between 1862 N and 4937 N depending on the volumetric ratio. The joints failed through two failure modes: full rivet pull-out (Failure Type 3, Figure 4.23) and fracture through the metallic rivet outside the composite plate (Failure Type 1, Figure 4.23). Condition C8 and C13 resulted in the strongest joints, which achieved 92 % of the ultimate tensile force of the metallic rivet.

This 8 % of decrease was proven to be unrelated to the polymer degradation or fiber breakage on the CTMAZ since the fracture occurred in the metallic rivet. The process-related annealing phenomena reduced the local mechanical properties of the rivet and consequently the joint global mechanical properties. The correlation between Ultimate Tensile Force (UTF) and Volumetric Ratio (VR) was linear, whereby high volumetric ratio values resulted in high mechanical strength joints.

- Fracture analysis was carried out by SEM to address the micro-mechanisms of failure. The Composite-Thermo-Mechanically Affected Zone (CTMAZ) was pulled out with the metallic rivet during T-pull tensile testing for a failure Type III in FricRiveting (Figure 4.26). The ductile fracture of the metallic rivet characterized by the presence of the micro voids was observed for a failure Type I (Figure 4.26). This fracture characterizes the best type of fracture in terms of UTF.
- Statistical analysis of the effects of process parameters on process temperature, polymer degradation and mechanical performance was carried out. The flash material temperature was influenced mainly by the friction phase parameters - Rotational Speed (RS) and Joining Force (JF) - since they are responsible to generate the frictional heat. The JF was the parameter that had the highest influence on the flash material temperature, with higher values of JF generating the highest process temperatures. Viscosity average molecular weight (MW) of PA6 in CMHAZ is sensitive to the heat generated and shear rate imposed, consequently RS and JF are the parameters that most influence it. The RS had the highest influence on MW, with higher values of RS providing the greater decrease on the MW. Ultimate Tensile Force (UTF) is directly dependent on the shape and amount of plastic deformation in the rivet tip, in other words the rivet anchoring zone; it was shown that the formation of the anchoring zone is directly dependent of the heat generated and force applied during the process. Thus, UTF is influenced by RS, DaF and JF. The JF was the parameter

with the highest positive influence on the ultimate tensile force, since the JF is not only responsible for the heat generation but also for the deformation of the metallic rivet.

- An optimized joining condition (C13; RS: 16000 rpm, DaF: 9 mm e JF: 2200 N) was selected using validated statistical models. The condition was replicated and its reproducibility analyzed. All the replicates fractured through the metallic rivet - the type of fracture under T-pull tensile testing displaying the best performance - reaching 4884 ± 48 N (92% of the ultimate tensile force of the metallic rivet).
- The joint produced with optimized condition (C13) was submitted to post joining heat treatment (PJHT). An increase in ultimate tensile force of 7.7 % was observed after the PJHT. The final joint failure occurred by the through the metallic rivet failure, which indicates that the mechanical properties of the metallic were improved by the PJHT. This assumption was confirmed by the microhardness measurements, whereby an increase in hardness was observed for the PJHT specimens.
- The effect of natural weathering was analyzed for the as-joined optimized condition (C13). The joints displayed a decrease in the ultimate tensile force of 8.4 % after 6 months and 15.5 % after 12 months. These were related to a probable occurrence of the water absorption by the PA 6 matrix, thereby plasticizing the polyamide 6 matrix leading to a decrease in stiffness.

5 CONCLUSIONS

The feasibility of a new FricRiveting process variant (controlled by force; limited by displacement and time) was successfully demonstrated for the material combination of 30 wt% short glass fiber reinforced polyamide 6 composite and 6056-T6 aluminum alloy rivets. Moreover, the results of simple and effective design of experiments (the first-time use of BBD-design in FricRiveting) and statistical analysis, as well as the use of advanced analytical techniques has provided a basis for the understanding of the new joining process variant. Through these techniques an optimized joining condition (C13; RS: 16000 rpm, DaF: 9 mm e JF: 2200 N) was selected. Joints produced at this condition achieved the highest value of ultimate tensile force (4884 ± 48 N, 92 % of the ultimate tensile force of the metallic rivet) even with a considerable area of volumetric defects on the polymer composite part, a decrease on the viscosity average molecular weight of polyamide 6 (18 %) and annealing phenomena on the metallic part. The quasi-static global mechanical strength was improved using a post joining heat treatment; the joint achieved 99% of the ultimate tensile force of the metallic rivet (5261 ± 68 N). Natural weathering showed a negative effect on the joint mechanical strength due to water absorption by the PA 6 matrix of composite. In summary, this master thesis has accomplished its scientific and engineering objectives. The work has provided a relevant contribution to the state of the art in FricRiveting.

6 RECOMMENDATIONS FOR FUTURE WORK

Although this master dissertation fulfilled its proposed objectives, further investigations are necessary to understand the new process variant and to support the transfer of FricRiveting in the automotive industry for this combination of materials in. This may include:

• The metallurgical phenomena occurring on the MTMAZ should be carefully analyzed, for instance through Transmission Electron Microscopy (TEM). Thus, dissolution of the precipitates and distribution of dislocation could be better understood and support our assumptions on the joint local mechanical properties.

• The fatigue properties must be analyzed, in face of the future industrial applications.

• The influence of filler and absorbed water content on joint formation, i.e. formation and shape of the rivet anchoring zone, and process temperature.

• The comparison between friction riveted joints and screwed joints in terms of: mechanical performance, manufacturing time and costs.

7 REFERENCES

[1] AMANCIO-FILHO, S. T.; DOS SANTOS, J.F. “Joining of polymers and polymer–metal hybrid structures: Recent developments and trends”, *Polym. Eng. Sci.*, vol. 49, no 8, p. 1461–1476, Aug. 2009.

[2] "Innovative Ideas for Metal Replacement”, *Dupont Webpage*. [Online]. Available at: http://www.dupont.com/products-and-services/plastics-polymers-resins/articles/innovative-ideas-for-metal-replacement.html. [Accessed: 30-Nov-2015].

[3] MICHALOS, G. *et al.* “Automotive assembly technologies review: challenges and outlook for a flexible and adaptive approach”, *CIRP J. Manuf. Sci. Technol.*, vol. 2, nº 2, p. 81–91, 2010.

[4] MALLICK, P. K. *Materials, Design and Manufacturing for Lightweight Vehicles*. Elsevier, 2010.

[5] KAH, P. *et al.* “Techniques For Joining Dissimilar Materials: Metals and Polymers”, *Rev. Adv. Mater. Sci.*, p. 152–164, 2014.

[6] BALDAN A., “Adhesively-bonded joints in metallic alloys, polymers and composite materials: Mechanical and environmental durability performance”, *J. Mater. Sci.*, vol. 39, nº 15, p. 4729–4797, Aug. 2004.

[7] NIU, M. *Airframe structural design: practical design information and data on aircraft structures*. California: Conmilit Press, 1988.

[8] AMANCIO-FILHO, S.T.; BEYER, M.; DOS SANTOS, J.F. “Method of connecting a metallic bolt to a plastic workpiece”, US7575149 B2, Aug. 2009.

[9] AMANCIO-FILHO, S.T. “Friction riveting (FricRiveting). Development of a new joining technique for polymer-metal hybrid joints). Part II: thermal and mechanical properties”, *Soldag. Amp Insp.*, vol. 16, nº 4, p. 396–404, Dec. 2011.

[10] RODRIGUES, C.F. *et al.* “FricRiveting of aluminum 2024-T351 and polycarbonate: Temperature evolution, microstructure and mechanical performance”, *J. Mater. Process. Technol.*, vol. 214, nº 10, p. 2029–2039, Oct. 2014.

[11] BLAGA, L. A. *et al*. “Friction Riveting of glass–fibre-reinforced polyetherimide composite and titanium grade 2 hybrid joints”, *Mater. Des.*, vol. 50, p. 825–829, Sep. 2013.

[12] ALTMEYER, J. *et al*. “Effect of the friction riveting process parameters on the joint formation and performance of Ti alloy/short-fibre reinforced polyether ether ketone joints”, *Mater. Des.*, vol. 60, p. 164–176, Aug. 2014.

[13] BORBA, N. Z. *et al.* “Friction Riveting of Pultruded Thermoset Glass Fiber Reinforced Polyester Composite and Ti6Al4V Hybrid Joints”, Las Vegas, ANTEC 2014.

[14] BORBA, N. Z. *et al.* “On the Process-Related Rivet Microstructural Evolution, Material Flow and Mechanical Properties of Ti-6Al-4V/GFRP Friction-Riveted Joints”, *Materials*, vol. 10, nº 2, p. 184, Feb. 2017.

[15] PROENCA, B. C. *et al.* “Force-Controlled Friction Riveting Of Glass Fiber Reinforced Polyamide 6 and Aluminum Alloy 6056 Hybrid joints”, Orlando, ANTEC 2015.

[16] MARCOS, H. “Polyamides, polyesters and elastomeric thermoplastics: a sustainable perspective in modern industry”, *Polímeros*, vol. 22, nº 2, p. 107–110, Jan.2012.

[17] MAXWELL, J. *Plastics in the automotive industry*. Cambridge: Woodhead Publishing Ltd; 1994.

[18] IWAYAMA, I. *et al*. “6056 Aluminum Alloy Wire for Automotive Fasteners”, *SEI Tech. Rev.*, vol. 77, p. 74–78, 2013.

[19] “Polymer manufacturers develop novel solutions for the auto industry”. [Online]. Available at: http://goo.gl/s99OGV. [Accessed: 15-Jul-2016].

[20] MUKHOPAHYAY, P. “Alloy Designation, Processing, and Use of AA6XXX Series Aluminium Alloys”, *Int. Sch. Res. Not. Int. Sch. Res. Not.*, vol. 2012, Apr. 2012.

[21] SHEPPARD, T. *Extrusion of Aluminium Alloys*. Springer Science & Business Media, 1999.

[22] ASM METALS HANDBOOK. *Properties and Selection: Nonferrous Alloys and Special-Purpose Materials*, vol. 2. ASM Metals Handbook, Oct. 1990.

[23] GGD metals company, “Aluminum datasheet”. [Online]. Available at: http://www.ggdmetals.com.br/cat/aluminio.pdf. [Accessed 23-Mar-2015].

[24] MENG, C. “Effect of preheating condition on strength of AA6060 Aluminium Alloy for extrusion”, PhD Thesis, Auckland University of Technology, New Zealand, 2010.

[25] ASM METALS HANDBOOK. *Heat Treating*, vol. 4. ASM Metals Handbook, 1991.

[26] EDWARDS, G. A. *et al.* "The precipitation sequence in Al–Mg–Si alloys." Acta Materialia, v. 46, n. 11, p. 3893-3904, 1998.

[27] Aluminum 6056 datasheet, "Grades 6056 comparison! [Online]. Avaiable at: http://www.clintonaluminum.com/wp-content/uploads/2014/08/Grades-6056-Comparison-vs-6061-2024-7075-.pdf. [Accessed: 23-Mar-2015].

[28] KOHAN, M. I. *Nylon Plastics Handbook*. Hanser/Gardner Publications, 1995.

[29] MARK, H.; STAFFORD, G. “Collected Papers Of Wallace Hume Carothers On High Polymeric Substances, Interscience Publishers Inc, 1940.

[30] ZIMMERMAN, J.; KOHAN, M. I. “Nylon–selected topics”, *J. Polym. Sci. Part Polym. Chem.*, vol. 39, nº 15, p. 2565 – 2570, 2001.

[31] NANYING JIA, H. A. F. “Effects of Moisture Conditioning Methods on Mechanical Properties of Injection Molded Nylon 6”, *J. Reinf. Plast. Compos. - J REINF PLAST Compos.*, vol. 23, nº 7, p. 729–737, 2004.

[32] PEZZIN, G.; GECHELE, G. B. “Capillary viscometry of molten polycaprolactam”, *J. Appl. Polym. Sci.*, vol. 8, nº 5, p. 2195–2212, Sep. 1964.

[33] CHAWLA, K. K. *Composite Materials: Science and Engineering*. Springer Science & Business Media, 2012.

[34] Polyamide 6 Datasheet, “Ultramid ® 8200 HS Polyamide 6”. Available at: http://iwww.plasticsportal.com/products/dspdf.php?type=iso&param=Ultramid+8200+HS. [Accessed: 24-Dec-2015].

[35] Polyamide 6 reinforced with 33% of short glass fiber Datasheet “Ultramid 8233G HS BK-102 Polyamide 6”. Available at: http://iwww.plasticsportal.com/products/dspdf.php?type=astm&param=Ultramid+8233G+HS+BK-102. [Accessed: 24-Dec-2015].

[36] DAVIS, R. D.; GILMAN, J. W.; VANDERHART, D. L. “Processing degradation of polyamide 6/montmorillonite clay nanocomposites and clay organic modifier”, *Polym. Degrad. Stab.*, vol. 79, nº 1, p. 111–121, 2003.

[37] GOLDFARB, I. J.; MEEKS, A. C. *Thermal Degradation of Polyamides - Part I. Aliphatic Polymers*, Technical Report, Feb. 1969.

[38] LEVCHIK, S. V.; WEIL, E. D.; LEWIN, M. “Thermal decomposition of aliphatic nylons”, *Polym. Int.*, vol. 48, nº 7, p. 532–557, Jul. 1999.

[39] PRAMODA, K. P. *et al*. “Thermal degradation behavior of polyamide 6/clay nanocomposites”, *Polym. Degrad. Stab.*, vol. 81, nº 1, p. 47–56, 2003.

[40] LEVANTOVSKAYA, I. I. *et al*. “Mechanism of thermal oxidative degradation of polyamides”, *Polym. Sci. USSR*, vol. 6, nº 10, p. 2089–2095, 1964.

[41] CERRUTI, P. *et al*. “Comparison of photo-oxidative degradation of polyamide 6,6 films stabilized with HALS and $CuCl_2$+KI mixtures”, *Polymer*, vol. 46, nº 13, p. 4571–4583, Jun. 2005.

[42] DONG, W.; GIJSMAN, P. “Influence of temperature on the thermo-oxidative degradation of polyamide 6 films”, *Polym. Degrad. Stab.*, vol. 95, nº 6, p. 1054–1062, Jun. 2010.

[43] GRIGG, M. N. “Themo-Oxidative Degradation Of Polyamide 6”, PhD Thesis, Queensland University of Technology, Brisbane, Australia, 2006.

[44] LANSKA, B.; MAKAROV, G. G.; SBENDA, J. “Termination reaction in the chain oxidation of caprolactam”, *Angew. Makromol. Chem.*, vol. 181, nº 1, p. 143–152, Oct. 1990.

[45] LANSKA, B. “Thermo-oxidation of lactam-based polyamides with carboxylic end-groups. Decomposition of 6-hydroperoxy-6-hexanelactam in the presence of carboxylic acids”, *Eur. Polym. J.*, vol. 30, nº 2, p. 197–204, Feb. 1994.

[46] GONÇALVES, J. “Friction Spot Welding (FSpW) of Polyamide 6”, Master Thesis, Federal University of São Carlos, Brazil, 2015.

[47] THOPPUL, S. D.; FINEGAN, J.; GIBSON, R. F. “Mechanics of mechanically fastened joints in polymer–matrix composite structures – A review”, *Compos. Sci. Technol.*, vol. 69, nº 3–4, p. 301–329, Mar. 2009.

[48] GRUJICIC, M. *et al.*, “An overview of the polymer-to-metal direct-adhesion hybrid technologies for load-bearing automotive components”, *J. Mater. Process. Technol.*, vol. 197, nº 1–3, p. 363–373, Feb. 2008.

[49] BALLE, F.; WAGNER, G.; EIFLER, D., “Ultrasonic Metal Welding of Aluminium Sheets to Carbon Fibre Reinforced Thermoplastic Composites”, *Adv. Eng. Mater.*, vol. 11, nº 1–2, p. 35–39, Jan. 2009.

[50] MITSCHANG, P.; VELTHUIS, R.; DIDI, M. “Induction Spot Welding of Metal/CFRPC Hybrid Joints”, *Adv. Eng. Mater.*, vol. 15, nº 9, p. 804–813, Set. 2013.

[51] AGEORGES, C.; YE, L. Resistance Welding of Metal/Thermoplastic Composite Joints. Journal of Thermoplastic Composite Materials, vol. 14, 6, pp. 449–475, 2001.

[52] ABIBE, A. B. *et al*. “On the feasibility of a friction-based staking joining method for polymer-metal hybrid structures”, *Mater. Des.* Vol. 92, p. 632–642, Feb. 2015.

[53] ABIBE, A. B. *et al*. “A method for joining a plastic workpiece to a further workpiece”, Patent application EP14182938.2, 2014.

[54] GOUSHEGIR, S. M. *et al* “Friction Spot Joining of aluminum AA2024/carbon-fiber reinforced poly(phenylene sulfide) composite single lap joints: Microstructure and mechanical performance”, *Mater. Amp Des.*, vol. 54, p. 196–206, 2014.

[55] AMANCIO-FILHO, S. T.; DOS SANTOS, J. F., “Method for joining metal and plastic workpieces" European Patent 2329905B1, 2012.

[56] GASPARIN, A. L. “Metal-polymer adhesion: Measurement devices and physical-chemical correlations”, PhD Thesis, Federal University of Rio Grande do Sul, Brazil, 2011.

[57] HIGGINS, A. “Adhesive bonding of aircraft structures”, *Int. J. Adhes. Adhes.*, vol. 20, nº 5, p. 367–376, 2000.

[58] HOLLAWAY, L. C. “A review of the present and future utilisation of FRP composites in the civil infrastructure with reference to their important in-service properties”, *Constr. Build. Mater.*, vol. 24, nº 12, p. 2419–2445, Dec. 2010.

[59] GRANDT, A. F. “Materials Degradation and Fatigue in Aerospace Structures”, Aug. 1997.

[60] Polyone, “Injection Over molding Guide”. [Online]. Available at: http://www.polyone.com/files/resources/Overmold_Design_Guide.pdf. [Accessed: 01-Mar-2016].

[61] RINK, M., “Device for producing bonded parts”, US005940949A, 1999

[62] Polymotive, “Plastic-Metal Hybrid Material” [Online]. Disponível em: http://www.hbmedia.net/polymotive/ polymotive/2003/01/articles/frontend1.shtml. [Accessed: 30-Apr-2015].

[63] GRUJICIC, M. *et al.* “Suitability analysis of a polymer–metal hybrid technology based on high-strength steels and direct polymer-to-metal adhesion for use in load-bearing automotive body-in-white applications”, *J. Mater. Process. Technol.*, vol. 209, nº 4, p. 1877–1890, Feb. 2009.

[64] Lanxess, “Case Hybrid Frontend Ford Focus”. [Online]. Avaiable at: https://techcenter.lanxess.com/scp/emea/en/docguard/TI_2006-024_EN_Case_Hybrid_Frontend_Ford_Focus.pdf?docId=63412. [Accessed: 24-May-2016].

[65] AMANCIO-FILHO, S. T. "Friction Riveting: Development and Analysis of a New Joining Technique for Polymer-Metal Multi-Materials Structures”, PhD Thesis, GKSS-Forschungszentrum Geesthacht: Technischen Universität Hamburg-Harburg, Germany, 2007.

[66] AMANCIO-FILHO, S. T. “FRICTION RIVETING: development and analysis of a new joining technique for polymer-metal multi-material structures”, presented in Welding in the World, 2011.

[67] BLAGA, L. A. “Innovating material in bridge construction. Contribution to construction with composite fiber-reinforced materials”, PhD Thesis, Polytechnic University of Timisoara, Romania, 2012.

[68] ALTMEYER, J. “Fundamental characteristics of friction riveted multi-material joints", Ph.D. Thesis, Technischen Universität Hamburg-Harburg, Hamburg, Germany, 2014.

[69] AMANCIO-FILHO S. T.; DOS SANTOS, J.; VENTZKE, “Determination of fracture mechanism under tensile loading in commercial available

engineering thermoplastic material joined by FricRiveting", presented in 5th International Conference on Fracture of Polymer, 2008.

[70] ASTM INTERNATIONAL, ASTM D3171-99: Standard test methods for constituent content of composite materials. West Conshohocken, Pa, 1999.

[71] BRITISH STANDARD EUROPEAN NORM, BS EN 1435:1997, "Non-destructive examination of welds. Radiographic examination of welded joints", 1997.

[72] ASTM INTERNATIONAL, ASTM E.-10e1: Standard Test Method for Knoop and Vickers Hardness of Materials, West Conshohocken, Pa, 2010.

[73] EHRENSTEIN, G. W.; RIEDEL, G.; TRAWIEL, P. *Thermal analysis of plastics: theory and practice*. Munique: Hanser Verlag, 2004.

[74] ASTM INTERNATIONAL, ASTM E384-10e1: Standard Test Method for Transition Temperatures and Enthalpies of Fusion and Crystallization of Polymers by Differential Scanning Calorimetry, West Conshohocken, 2008.

[75] MILLITARY HANDBOOK, *MIL-HDBK-17-1F: Composite Materials Handbook. Vol. 1. Polymer-matrix Composites Guidelines for Characterization of Structural Materials*, Jan. 1997.

[76] ASTM INTERNATIONAL, ASTM D2857-95: Standard Practice for Dilute Solution Viscosity of Polymers, West Conshohocken, 1995.

[77] PROENCA, B. *et al*. "Comparative analysis of molecular weight measurements of polyamide 6 and solution of formic acid by viscosimetry via dilution and single concentration methods", in *12º Congresso Brasileiro de Polímeros (12º CBPol)*, Florianópolis, 2013.

[78] BILLMEYER, F. W. "Methods for estimating intrinsic viscosity", *J. Polym. Sci.*, vol. 4, nº 1, p. 83–86, Feb. 1949.

[79] BRANDRUP, J.; IMMERGUT, E. H.; GRULKE, E. A. *Polymer Handbook*, Vol. 89. New York: Wiley, 1999.

[80] NOVELLO, M. V.; CARREIRA, L. G.; CANTO, L. B. "Post-consumer polyethylene terephthalate and polyamide 66 blends and corresponding short glass fiber reinforced composites", *Mater. Res.*, vol. 17, nº 5, p. 1285–1294, Oct. 2014.

[81] MONDADORI, N. M. L. *et al*. “Composites of Recycled PET Reinforced with Short Glass Fiber”, *J. Thermoplast. Compos. Mater.*, vol. 25, nº 6, p. 747–764, Sep. 2012.

[82] MONDADORI, N. M. L. *et al*. “Relationship between processing method and microstructural and mechanical properties of poly(ethylene terephthalate)/short glass fiber composites”, *J. Appl. Polym. Sci.*, vol. 109, nº 5, p. 3266–3274, Sep. 2008.

[83] KELLY, A.; TYSON, W. R. “Tensile properties of fibre-reinforced metals: Copper/tungsten and copper/molybdenum”, *J. Mech. Phys. Solids*, vol. 13, nº 6, p. 329–350, Dec. 1965.

[84] AMANCIO-FILHO, S. T. “Friction riveting (FricRiveting). Development of a new joining technique for polymer-metal hybrid joints. Part I: process and microstructure”, *Soldag. Amp Insp.*, vol. 16, nº 4, p. 387–395, Dec. 2011.

[85] BOX, G.E.; BEHNKEN, D.W., “Some new three level designs for the study of quantitative variables”, *Technometrics*, vol. 2, nº 4, p. 455–75, 1960.

[86] FERREIRA, S. L. C. *et al*. “Box-Behnken design: An alternative for the optimization of analytical methods”, *Anal. Chim. Acta*, vol. 597, nº 2, p. 179–186, Aug. 2007.

[87] KARTHIKEYAN, P.; THIAGARAJAN, D.; MAHADEVAN, K. “Study of Relation between Welding and Hardening Parameters of Friction Stir Welded Aluminium 2024 Alloy”, *Procedia Eng.*, vol. 97, p. 505–512, 2014.

[88] SHANMUGA, S. N.; MURUGAN, N. ; URESH, S. “Mathematical Modeling of Ductility of Friction-Stir-Welded AA5083-H321”, vol. 4, nº 1, p. 117–132, Dec. 2011.

[89] DWIVEDI, S. P. “Effect of process parameters on tensile strength of friction stir welding A356/C355 aluminium alloys joint”, *J. Mech. Sci. Technol.*, vol. 28, nº 1, p. 285–291, Jan. 2014.

[90] LI, J. Q.; LIU, H. J. “Optimization of welding parameters for the reverse dual-rotation friction stir welding of a high-strength aluminum alloy 2219-T6”, *Int. J. Adv. Manuf. Technol.*, vol. 76, nº 5–8, p. 1469–1478, Sep. 2014.

[91] VIGNESHWARAN, P. *et al*. “Weld Strength Optimization by using Box-Behnken Design”, apresentado em International Journal of Engineering Research and Technology, 2014, vol. Vol. 3-Issue 4, Apr. 2014.

[92] ELANGOVAN, K.; BALASUBRAMANIAN, V. “Influences of post-weld heat treatment on tensile properties of friction stir-welded AA6061 aluminum alloy joints”, *Mater. Charact.*, vol. 59, nº 9, p. 1168–1177, Sep. 2008.

[93] OLEA, C. A. W. *et al*. “Friction Stir Welding of Precipitate Hardenable Aluminium Alloys: A Review”, *Weld. World*, vol. 50, nº 11–12, p. 78–87, Jan. 2013.

[94] ASTM INTERNATIONAL, ASTM D1435-13: Standard Practice for Outdoor Weathering of Plastics, West Conshohocken, 2013.

[95] AMANCIO-FILHO, DOS SANTOS, J.F. "Preliminary Analytical Modeling of Heat Iinput In Friction Riveting", Indianapolis, ANTEC 2016.

[96] WERENSKIOLD, J. C. “Equal Channel Angular Pressing (ECAP) of AA6082: Mechanical Properties, Texture and Microstructural Development”. PhD Thesis, Norwegian University of Science and Technology, Norway, 2004.

[97] CALLISTER JR W. D. *Fundamentals of materials science and engineering*. John Wiley & Sons, 2001.

[98] GALLAIS, C. *et al*. “Precipitation microstructures in an AA6056 aluminium alloy after friction stir welding: Characterisation and modelling”, *Mater. Sci. Eng. A*, vol. 496, nº 1–2, p. 77–89, Nov. 2008.

[99] SRINIVASAN, P. B. *et al*. “Stress corrosion cracking susceptibility of friction stir welded AA7075–AA6056 dissimilar joint”, *Mater. Sci. Eng. A*, vol. 392, nº 1–2, p. 292–300, Feb. 2005.

[100] TABOR, D. "The Friction and Lubrication of Solids", Oxford University Press, London, United Kingdom, 1954.

[101] WEISSENBERG, K. “A Continuum Theory of Theological Phenomena”, *Nat.* v.159, p. 310-311, Mar.1947.

[102] CHAN, Y.; WHITE, J. L.; OYANAGI, Y. “A Fundamental Study of the Rheological Properties of Glass-Fiber-Reinforced Polyethylene and Polystyrene Melts”, *J. Rheol. 1978-Present*, vol. 22, nº 5, p. 507–524, Oct. 1978.

[103] ZIRNSAK, M. A.; HUR, D. U.; BOGER, D. V. “Normal stresses in fibre suspensions”, *J. Non-Newton. Fluid Mech.*, vol. 54, p. 153–193, Aug. 1994.

[104] J. M. Dealy e T. K. P. Vu, “The Weissenberg effect in molten polymers”, *J. Non-Newton. Fluid Mech.*, vol. 3, nº 2, p. 127–140, nov. 1977.

[105] ASM Metals HandBook, *Metal Working: Sheet Forming*, vol. 14B. ASM Metals Handbook, 2006.

[106] LAURENT, H. *et al.*, “Mechanical Behaviour and Springback Study of an Aluminium Alloy in Warm Forming Conditions”, *Int. Sch. Res. Not.*, vol. 2011, p. e381615, Apr. 2011.

[107] LI, D. and GHOSH, A. “Tensile deformation behavior of aluminum alloys at warm forming temperatures”, *Mater. Sci. Eng. A*, vol. 352, nº 1–2, p. 279–286, Jul. 2003.

[108] INCEOGLU, F. *et al*, “Correlation Between Processing Conditions and Fiber Breakage During Compounding of Glass Fiber-Reinforced Polyamide”, *ResearchGate*, vol. 32, nº 11, p. 1842–1850, Nov. 2011.

[109] BECKER, W.T. and LAMPMAN, S. “Fracture Appearance and Mechanisms of Deformation and Fracture - Heat Treating Society” ASM Handbook, vol 11, 2002.

[110] MYERS, H. R.; MONTGOMERY, D. C.; ANDERSON-COOK, C. M. “Response Surface Methodology: Process and Product Optimization Using Designed Experiments", Vol. 705. John Wiley & Sons, 2009 .

[111] MONTGOMERY, D. C.; RUNGER, G.C. “Applied Statistics and Probability for Engineers." John Wiley & Sons, 2010.

[112] RODRIGUES, C. “Friction Riveting of Aluminum 2024-T351 and Polycarbonate”, Master Thesis, Federal University of São Carlos, Brazil, 2014.

[113] CROSSLAND, B. “Friction welding”, *Contemp. Phys.*, vol. 12, nº 6, p. 559–574, Nov. 1971.

[114] BORBA, N. Z. *et al.* “Influence of Rotational Speed on the Microstructure and Mechanical Performance of Friction-riveted Thermosetting Composite Joints”, *Soldag. Amp Insp.*, vol. 21, nº 1, p. 30–43, Mar. 2016.

[115] ABIBE, A. B. “Friction-based Injection Clinching Joining (F-ICJ): a new joining method for hybrid lightweight structures”. PhD Thesis, Helmholtz-Zentrum-Geesthacht: Technischen Universität Hamburg-Harburg, Germany, 2015.

[116] CHEN, Y. C.; LIU, H. J.; FENG, J. C.; “Effect of post-weld heat treatment on the mechanical properties of 2219-O friction stir welded joints”, *J. Mater. Sci.*, vol. 41, nº 1, p. 297–299.

[117] SULLIVAN, A.; ROBSOB, J. D. “Microstructural properties of friction stir welded and post-weld heat-treated 7449 aluminium alloy thick plate”, *Mater. Sci. Eng. A*, vol. 478, nº 1–2, p. 351–360, Apr. 2008.

Appendix A –Detailed Data of Geesthacht Weather.

Table A.1 Minimum, medium and maximum outdoor temperatures recorded in Geesthacht, Germany.

	Temperature [°C]		
Month	Min	Med	Max
Feb/15	-6	2	10
Mar/15	-2	6	17
Apr/15	-3	8	31
May/15	3	11	24
Jun/15	4	15	29
Jul/15	8	18	36
Aug/15	7	19	31
Sep/15	3	14	20
Oct/15	1	9	19
Nov/15	-1	8	17
Dec/15	-2	8	14
Jan/16	-9	1	11

Table A.2 Minimum, medium and maximum air humidity and precipitation recorded in Geesthacht, Germany.

	Humidity [%]			Precipitation [mm]			
Month	Min	Med	Max	Min	Med	Max	Total
Feb/15	31	87	100	0	0.3	3	7.88
Mar/15	27	77	100	0	1	5.1	31.74
Apr/15	30	72	100	0	0.5	4.1	15.25
May/15	37	74	100	0	0.6	8.9	18.8
Jun/15	23	71	100	0	0.3	4.1	9.13
Jul/15	23	74	100	0	1.4	7.9	44.18
Aug/15	30	76	100	0	0.8	6.1	25.16
Sep/15	43	83	100	0	1.1	11.9	34.27
Oct/15	47	87	100	0	0.9	9.9	26.92
Nov/15	58	90	100	0	1.8	19.1	52.57
Dec/15	53	86	100	0	0.4	4.1	12.97
Jan/16	58	90	100	0	7.9	0.5	14.72

Appendix B - Fourier Transformed Infrared Spectroscopy

Figure B.1 shows a typical IR spectrum of polyamide 6 matrix from PA6-30GF composite with deconvoluted bands. The deconvolution was performed using Origin Pro.8.5 software. The signal processing analysis was selected followed by the base line definition and finally the deconvolution tool.

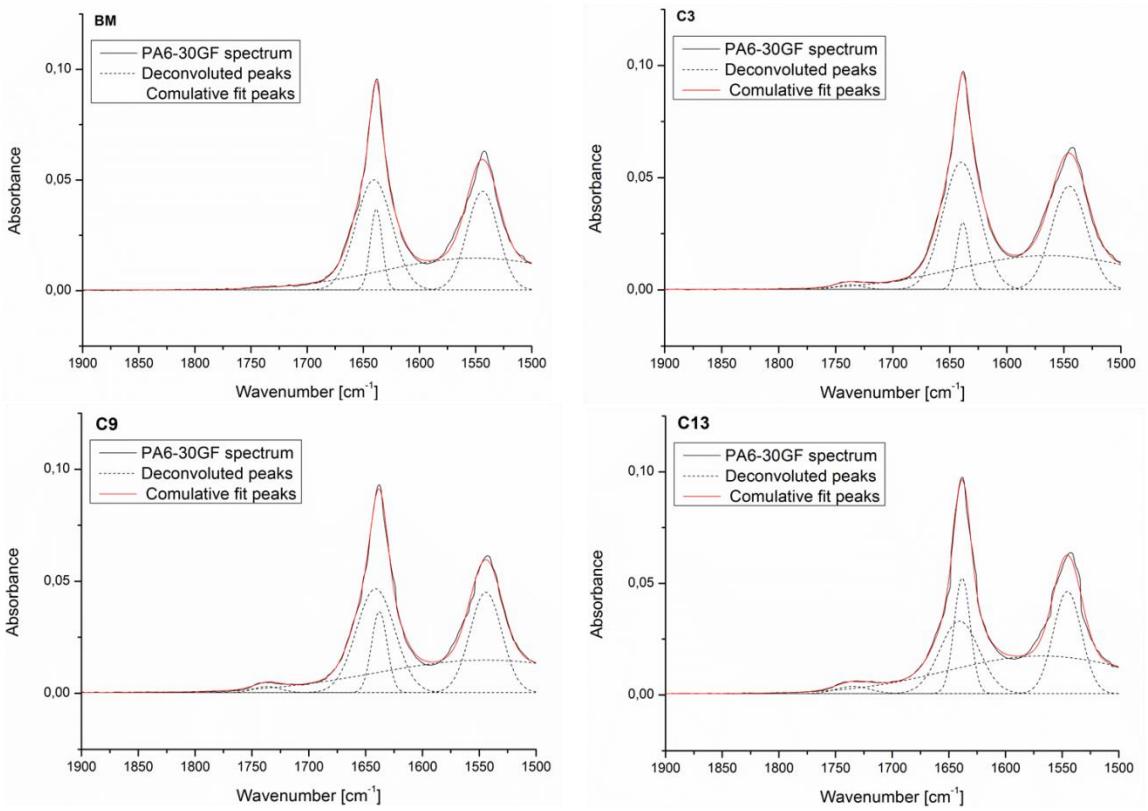

Figure B.1 Infrared spectrum of GF-P base material with deconvoluted peaks.

Appendix C –Tensile curves of AA6056-T6/PA6-30GF friction-riveted joints

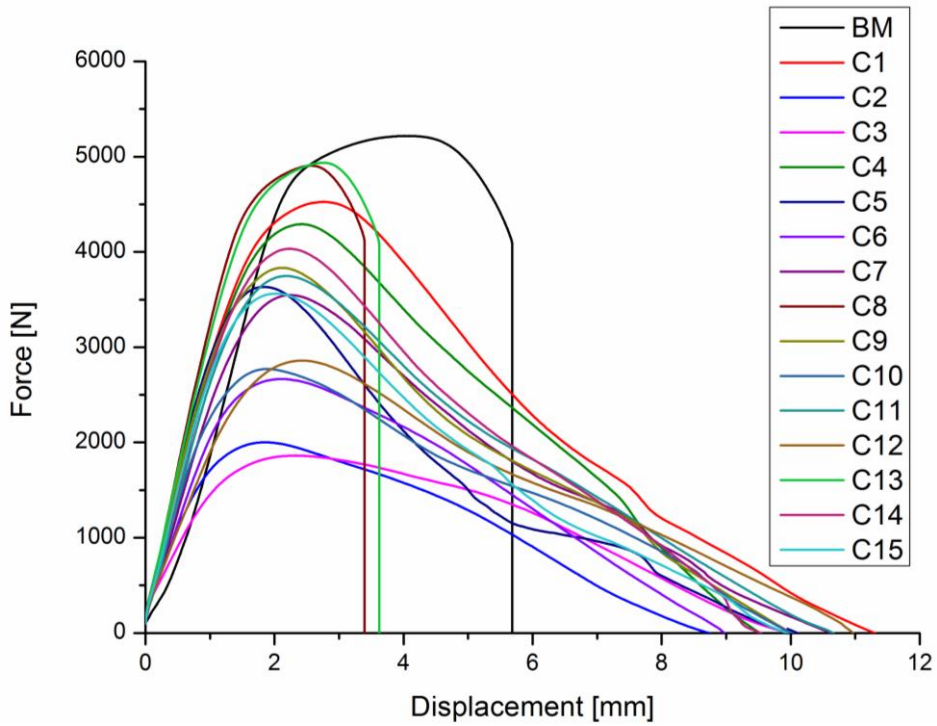

Figure C.1 Force-displacement curves of AA6056-T6/PA6-30GF friction-riveted joints

Appendix D –Surface graphs and contour plots for the viscosity average molecular weight and ultimate tensile force

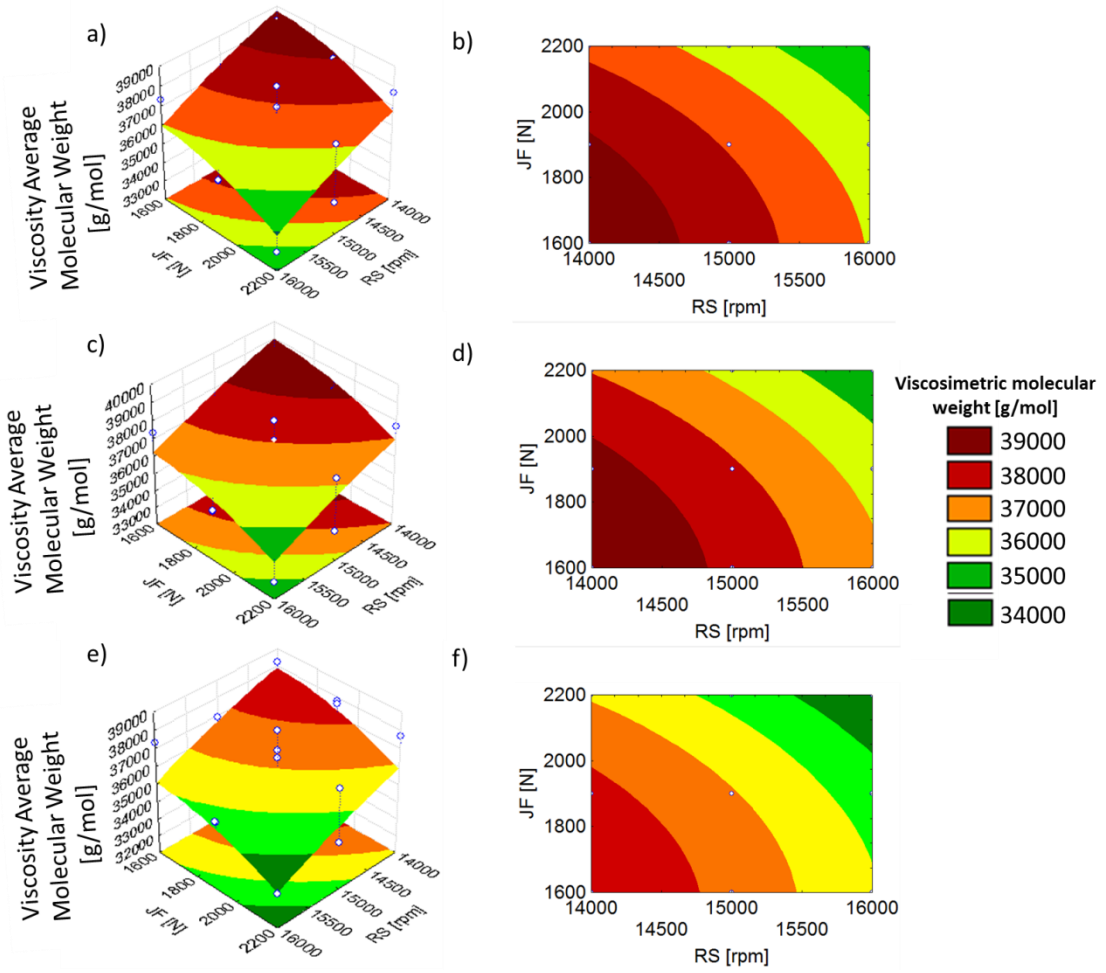

Figure D.1 Surface graphs for the viscosity average molecular weight with the Displacement at Friction fixed at 8mm (a), 9mm (c) and 10mm (e) and Contour plots for the viscosity average molecular weight with the Displacement at Friction kept constant at 8mm (b), 9mm (d) and 10mm (f).

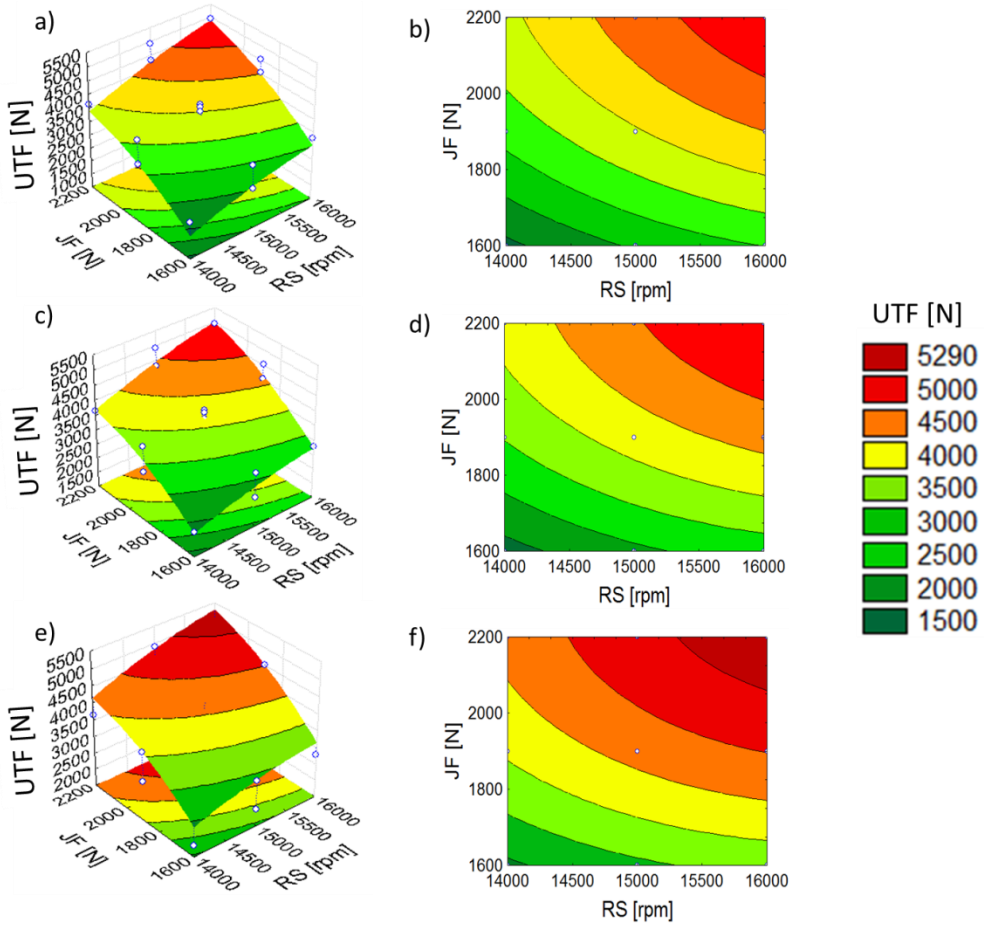

Figure D.2 Surface graphs for the ultimate tensile force with the Displacement at Friction kept constant at 8mm (a), 9mm (c) and 10mm (e), and Contour plots for the ultimate tensile force with Displacement at Friction fixed at 8mm (b), 9mm (d) and 10mm (f).

Appendix E – DSC Analysis of the Post Joined Heat Treatment Joints

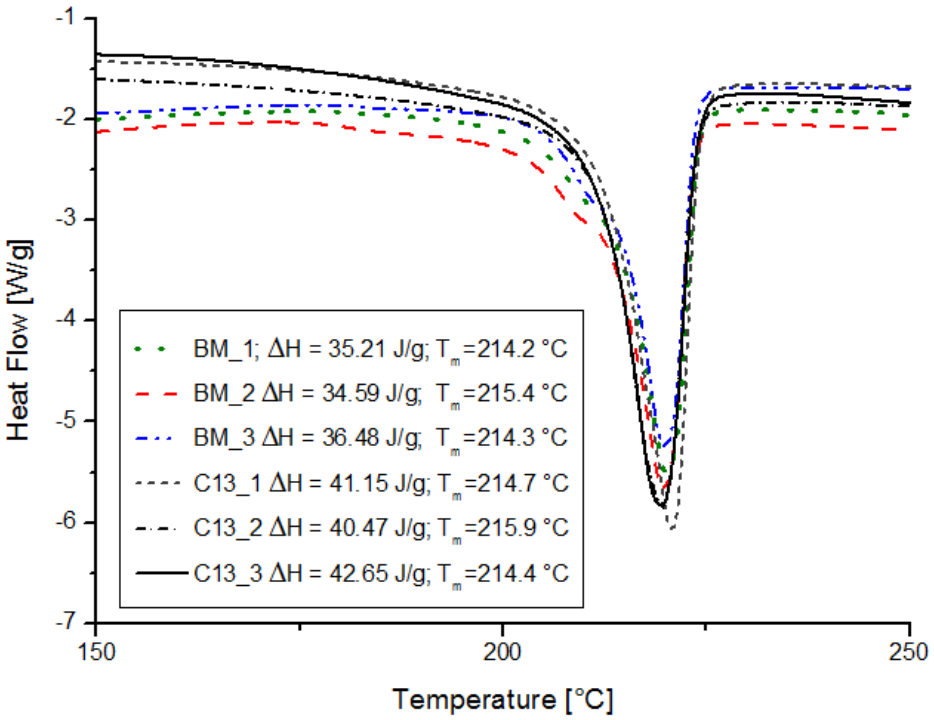

Figure E.1. DSC diagrams of the first heating run for the Base Material and C13 after PJHT